Department of Precision and Microsystems Engineering

Design and performance of a novel concept vacuum insulation panel with a honeycomb plate-foil core

J.J.M. Tjeerdsma

Report no	: 2022.086
Coach	: Matthijs Langelaar, Fred van Keulen
Professor	: Matthijs Langelaar
Specialisation	: MSD/EM
Type of report	: Master thesis
Date	: 07-12-2022

TU Delft Delft University of Technology

Challenge the future

Abstract

Reducing greenhouse emissions can be achieved by better insulating buildings. However, wall thickness increases significantly if conventional insulation materials are used. Conventional vacuum insulation panels (VIPs) offer a solution to this problem. VIPs have potential, but can not compete with conventional insulation materials due to their high pricing. A new concept vacuum insulation panel is introduced by the start-up company IQ-Bizz. To what extent this concept panel is a feasible alternative to conventional VIPs is the main research question of this thesis. The concept panel consists of two honeycomb plates, an intermediate foil and an MF2 panel envelope. The panel's geometry is chosen such that heat transfer through the panel is minimal and failure of the panel does not occur. Finite element models, verified by analytical calculations, have been used for evaluating the concept panel's structural and thermal performance. A thermal performance (R-value) of 6.23 m^2K/W is evaluated for a one-centimetre thick square panel with sides of one metre. Conventional VIPs of equal size have an R-value of 2.5 m^2K/W. The global warming potential of the concept is roughly 9.2 kg compared to roughly 15 kg for conventional VIPs. A rounded conventional VIP's price of 21 euros is compared to the material costs of the concept panel of roughly 8 euros. All performance parameters of the concept panel are higher compared to conventional VIPs. However, the concept panel's thermal performance is expected to be lower, and its environmental impact and price higher. Further research is required for a better evaluation of these performance parameters. Nevertheless, this thesis shows that the vacuum insulation panel concept has promising potential.

Contents

Chapter 1 Introduction

1.1 Motivation

Slowing global warming by reducing the emission of greenhouse gases is of paramount importance in this day and age. The Paris climate agreement states that the total reduction of these harmful gases should be at least 40 per cent in 2030 [1]. The Netherlands wants to realise a reduction of up to 55 per cent if other countries contribute [2]. There are many different areas where a reduction in CO_2 can be realised, but tackling a large contributing sector can result in a high absolute reduction. Figure 1.1 shows where greenhouse gas emissions, measured in tonnes CO_2 equivalent, come from (2016) [3]. Energy used in buildings accounts for 17.5 per cent of the global CO_2 emission. In Europe, 60-80% of energy consumption in buildings is used for space heating and cooling [4, 5]. Improving building insulation can significantly reduce CO_2 emissions [6–8].

Even though progress has been made, 69% of all residential buildings in the Netherlands consume upwards of 160 kWh per square metre of usable living space annually (second quarter 2022) [9]. Buildings that annually require less than 15 kWh/m^2 for heating and cooling, called passive houses, are the way forward. The low energy demand of these buildings is achieved by sufficient insulation. Increasing insulation performance with conventional materials can be achieved by increasing the material's thickness. However, to reach high insulation values, wall thickness is increased by 20 to 35 centimetres [10], depending on where the passive house is built [11]. This drastically reduces usable living space.

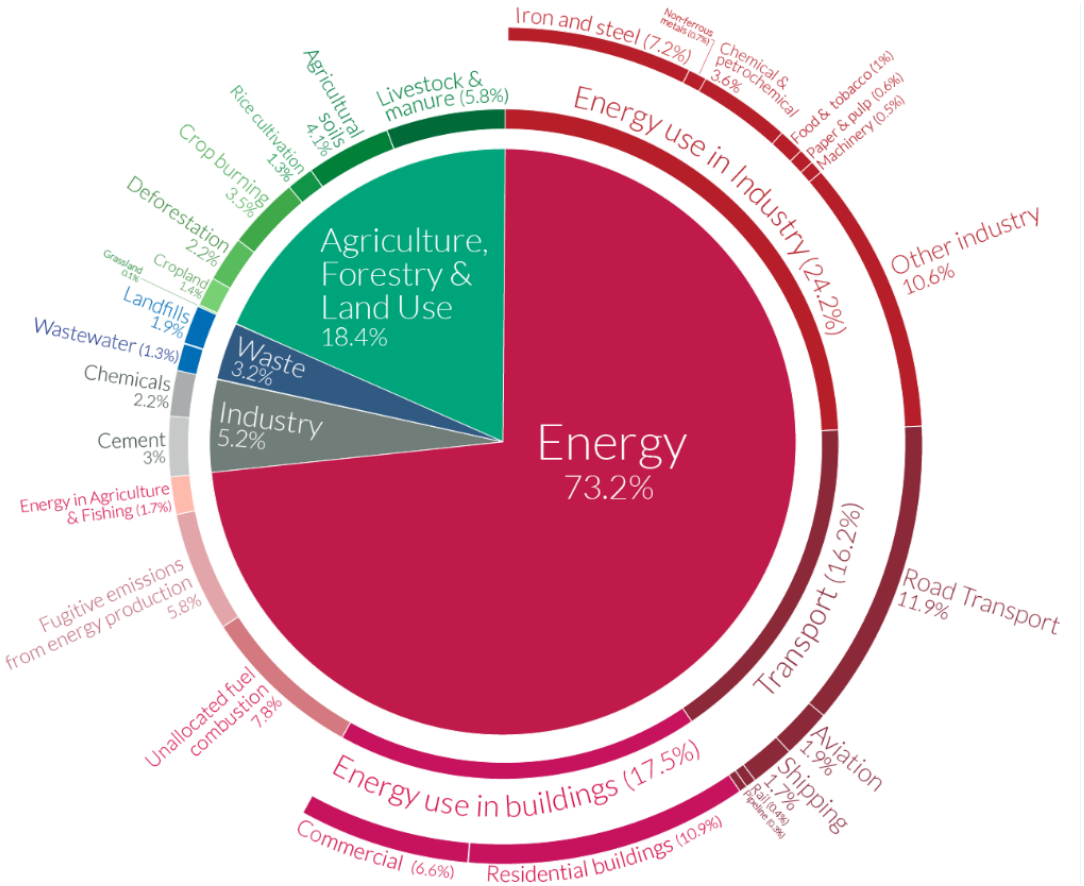

Figure 1.1: Global greenhouse gas emission by sector, measured in tonnes CO_2 equivalent [3].

Vacuum insulation panels (VIPs) potentially offer a solution to this problem. Existing panels consist of two major parts: a microporous core material and an airtight envelope [12]. The thermal performance of these panels is five to ten times better than the conventional insulation techniques [13]. VIPs have potential, but can not compete with conventional insulation at the moment due to their high pricing [14]. Vacuum insulation panels account for less than 1 per cent of the total market share [15].

A new concept by the start-up company IQ-Bizz introduces an alternative design for the core of the VIP. The single block of material that is uniformly loaded in compression is replaced by two honeycomb plates and an intermediate foil. This general panel shape was set at the start of the project and was therefore not a design choice. At first sight, this concept seems promising because structural and thermal functions can be split over the parts, creating the possibility to optimise each part's design and material selection to its isolated function, which can result in a better-performing and cheaper panel.

A key question is what advances can be achieved with this new panel concept relative to the state of the art, and whether it can form a viable alternative. This involves many aspects, ranging from technical to economic and manufacturing to life cycle aspects. Covering all these aspects in detail is beyond the scope of this thesis. This report contains an overview of the structural and thermal aspects of the concept, followed by an optimal panel geometry design and its performance. The findings discussed in this report will form the basis for the construction of prototypes and potentially an optimised physical product.

1.2 Research question and goals

To what extent is an optimised concept vacuum insulation panel a potentially feasible alternative for conventional vacuum insulation panels?

To answer the main question, shown above, underlying sub-questions listed below require answering first. Answering these questions forms the framework for this graduation project report. However, an all-encompassing answer to the main research question requires more research than what will be presented in this thesis. Fundamental aspects of the concept like its structural and thermal performance, manufacturability, and a brief assessment of economic performance and environmental impact will be assessed.

1. What are the relevant aspects that play a role in insulation panels?
2. What are the relevant parameters and aspects for the vacuum insulation panel concept?
3. What is the optimal geometry for the concept panel?
4. What is the optimal material for each panel part?
5. Is the optimal panel manufacturable?
6. What is the performance of the optimised concept panel?
7. How does the performance of the concept and conventional vacuum insulation panels compare?

1.3 Report outline

The report is structured as follows. Chapter 2 provides an overview of relevant aspects that form the basis for construction, operation and performance measurement of insulation techniques. Herein, answers to Question 1 are provided.

Chapter 3 starts with an overview of the panel concept. The concept's relevant parameters, geometry, failure mechanisms and thermal resistance are analysed in the following sections of this chapter. Thereby, Question 2 is answered.

Questions 3, 4 and 5 will be answered in Chapter 4, where a detailed design will be presented. Optimal geometry for which minimum heat transfer occurs without the panel failing will be determined analytically. Material selection of the panel parts will be discussed next, followed by manufacturing possibilities.

Question 6 will be answered in Chapter 5, where the panel's performance will be further analysed. Analytical structural and thermal performance will be presented first. Finite element models are verified with these analytical results. Subsequently, they are used for a more detailed evaluation of the structural and thermal performance of the concept panel. The economic performance and environmental impact will be briefly assessed. Subsequently, the performance of the concept will be compared to conventional vacuum insulation panels. Hereby, Question 7 is answered.

The report's conclusion and future work recommendations are the topic of Chapter 6. Herein, answers to the sub-questions and the main research question are presented.

Chapter 2 Problem analysis

2.1 Overview

The performance of insulation materials can be expressed in many different parameters. The basics and relevant aspects of these performance parameters are presented in this chapter. This report mainly focuses on thermal and structural performance. Relevant thermal aspects are the basics of heat transfer and modes of heat transfer. Equations shown in this report are not representative of three-dimensional, time-dependent heat transfer. Instead, One-dimensional and steady-state conditions are assumed to simplify calculations. Furthermore, the structural performance of the panel is determined by relevant failure modes. Aspects of these relevant modes are presented in this chapter, followed by an overview of all relevant performance parameters.

2.2 Relevant aspects

2.2.1 Basics of heat transfer

Heat transfer is governed by physical principles. First, the first law of thermodynamics for a closed system, shown in Equation (2.1) [16], states that energy is always preserved. The change in internal energy of a system is always equal to the heat transfer into the system combined with the heat generated within that system. Second, conduction (solid, liquid and gas), convection (liquid and gas) and radiation (gas) are the possible modes of heat transfer [12, 17]. Third, the heat transfer through a medium for each mode of heat transfer can be expressed as a heat flux multiplied by the area perpendicular to the direction of the heat flow for one-dimensional heat transfer, as shown in Equation (2.2) [16]. One-dimensional general equations exist for all heat transfer modes. These equations can be used to analyse heat transfer through parts of the panel. These equations form the basis for performance evaluation of the panel parts and therefore the complete panel, regardless of the operating conditions. An overview of the modes of heat transfer will be discussed in Section 2.2.2. The total heat transfer can be calculated by combining the heat transferred by individual modes. Finally, three-dimensional and time-dependent heat transfer equations should be used to describe heat flow in more complex situations accurately.

$$\rho V c_v \frac{dT}{dt} = \dot{Q}_i + \dot{Q}_v, \qquad (2.1) \qquad\qquad \dot{Q} = qA. \qquad (2.2)$$

Where:

ρ = Density of the medium [kg/m^3]
V = Volume of the medium [m^3]
c_v = Constant-volume specific heat [J/kg K]
dT/dt = Change in temperature [K/s]
$\dot{Q}_i$ = Heat transfer into the system [W]
$\dot{Q}_v$ = Heat generated in the system [W]
$\dot{Q}$ = Heat transfer [W]
q = Heat flux [W/m^2]
A = Area of the medium perpendicular to the flow direction [m^2]

2.2.2 Modes of heat transfer

Conduction

Thermal conduction is the transfer of energy from one particle to another when the two collide [16]. Heat can be conducted from hot to cold areas in any medium as long as it contains particles. An increase in the internal energy of the particles near the hot side causes increased particle vibration. As a result of this, collisions with neighbouring particles occur and energy is transferred. On a macro level, this repeating energy transfer cycle allows heat to progress from the hot to the cold side of a medium. This process can be described with the help of Equation (2.1), shown in Section 2.2.1. Fourier's equation (or the heat equation), shown in Equation (2.3) [16], can be obtained when the heat generation in the system is assumed to be zero and the heat transferred into the system is rewritten as a function of the spatial coordinates x, y and z. Equation (2.3) shows the time and location dependency of the process. However, equilibrium is reached after a certain period. If only one-directional heat transfer (from hot to cold side) is considered and a uniform medium is assumed, Equation (2.3) can be simplified to obtain Equation (2.4) for one-dimensional steady-state heat conduction [16]. Here k is a material-dependent constant and L depends on the geometry. A thick insulation panel made from a material with low thermal conductivity is ideal for low heat transfer through that panel.

$$\frac{\partial T}{\partial t} = \frac{k}{\rho c_v}\left(\frac{\partial^2 T}{\partial x^2} + \frac{\partial^2 T}{\partial y^2} + \frac{\partial^2 T}{\partial z^2}\right), \qquad (2.3)$$

$$q = \frac{k\Delta T}{L}. \qquad (2.4)$$

Where:

k = Thermal conductivity of the medium [$\mathrm{Wm^{-1}K^{-1}}$]
q = Heat flux [$\mathrm{W/m^2}$]
ΔT = Temperature difference between sides of the medium [K]
L = Length of the path of conduction [m]

The amount of heat transferred by conduction decreases when collisions between neighbouring particles become more difficult. This can be achieved for gaseous conduction by increasing the distance between particles or by blocking the path between them. A vacuum decreases the number of particles in a gas. Hence, the distance between the remaining particles is enlarged. Adding a porous material to a medium where gaseous conduction occurs, shortens the free path length of the particles. Gaseous conduction can be reduced to zero before an ideal vacuum is reached if the pore sizes are smaller than the distance between neighbouring particles [12, 18]. Conventional vacuum insulation panels have a porous core and rely on this effect for their high thermal performance. Equation (2.5) shows the conductivity (of a gas) as a function of pressure, free path length and mean temperature [19, 20]. Note that solid conduction can always occur through the added porous material, regardless of the pressure.

$$k = \frac{k_0}{1 + \frac{7.6\times10^{-5}}{\frac{pl}{T_m}}} \qquad (2.5)$$

Where:

k_0 = Conductivity of air at room temperature and pressure [$\mathrm{Wm^{-1}K^{-1}}$]
p = Air pressure [Pa]
l = Free path length [m]
T_m = Mean air temperature [K]

Convection

Convection is a method of energy transfer through the flow of fluids or gases. Two types of convection exist; natural and forced convection. Natural convection occurs when a natural phenomenon, for example, the rising of a heated fluid or liquid or the gravitational pull on a particle, is the driving force of the medium's movement. Forced convection occurs if an object is placed in a liquid or gaseous flow with a different temperature compared to the object [16].

Natural convection occurs in an air gap between two plates, for example in double glazing, when a temperature difference between the two plates creates a natural, heat-transferring flow. The heat flux of natural convection can be calculated with Equation (2.6) [16]. The heat transfer coefficient h depends on medium-specific parameters, operation conditions, conductivity (shown in Equation (2.5)), temperatures of the hot and cold plates and the distance between these plates. It can be calculated in multiple steps, shown in Appendix B. In general, though, convective heat transfer can be neglected if the gap between the plates is evacuated.

$$q = h\Delta T \tag{2.6}$$

Radiation

Heat can be transferred between surfaces via electromagnetic radiation emitted from the hotter surface and absorbed by the colder surface. The material, temperature, size and orientation of both surfaces influence the total energy transfer between the two surfaces. In practice, the absorbing surface reflects a fraction of the incoming electromagnetic waves back to the hot surface. Reflection between both surfaces eventually dies out as a result of space and surface resistance, shown in Equations (2.7) and (2.8) respectively [16]. Subscript 1 and indicates the hot surface cold surface respectively. The space and surface resistance act in series and can be found in the denominator of the linearised energy balance method, shown in Equation (2.9) [16] Equation (2.9). This linearised version may be used to calculate the radiative energy transfer when the temperature difference between the hot and cold sides is small. If the areas of both plates (with subscripts one and two) are equal, both sides in Equation (2.9) can be divided by the area to find the heat flux, shown in Equation (2.10).

$$R_{space,12} = \frac{1}{A_1 F_{12}}, \tag{2.7}$$

$$R_{surf} = \frac{(1-\varepsilon)}{\varepsilon A_{1,2}}. \tag{2.8}$$

Where:

$R_{space,12}$ = Space resistance in path from hot body to cold body [m^{-2}]
R_{surf} = Surface resistance of emitting surface (can be 1 or 2) [m^{-2}]
ε = Emittance of surface material [-]
A = Area subscript 1 indicates the hot surface and 1,2 can be both surfaces [m^2]
F_{12} = Shape factor of hot and cold surface orientation [-]

$$\dot{Q} = \frac{\sigma 4 T_m^3 \Delta T}{\frac{1-\varepsilon_1}{\varepsilon_1 A_1} + \frac{1}{A_1 F_{12}} + \frac{1-\varepsilon_2}{\varepsilon_2 A_2}}, \tag{2.9}$$

$$q = \frac{\sigma 4 T_m^3 \Delta T}{\frac{1-\varepsilon_1}{\varepsilon_1} + \frac{1}{F_{12}} + \frac{1-\varepsilon_2}{\varepsilon_2}}. \tag{2.10}$$

Where:

σ = Stefan-Boltzmann constant = 5.67×10^{-8} [$Wm^{-2}K^{-4}$]
T_m = Mean temperature of hot and cold surface [K]
ΔT = Difference between the hot and cold surface [K]

2.2.3 Structural failure mechanisms

Creep

Creep is a continuous plastic deformation of materials, which can eventually lead to failure of a part. It is the dominant failure mechanism when either stresses or operation temperature or both are high for an extended period. Multiple modes of creep exist, each with different characteristics. Which creep mechanism is active depends on the operation conditions (stress and temperature) and material parameters (elasticity modulus and melting temperature). This is shown graphically in a deformation mechanism map. The map for a stainless steel is shown in Figure 2.1 [21]. Stainless steel will be selected, as will be explained in Chapter 4. Locations of the creep mechanism boundaries in Figure 2.1 can shift slightly for different grain sizes and materials, but the general shape holds for metals, polymers and ceramics [21]. Regions of dislocation plasticity, power-law and diffusional flow creep ensure high shear rates and should be avoided if possible. However, creep is also present as coble creep in the region indicated with elastic deformation in Figure 2.1 [22]. Coble creep occurs at temperatures below 0.4 times the material's melting temperature and all stresses. Figure 2.2 shows the percentage of plastic strain caused by creep for a stainless steel at low operation temperature of 22°C for multiple applied loads. The yield strength of the tested steel is 221 MPa. Creep is only truly negligible for stresses of 145-155 MPa or roughly a factor 1.5 lower than the yield strength. This factor of 1.5 is assumed to be valid for all materials. Therefore, it will also be used in the design for the foil. Concluding, stress in the parts of panel should remain below two-thirds the yield strength and operation temperature should stay below 0.4 times the melting temperature of the materials.

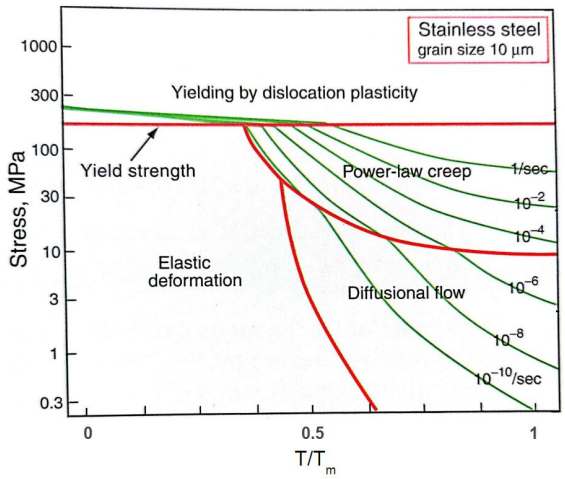

Figure 2.1: Schematic illustration of the conventional deformation mechanism map of normalised stress versus homologous temperature [21, 22].

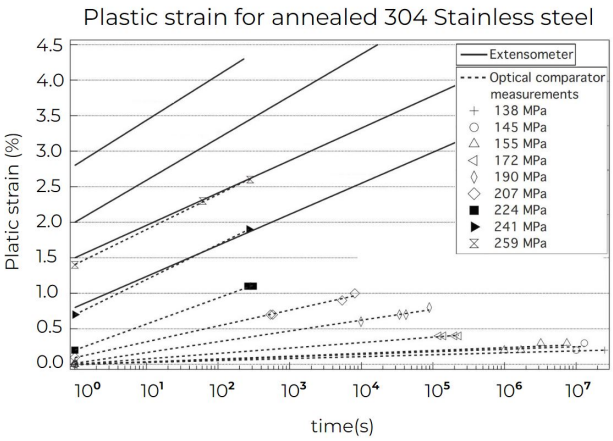

Figure 2.2: Plastic strain versus log time behaviour of annealed 304 stainless steel [23].

Buckling

Buckling failure is characterised by a sudden large transverse deflection of the failed part. Failure occurs when a compressive load on the part exceeds a certain threshold. Below this threshold, the part is in a stable equilibrium and no deflection will occur. Above the threshold, it will become unstable and the part can fail. Slender beams and shafts are prone to buckling. Supporting the centre of slender parts reduces the risk of buckling. However, altering design is not always possible. This does not mean that slender parts can not be used, but that axial loads should be carefully considered.

2.2.4 Performance parameters

Thermal performance

The primary measure of performance used for insulating panels is the R-value [m^2K/W]. The R-value of conventional insulation panels primarily depends on the resistance to solid conduction. Therefore, their R-values can be increased by increasing the panel's thickness or constructing the panel from a material with a lower thermal conductivity. However, other modes of heat transfer, besides solid conduction, are relevant for the vacuum insulation panel concept.

The R-values for modes of heat transfer can be calculated with Equation (2.11), where the heat flux q can be calculated with one of the equations shown in Section 2.2.2. Multiple heat transfer modes can simultaneously contribute to the transfer of heat. The R-value of each mode of heat transfer is converted to thermal resistances R [K/W] by dividing it by the area, shown in Equation (2.12). The thermal resistances can be combined and converted back to the R-value of the panel. Higher-order phenomena, such as thermal bridging, are hereby neglected.

$$R_{val} = \frac{\Delta T}{q}, \tag{2.11}$$

$$R = \frac{R_{val}}{A}. \tag{2.12}$$

Economic performance

A measure of the success of any product is its economic feasibility. A new product is economically feasible if the money saved by using the new product is higher than its total cost. The total cost can be evaluated in a life cycle cost analysis (LCCA). Herein, production, installation, operation, maintenance and salvage costs are combined in a total product price [24]. However, an LCCA falls outside the scope of this thesis, where only material costs will be considered. Therefore, further research is required to accurately estimate the concept VIP's total costs.

Environmental performance

Currently, heating buildings has a considerable impact on the environment, as discussed in Section 1.1. Therefore, any product that reduces the need for heating seems a good option. However, products that provide better insulation might be energy intensive to make themselves. The energy required to produce products can outweigh the benefits of their usage. There are a couple of factors that describe the environmental impact of a product. These factors should be considered in an envrionmental impact study. However, only the Global Warming Potential (GWP) will be used in this thesis. The GWP describes the global warming impact of the product in terms of kilograms CO_2.

2.3 Conclusions

The relevant aspects that play a role in insulation can be divided into thermal, structural, economic and environmental parameters. The relevant modes of heat transfer are conduction, convection and radiation. The R-value and thermal resistance of the individual modes of heat transfer can be calculated. The thermal resistances of each mode can be combined to obtain the total thermal resistance, which can be converted to the total R-value. Creep is the failure mechanism that should be designed for. Stress in the part should remain below two-thirds of the yield strength and temperature should remain below 0.4 times the melting temperature. This results in requirements for materials parameters. The economic performance and the environmental impact are assessed by evaluating the materials costs and the Global Warming Potential, respectively. A Life cycle cost analysis and an environmental impact study estimate the economic and environmental performance, but fall outside the scope of this thesis. Therefore, future research is required for the evaluation of these two performance parameters.

Chapter 3 Conceptual design

3.1 Overview

The concept vacuum insulation panel will be presented in this chapter. The first section contains a global description of the panel and its parts. The geometry of the panel parts is determined by parameters. Besides changing the geometry, these parameters affect the performance of the panel. Reducing the thickness of the panel parts leads to better thermal performance of the panel. Besides, overall weight and price reduce with reducing thickness. However, the system can fail if stress imposed by the external air pressure exceeds structural limits. A failure mechanism and thermal resistance analysis of the concept panel will be presented in this chapter. Herein, analytical panel performance will be evaluated with the help of geometrical models and equations presented in Section 2.2. Only models representative for the panel's centre will be presented in this thesis. A failure mechanism analysis of the panel's edges requires further research.

3.2 Description of the concept panel

The complete panel consists of three essential elements: a honeycomb plate, an intermediate foil and an envelope. Two stacked honeycomb plates with a foil placed between them make up the panel's core. A honeycomb plate is essentially a repeating pattern of the structure shown in Figure 3.1. This structure will from hereon be referred to as 'single honeycomb'. A portion of four of the six walls of the single honeycomb is cut away, as shown in Figure 3.1. A graphical representation of the resulting honeycomb plate is shown in Figure 3.2. The second honeycomb plate is identical to the first, but its orientation differs. The plate is flipped, so that the incisions are pointing down, and positioned such that its walls do not touch the walls of the first plate. Figure 3.3 shows a section of the core of the panel, where the second honeycomb plate and foil are placed on top of the single honeycomb shown in Figure 3.1. The two honeycomb plates are only connected via the intermediate foil. Cutouts in the honeycomb plate ensure maximum distance between locations where the opposing plates make contact with the foil. The final element of the concept panel is the panel envelope. It is wrapped around the core such that an airtight seal is created. After that, the core of the panel is evacuated. A collection of graphical representations of the concept panel can be found in Appendix C.

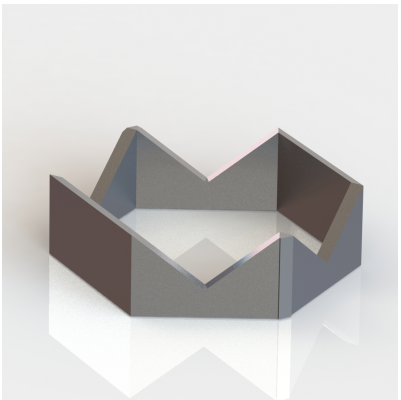

Figure 3.1: A single honeycomb.

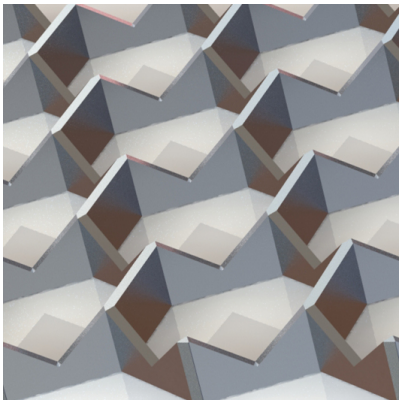

Figure 3.2: A honeycomb plate.

Figure 3.3: A section of the core.

3.3 Relevant parameters

General parameters

General parameters are the panel's length, width and thickness and define the panel's size. They are independent of the dimensions of the panel parts. However, there is no need for both the length and width to be variable in estimating of theoretical panel performance. Therefore, the panel is assumed to be square. Consequently, the total size of the panel area can be defined by a single parameter: w_p. Panel thickness t_p is defined for the non-evacuated case. Hereby, the foil is assumed to be horizontal. The panel thickness will decrease slightly when the panel is evacuated due to the deflection of the foil.

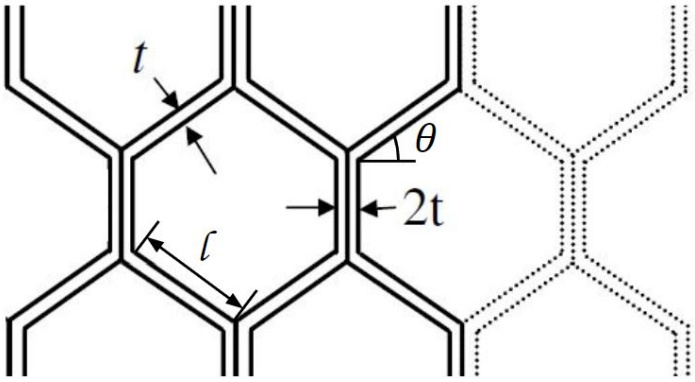

Figure 3.4: Geometry of a conventional honeycomb plate [25].

Honeycomb plates

A honeycomb plate is a repeating pattern of hexagons with a certain thickness and height. A hexagon's geometry can be defined by two parameters: honeycomb angle θ and wall length l. It is hereby assumed that all sides of the hexagon are equal. Conventional honeycomb plates are used for the concept vacuum insulation panel. They are made with strips of sheet metal with thickness t_h. These strips are bonded to each other to form a honeycomb plate. Therefore, locations where two strips are attached have a thickness equal to twice the thickness of a strip. All geometric parameters are shown graphically in Figure 3.4.

The geometry of a three-dimensional honeycomb plate also depends on the plate height and the number of single honeycombs that fit in the plate. However, both parameters can be written as a function of already defined parameters and are therefore not relevant parameters themselves. Plate height is equal to half the previously defined general parameter panel height. The number of single honeycomb structures that fit in a honeycomb plate depends on the size of a single honeycomb, its thickness and the total size of the panel.

The parameters for the cutouts in the honeycomb walls, shown in Figure 3.1, will be defined next. Both the width and height of the triangular-shaped cutout can be chosen freely. To reduce the number of parameters, the width of the cutout is set equal to the honeycomb side length. Cutouts should be sufficiently high so they do not touch the intermediate foil when it deforms. However, increasing the height of the cutout also weakens the honeycomb plates. Therefore, cutout height h_{cutout} is a relevant design parameter.

Four relevant parameters need to be added to the already defined general parameters to define a honeycomb plate: honeycomb angle θ, honeycomb wall length l_h, honeycomb thickness t_h and honeycomb cutout height h_{cutout}.

Foil

The length and width of the foil are equal to the length and width of the panel. Since the panel is assumed to be square, the foil is automatically assumed to be square. Therefore, the panel geometry fully defines the area of the foil. Only foil thickness, t_f, is necessary to define the geometry of the foil.

Envelope

The geometry of the envelope is equal to the geometry of the panel. However, the thickness of the envelope can still be chosen freely. Standard panel envelopes already used in existing panels consist of more than one layer. These envelopes have been studied in detail in previous studies. A short overview of relevant information on existing panel envelopes can be found in Appendix D. The design of a new envelope type is not the aim of this project. Therefore an existing envelope will be used for the panel. Consequently, envelope type is the free variable that fully describes the composition and properties of the envelope.

Overview of relevant parameters

An overview of the remaining relevant parameters for the panel, accompanied by their symbol used in further calculations, is listed below. Items one to seven are geometrical parameters that define the shape of the panel. Items eight to ten are material parameters. The honeycomb plates and the foil are assumed to be made from a single material. Material selection for these parts is therefore not discussed above. The envelope type is slightly different since the envelope consists of multiple layers of different materials.

1. Honeycomb angle, θ
2. Panel thickness, t_p
3. Panel width, w_p
4. Honeycomb wall length, l_h
5. Honeycomb thickness, t_h
6. Honeycomb cutout height, h_{cutout}
7. Foil thickness, t_f
8. Envelope type
9. Honeycomb plate material
10. Foil material

3.4 Geometry analysis

Calculating structural and thermal properties of the entire panel at once is complicated since all honeycombs of a plate are linked to each other and the honeycombs from the opposite plate via the foil. Simplification can be found in the use of simpler models that are representative of the entire panel. Before this is possible, a closer look at the panel geometry is necessary.

Figure 3.3 in Section 3.2 shows a helpful section of the panel. However, this particular geometry cannot be used to form a complete panel by repeating it in two directions. Therefore, a new structure, shown in Figure 3.5, is introduced. This structure will, from hereon, be referred to as the panel's unit structure. The only difference between the unit structure and the panel section shown in Figure 3.3 is that the width of the unit structure is reduced.

An imaginary box can be placed around the unit structure, as shown in Figure 3.6. This box will, from hereon, be referred to as the panel unit cube. Note that the unit cube is not actually a cube, but a cuboid. Dimensions of the unit cube are length L, width W and height H. These are not free variables, but follow from the size of the unit structure, which is determined by the relevant parameters. The height of the unit structure is determined by the free variable panel thickness. The length and width of the structure are predominantly determined by the honeycomb wall length and honeycomb angle. However, honeycomb wall length only defines the size of the inner hexagon. The walls of the unit cube connect to the outside of the honeycomb walls. Therefore, their position is also determined by the thickness of the honeycomb walls.

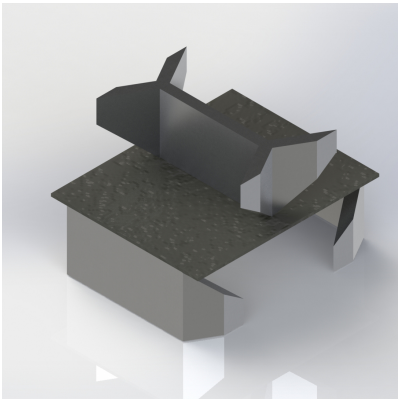

Figure 3.5: Model of panel unit structure.

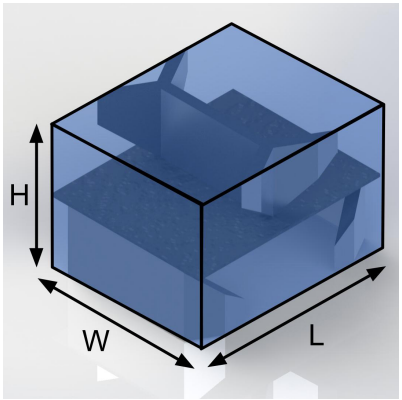

Figure 3.6: Model of panel unit cube.

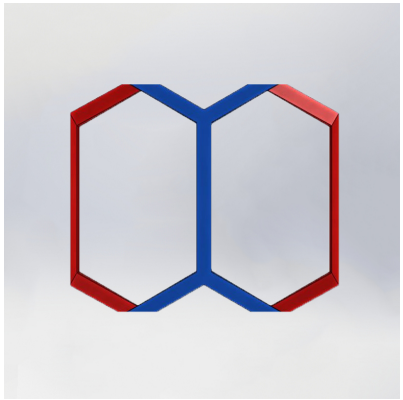

Figure 3.7: Top view of the panel unit structure.

A top view of the unit structure, shown in Figure 3.7, will be helpful for further panel analysis. The top honeycomb is shown in blue and the bottom honeycomb is shown in red. The intermediate foil is removed to show the bottom honeycomb. Now, it is important to define two different wall types: vertical walls and diagonal walls. The vertical walls of the honeycombs are twice as thick as the diagonal walls. All diagonal walls do have a portion of the honeycomb wall cut away. This definition of vertical and diagonal walls will be used further. The vertical walls of the honeycomb in Figure 3.7 are shown separately in Figure 3.8. Herein, the diagonal walls (with the cutout) are shown slightly faded. Figure 3.9 shows the three-dimensional representation of the vertical walls and the foil.

The unit structure can be repeated horizontally to form a row of unit structures. This is shown from the top in Figure 3.10. This row must be repeated vertically multiple times to form a complete panel. For every next row however, the colours assigned to the row must be switched: red honeycombs become blue and blue honeycombs become red. Switching the colours

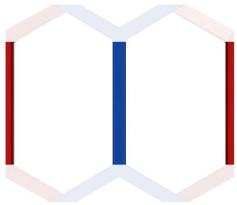

Figure 3.8: Top view of the vertical walls of the panel unit structure.

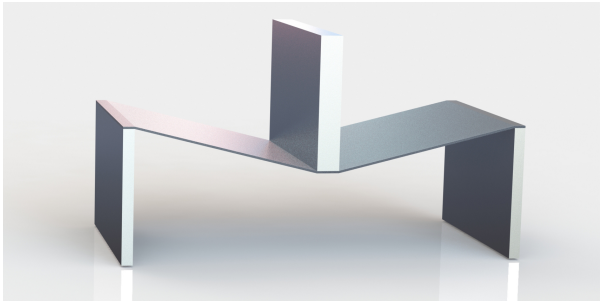

Figure 3.9: Simplified model of the unit structure.

is necessary to acquire a continuous pattern, as shown in Figure 3.11. However, blue and red indicated the top and bottom honeycombs. Reversing the colours in a row equates to flipping the row. Flipping a row, or a unit structure for that matter, does affect the appearance of the row. However, the number of walls in the row has not changed and their properties are not affected either. If a panel were to be constructed with these flipped rows, it would not look like the panel shown in Figure 3.12, but it would have similar thermal properties. Therefore, a hypothetical panel with equal thermal properties can be constructed out of a single unit structure. However, the unit structure's dimensions still need to be determined.

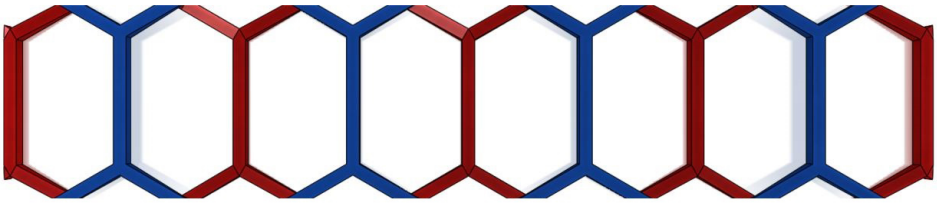

Figure 3.10: A row of unit structures.

Changing parameters that define the shape of the unit structure inherently changes the shape of the entire panel. Therefore, the unit structure can be used for structural and thermal calculations. Two models, shown in Figures 3.1 and 3.9, are of particular interest. The structure shown in Figure 3.9 is used for situations where both plates and the foil play a role. For example, the heat conduction from one side to the other or the structural rigidity of the panel for axial compression. This model will be referred to as the simplified model from hereon. The model of a single honeycomb, shown in Figure 3.1, is used for calculating structural properties for transverse load cases.

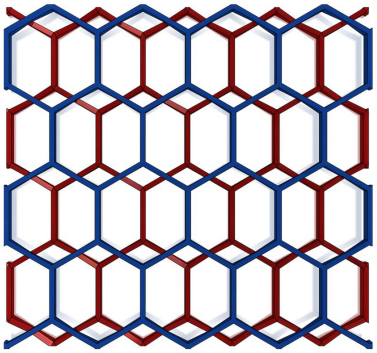

Figure 3.11: A panel constructed with unit structures.

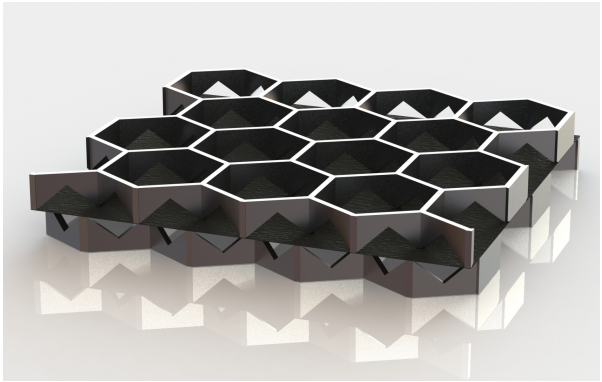

Figure 3.12: Three-dimensional representation of the panel.

3.5 Failure mechanisms analysis

Atmospheric pressure compresses the panel due to the vacuum created in the core. This compression can ultimately lead to failure. A failure mechanisms analysis that uses the previously defined unit structure and unit cube (shown in Figures 3.5 and 3.6 respectively in the previous section) is done to understand the panel's possible failure modes better. The pressure on the unit cube is equal to the pressure on the panel's outside and stresses in the unit structure are representative of stresses in the panel. Three failure mechanisms affect the design of the honeycomb plates: yield, creep and buckling. As mentioned in Section 2.2.3, creep occurs when stress comes above two-thirds of the yield strength of the material and buckling occurs if the axial load exceeds the critical buckling load. Both failure mechanisms have lower critical stresses compared to failure by material yield. Therefore, only creep and buckling are analysed. Besides creep and buckling, VIPs can fail in a variety of ways. Failure can occur shortly after manufacturing if the panel envelope is not sealed correctly. Panels can also get damaged during transportation or installation. Subsequently, air gets into the panel's core, eradicating the vacuum. However, these failure modes do not affect the design of the panel. Therefore, they are not discussed further.

The panel is compressed from all directions simultaneously. However, two different loads on the unit cube are considered for further analysis: axial and transverse loads. A graphical representation of the load cases is shown in Figure 3.13. Axial load is caused by compression the panel's larger top and bottom areas. This compression results in an axial force on the unit cube that can be calculated with Equation (3.1). Analogous to Equation (3.1), Equation (3.2) can be used for the transverse load. F_{top} and $A_{rect,top}$ are replaced by F_{side} and $A_{rect,side}$ respectively. F_{side} is the force acting on one of the two sides of the unit cube. Since the unit cube is a cuboid, the areas of the two sides of the unit cube are not equal. Therefore, the force acting on each side is not equal either. Areas of all cuboid sides follow from panel parameters. These relations are shown in Appendix E. Since these (slightly complicated) relations serve no purpose in this chapter, $A_{rect,top}$ and $A_{rect,side}$ will be used for the areas of the top and side surfaces respectively.

$$F_{top} = p_{ext} A_{rect,top}, \tag{3.1}$$

$$F_{side} = p_{ext} A_{rect,side}. \tag{3.2}$$

Where:

F_{top} = Axial force acting on the top and bottom of the unit cube [N]
p_{ext} = External air pressure [Pa]
$A_{rect,top}$ = Area of the top surface of the unit cube [m^2]
$A_{rect,side}$ = Area of a side surface of the unit cube [m^2]

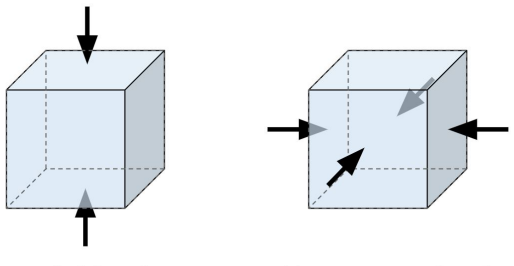

Figure 3.13: Load cases on the unit cube.

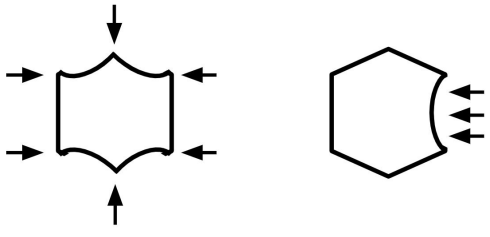

Figure 3.14: Bending of the diagonal (panel centre) and vertical honeycomb walls (panel edge)

The structure inside the unit cube (and therefore the entire panel) deforms due to the just established loads on the unit cube. Both this deformation and the accompanying stress must be restricted. An overview of the load cases on the honeycomb plates and the possible failure modes will be presented next. The analysis presented in this section is a simplification of reality. Loads on the unit cube are assumed to be perpendicular to the unit cube's surface and imperfections of the honeycomb plates are neglected. Furthermore, the honeycomb plates and foil are considered separately. However, both parts do affect the other's structural performance since they are connected. The foil limits the deformation of the honeycomb plate's walls. This increases the stiffness of the panel, but generates additional stress in the foil itself. A more realistic analysis with finite element models will be presented in Section 5.2. However, the honeycomb plates and foil are still considered separately. How the structural performance of each part is affected by the other falls outside this report's scope and remains to be assessed in future work.

Axial load on the unit cube results in axial compression of the unit structure. This axial compression is primarily restricted by the vertical walls in the honeycomb plate. These walls are twice as thick as the diagonal walls, as discussed in Section 3.3. The connected diagonal walls increase the resistance to transverse deformation of the vertical walls. Therefore, the shape of the honeycomb plates ensures high resistance to buckling of axially loaded vertical walls. Consequently, creep is the only relevant failure mechanism for the axial load case. Meanwhile, more complex load cases are present for the transverse loads on the unit cube.

The shape of the honeycomb plates does not restrict deformation for the transverse load cases on the unit cube, as it did for the axial load case. Both the vertical and diagonal walls undergo axial load and bending. Bending of the vertical walls occurs at the edges of the panel. Atmospheric compression causes a distributed load on this wall. Bending of the diagonal walls occurs throughout the panel. A single honeycomb at the centre of the panel is connected to neighbouring honeycombs at specific locations. The single honeycomb is compressed only at these locations. Figure 3.14 shows how loads, shown by the black arrows, translate to bending deformation for a single hexagon.

In order to prevent creep failure, the maximum bending stress combined with stress imposed by axial compression should remain below two-thirds of the yield strength, as discussed in Section 2.2.3. Furthermore, buckling can occur in both vertical and diagonal walls. A graphical representation of the possible failure modes is shown in Figure 3.15. Dimensions of the panel will be chosen such that loads and stress remain below critical values. A detailed analysis of dimensional design will be presented in Chapter 4.

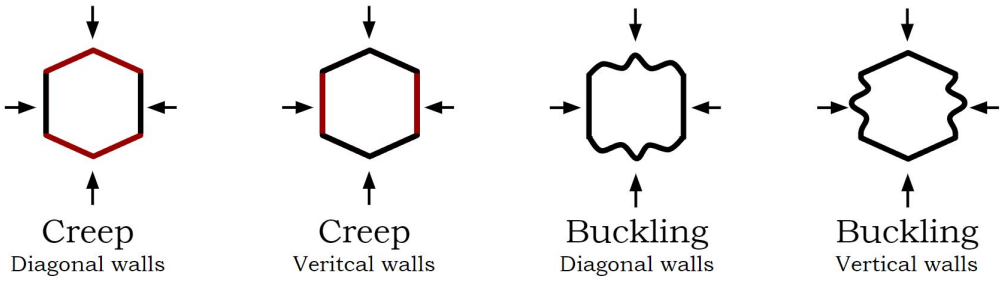

Figure 3.15: Possible failure modes as a result of transverse loads.

3.6 Thermal resistance analysis

General approach

The thermal resistance of the panel is determined by the combined thermal resistance to individual modes of heat transfer. The modes of heat transfer are solid conduction, gaseous conduction, convection, radiation and edge losses. These modes influence each other in reality. However, reality needs to be simplified to estimate the total thermal resistance of the panel analytically. Therefore, models are used where each mode is completely isolated. The simplified model of the panel core, shown in Figure 3.9 in Section 3.4, will be considered for solid conduction. A hypothetical panel without a core will be the basis for the gaseous conduction, convection, radiation and edge losses estimations. This hypothetical panel is essentially an evacuated, empty box with outer dimensions equal to the panel dimensions. Besides simplification in models, the actual behaviour of heat transfer modes will be simplified as well. These analytical estimates will be used to verify more complex models in Chapter 5.

Thermal resistance to solid conduction is not calculated for an area equal to the panel area. Instead, it is calculated for an area the size of a unit cube. The thermal resistance of the entire panel is equal to the thermal resistance of a unit cube divided by the number of unit cubes that fit in a plate. Subsequently, all thermal resistances are calculated for equal panel area and can be combined to find the total resistance.

Solid conduction

Solid conduction through the panel is a three-dimensional problem and can only be accurately solved with the help of finite element models. However, the problem can be simplified so that it is possible to estimate the thermal resistance analytically. For this simplification, one-dimensional solid conduction is assumed. The thermal resistance to solid conduction through an object for this one-dimensional case can be calculated with Equation (3.3) [16].

$$R_{cond} = \frac{L}{kA} \tag{3.3}$$

Where:

R_{cond} = Thermal resistance to conductive heat transfer [K/W]
L = Length of the object [m]
k = Thermal conductivity [$\mathrm{Wm^{-1}K^{-1}}$]
A = Cross-sectional area of the object [$\mathrm{m^2}$]

Calculating the total thermal resistance to conduction from one side to the other for the complete panel with Equation (3.3) is not trivial since the panel core consists of many linked parts. All honeycombs are in contact with each other via the foil. However, the diagonal walls, as introduced in Section 3.4, are not in contact with the foil since part of these walls has been removed. Consequently, only the vertical walls can conduct heat to and from the foil. These walls are considered in the simplified model (shown in Figure 3.9). Therefore, this model is used to simplify the problem. The thermal resistance of the entire panel is equal to the thermal resistance of the structure divided by the number of structures that fit in a plate. Hence, it is necessary to determine the thermal resistance of one structure before it is possible to calculate the thermal resistance of the complete plate.

Heat is conducted through both honeycomb walls at the bottom, the foil and the honeycomb wall at the top. A graphical representation of the conduction through the simplified model is shown in Figure 3.16. Honeycomb walls and the foil are indicated with an encircled H and F respectively. The thickness of the two honeycomb walls at the bottom of the structure is only half that of the honeycomb wall at the top. This model can be simplified further by combining the two walls at the bottom and the two foil elements into one part with twice the cross-sectional area. Combining the two parallel parts into a single part results in the model shown in Figure 3.17. This model contains two equal honeycomb walls and a foil that is twice its original thickness. The contact areas between the foil and the honeycomb walls are indicated by red bars. The thermal resistance to solid conduction of the models shown in Figures 3.16 and 3.17 is equal.

The total thermal resistance of the model shown in Figure 3.17 can be calculated by adding the thermal resistances of each part, as shown in Equation (3.4). Thermal resistances of the honeycomb walls and the foil, $R_{honeycomb\,wall}$ and R_{foil} respectively, can be calculated with Equation (3.3). $R_{contact}$ is the resistance in the contact between the honeycomb walls and the foil, which can be calculated with Equation (3.5) [16].

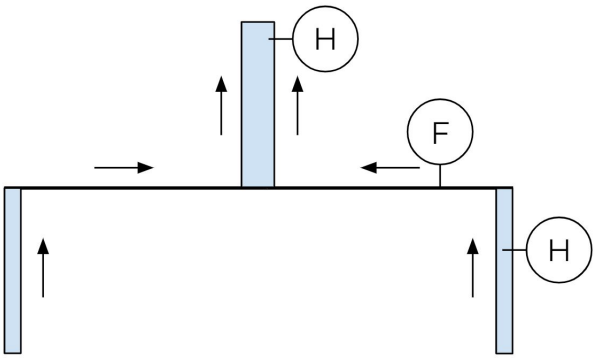

Figure 3.16: Conduction through the simplified model (side view).

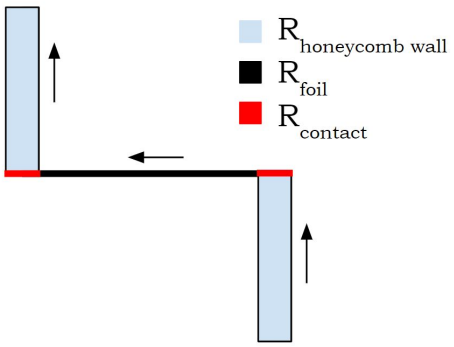

Figure 3.17: Thermal resistances of the simplified model.

$$R_{cond,structure} = 2R_{honeycomb\,wall} + R_{foil} + 2R_{contact}, \quad (3.4) \qquad R_{contact} = \frac{1}{h_i A_{contact}}. \quad (3.5)$$

Where:

h_i = Interfacial conductance [W/m^{2}K]
$A_{contact}$ = Contact area [m^2]

Gaseous conduction

As described in Section 2.2.2, heat transfer caused by gaseous conduction depends on colliding gas molecules that consequently transfer energy. It occurs in the open spaces of the panel. These spaces are bordered by the honeycomb walls, the panel envelope and the intermediate foil. Heat transferred via gaseous conduction influences the conduction, convection and radiation. For the sake of simplicity, the effect of honeycomb walls and the intermediate foil are neglected. The panel is modelled as an empty box with dimensions equal to the panel's dimensions. Furthermore, a one-dimensional case is assumed. Equation (2.5) in Section 2.2.2 shows the relation between the thermal conductivity of air and the air pressure. This air conductivity can be used to calculate the thermal resistance to one-dimensional gaseous conduction with Equation (3.3), repeated below. Here the length and area are equal to the panel thickness and cross-sectional area of the open space inside the panel respectively.

$$R_{conduction} = \frac{L}{k_{air} A} \tag{3.3}$$

Convection

Convective heat transfer decreases when a vacuum is created. The thermal resistance to convection can be calculated with Equation (3.6) [16]. Here, only the heat transfer coefficient varies with changing air pressure. Calculations for this coefficient are shown in Appendix B. Similar to the gaseous conduction calculations, the empty box model is used. This means that the influence of the honeycombs and the foil between the honeycombs are neglected in order to simplify calculations.

$$R_{conv} = \frac{1}{h_c A_{conv}} \tag{3.6}$$

Where:

R_{conv} = Thermal resistance to convective heat transfer [K/W]
h_c = Heat transfer coefficient [$\mathrm{Wm^{-2}K}$]
A_{conv} = Area perpendicular to the flow direction [$\mathrm{m^2}$]

Radiation

In reality, heat radiates from the envelope to the intermediate foil and the honeycomb walls. This influences conductive heat transfer and complicates the model. Therefore, a simplified model is used, where both elements are removed. Radiation for two opposing parallel plates with dimensions equal to the panel dimensions is considered. The thermal resistance to radiative heat transfer for this case is shown in Equation (3.7) [16] and the equations for the surface and space resistance are shown in Equations (2.7) and (2.8) in Section 2.2.2.

$$R_{rad} = \frac{R_{surf,1} + R_{space,12} + R_{surf,2}}{\sigma 4 T_m^3} \tag{3.7}$$

Where:

σ = Stefan-Boltzmann constant = 5.67×10^{-8} [$\mathrm{Wm^{-2}K^{-4}}$]
T_m = Mean temperature of hot and cold surface [K]

Edge losses

The envelope wrapped around the panel core connects the two sides of the vacuum insulation panel. Heat can be conducted through the envelope, around the panel's core, to the other side. This reduces the effectiveness of the entire panel. The thermal resistance to conduction can be calculated with Equation (3.3), repeated below. The envelope consists of multiple layers. Each layer has a specific thickness, thermal conductivity and thermal resistance. Length L and area A in Equation (3.3) are now the panel thickness and the total area perpendicular to the path of conduction respectively. This total area is four times the length of one side of the panel multiplied by the thickness of the layer for which the thermal resistance is calculated. Reality is simplified by only considering one-dimensional conduction through the envelope's layers. Therefore, the thermal resistance of the total envelope can be found by calculating the sum of the inverse of individual resistances for parallel layers with Equation (3.8).

$$R_{conduction} = \frac{L}{kA}, \tag{3.3}$$

$$R_{edge} = \frac{1}{\sum \frac{4k_{layer} w_p t_{layer}}{t_p}}. \tag{3.8}$$

Total thermal resistance

The total thermal resistance of the panel is equal to the sum of reciprocals of the thermal resistance of individual modes of heat transfer, as shown in Equation (3.9).

$$\frac{1}{R_{tot}} = \frac{1}{R_{cond.solid}} + \frac{1}{R_{cond.gas}} + \frac{1}{R_{conv}} + \frac{1}{R_{rad}} + \frac{1}{R_{edge}} \tag{3.9}$$

3.7 Conclusions

The panel is assumed to be square, with its size determined by the panel width. Panel width and panel thickness are the two general parameters. Additional relevant parameters for the honeycomb plates are the honeycomb angle, wall length, wall thickness and cutout height. The only relevant parameter for the foil is the foil thickness. Furthermore, the performance of the panel depends on the materials selected for the honeycomb plates and the intermediate foil. An envelope used for conventional vacuum insulation panels will also be used for the concept panel. The performance of the panel depends on these parameters. Creep and buckling are the relevant failure modes that should be considered for the structural performance of the panel. The thermal performance of the panel can be evaluated by computing the sum of reciprocals of the thermal resistance to the individual modes of heat transfer.

Chapter 4 Detailed design

4.1 Overview

The vacuum insulation panel will be lifted from a conceptually described panel to a fully worked-out design in this chapter. First, the geometry of the panel will be defined. Honeycomb thickness, cutout height and foil thickness will be written as a function of panel thickness and honeycomb wall length. Analytical structural and thermal performance will be calculated with the help of models and equations presented in the previous chapter. A geometry can be found so that optimal performance is reached. Second, materials that ensure optimal performance will be selected per panel part. Third, optimal values for the relevant parameters presented in Section 3.3 are shown. Finally, an overview of manufacturing possibilities will be discussed.

4.2 Dimensions

4.2.1 General approach

Thermal performance depends on the geometry of the panel. All parameters in Section 3.3 are necessary to define this panel's geometry. However, not all of them need to be varied individually to find the optimal panel geometry. The thermal performance will increase for decreasing honeycomb wall thickness, foil thickness and honeycomb cutout height. However, structural requirements pose limits on these parameters. They can therefore be written as a function of the remaining parameters. Panel width and honeycomb angle are assigned a specific value. The reasons for this will be explained in the corresponding sub-sections. Subsequently, honeycomb wall length and panel thickness are the only remaining free parameters. The thermal resistance of the panel can be evaluated and optimised for these two parameters. Honeycomb wall length and panel thickness automatically determine all other parameters.

An optimum exists for maximum thermal performance without panel failure by creep or buckling. Literature-based equations are used to evaluate critical buckling load. Creep is neglected for stresses below two-thirds of the yield strength of the material, as discussed in Section 2.2.3. Higher stress results in higher strain rates, as shown in Figure 2.2 in Section 2.2.3. However, also shown in this figure is that the strain rate only marginally increases for stresses up to 20% higher than two-thirds of the yield strength. Therefore, no additional safety factor is required. This claim will be verified in Chapter 5.

4.2.2 Honeycomb angle

The honeycomb angle influences the distance between honeycomb walls. Therefore, the structural and thermal performance of the honeycomb plates and foil depend on this angle. However, a complete section of the panel will be modelled only with finite element models in Chapter 5. In this project, finite element simulations will be used as a tool for performance evaluation, not for design. Therefore, the optimal angle had to be found based on an iterative process of analytical optimisation and finite element evaluation of the panel geometry. The structural performance of the foil, evaluated with a more complex model than the simplified model used for analytical calculations, determines the honeycomb angle. An optimal angle of 40 degrees was found, as will be explained further in Section 5.2.4.

4.2.3 Honeycomb thickness

Stress in the honeycomb plates will increase when the thickness of the honeycomb walls is decreased. The aim is to find the minimum allowable thickness to ensure maximum thermal performance combined with continuous panel operation. Two different load cases are introduced in Section 3.5: an axial and a transverse load case. The minimum acceptable honeycomb wall thickness can be determined for both load cases separately. One of the two will require a thicker honeycomb wall to ensure continuous panel operation. This thickness will be the active constraint and, therefore, the optimal honeycomb wall thickness for the centre of the panel. The minimum thickness for the axial load case will be calculated first, followed by the minimum thickness for the transverse load case.

Axial load

The simplified model (shown in Figure 3.9 in Section 3.4) is used for the calculation of the required minimum wall thickness. First, the force acting on this structure is calculated with Equation (3.1), which is repeated below. Here $A_{rect,top}$ is the top rectangle of the unit cube explained in Section 3.4. The force acts perpendicular to the horizontal cross-sectional area of the honeycomb walls, which is defined in Equation (4.1). Only creep is relevant for the axial load case, as discussed in Section 3.5. Therefore, the maximum allowable stress in the honeycomb plate is equal to two-thirds of the yield strength. Since the force on the walls is known too, the minimum required cross-sectional area of the honeycomb wall can be calculated with Equation (4.2). Substituting Equations (3.1) and (4.2) in Equation (4.1) and rewriting for the honeycomb thickness results in Equation (4.3). Note that the external air pressure and the yield strength of the material are constant and that the top rectangle of the unit structure is a function of the honeycomb plate geometry. Consequently, the honeycomb wall length is the only relevant parameter that influences the honeycomb walls' thickness.

$$F_{top} = p_{ext} A_{rect,top}, \tag{3.1}$$

$$A_{h,top} = l_h t_h. \tag{4.1}$$

$$A_{h,top} \geq \frac{F_{top}}{\sigma_{y,h}}, \tag{4.2}$$

$$t_h \geq \frac{p_{ext} A_{rect,top}}{2/3 \sigma_{y,h} l_h}. \tag{4.3}$$

Where:

t_h = Honeycomb wall thickness [m]
$\sigma_{y,h}$ = Yield strength of honeycomb material [Pa]
$A_{h,top}$ = Horizontal cross-sectional area of the honeycomb wall (viewed from the top) [m^2]

Transverse load

Contrary to the axial load case, diagonal walls are relevant for the transverse load case. Both vertical and diagonal walls can fail due to buckling or creep, as discussed in Section 3.5. An analysis of both failure modes and which is dominant will be presented. Creep failure will be discussed first.

Klintworth et al. provide equations usable for evaluating stress at individual walls for a honeycomb plate with external loads σ_x, σ_y and τ_{xy}, shown in Figure 4.1a. Figure 4.1b shows a single honeycomb from this plate. Loads on individual walls AB, BC and BD are shown in Figure 4.1c. Stress in honeycomb plate walls is not allowed to exceed two-thirds of the yield strength of the material, as discussed in Section 2.2.3. Axial load on diagonal walls AB and vertical wall BD can be calculated with Equations (4.4) and (4.5) respectively [26]. Equal and opposite moments acting on the ends of the diagonal walls can be calculated with Equation (4.6) [26]. For readability, the parameters l_h and h_h are replaced by L and h respectively.

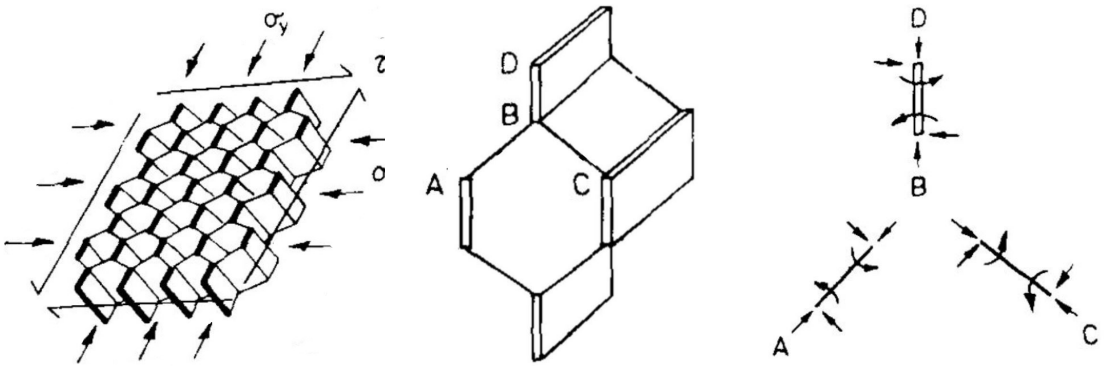

(a) Honeycomb load conditions [26].

(b) A single honeycomb from the complete panel with indicated A, B, C, D [26].

(c) Loads on individual honeycomb walls [26].

Figure 4.1: Geometry and loads from Klintworth et al. [26].

Transverse loads σ_x and σ_y are both equal to the atmospheric pressure and the applied shear τ_{xy} is zero for the operating conditions of the vacuum insulation panel. Because the shear load is zero, no moment is acting on the vertical walls. Furthermore, the magnitude of the axial load and moment acting on diagonal walls BC and AB are equal. According to Klintworth et al., stress is maximum at the ends of the diagonal walls and bending moment M_{AB} is zero at the centre of the honeycomb wall. These claims will be verified in Chapter 5. The minimum required honeycomb wall thickness to prevent creep failure at this location can be calculated with Equation (4.7). Appendix G shows how this formula is derived.

$$P_{AB} = -\sigma_x h(L + L\sin\theta)\cos\theta - \sigma_y hL\cos\theta\sin\theta - \tau_{xy}h(L + L\sin\theta) \tag{4.4}$$

$$P_{BD} = 2\sigma_y hL\cos\theta \tag{4.5}$$

$$M_{AB} = [\sigma_x hL(L + L\sin\theta)\sin\theta - \sigma_y h(L\cos\theta)^2 - \tau_{xy}hL^2\cos\theta]/2 \tag{4.6}$$

$$t_{h,ends} \geq \frac{3\left(P_{AB} + \sqrt{P_{AB}^2 + 16\sigma_{y,h}hM_{AB}}\right)}{4\sigma_{y,h}h}, \tag{4.7}$$

$$t_{h,middle} \geq \frac{3k_{cutout}P_{AB}}{2\sigma_{y,h}(1 - f_c)h}. \tag{4.8}$$

Equations (4.4) to (4.7) hold for fully intact honeycomb plates. However, cutouts have been made in the diagonal walls of the honeycomb plate of the vacuum insulation panel concept. Height is minimum at the centre of the honeycomb wall. The question arises whether the location of critical stress will shift from the end to the middle of the honeycomb walls due to the cutouts. A sharp notch generates a stress concentration in the material. This stress concentration can be reduced by rounding the sharp tip of the cutout. Therefore, diagonal walls with filleted notches are preferred. However, the manufacturability of filleted cutouts still need to be examined. A worst case, and therefore safe, estimation of the stress concentration is provided by evaluating sharp cutouts. Besides, Savruk et al. [27] provide data for analytically estimating the stress at a sharp notch tip for the geometry shown in Figure 4.2. The geometry of the specimen shown in Figure 4.2 can be chosen such that it is comparable to the honeycomb plate's diagonal walls.

Savruk et al. multiply the axial load on the specimen, indicated by p in Figure 4.2, by a stress concentration factor k_{cutout} to estimate the stress at notch tip. The calculated moment M_{AB} is zero at the centre of the honeycomb wall. Therefore, only axial load P_{AB} is relevant at this location. Consequently, this axial load can be multiplied by stress concentration factor k_{cutout}. High values of k_{cutout} are expected since the axial load, and not a stress estimate, is multiplied by stress concentration factor k_{cutout}. The minimum wall thickness required to eliminate creep failure at the middle of the diagonal honeycomb wall can be calculated with Equation (4.8). Equation (4.8) follows from Equation (4.7) for bending moment $M_{AB} = 0$ and wall height denoted as a fraction f_c of the initial honeycomb wall height.

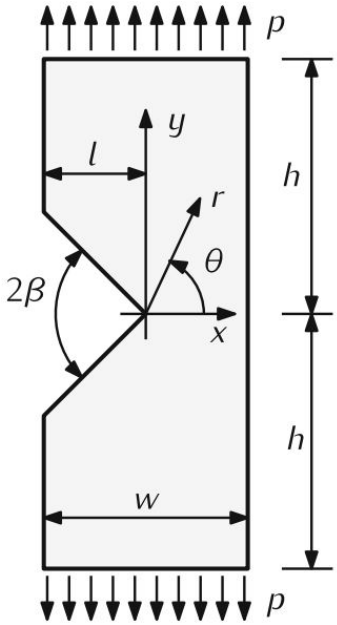

Figure 4.2: Geometry of an axially loaded specimen with symmetrical V-shaped notch [27].

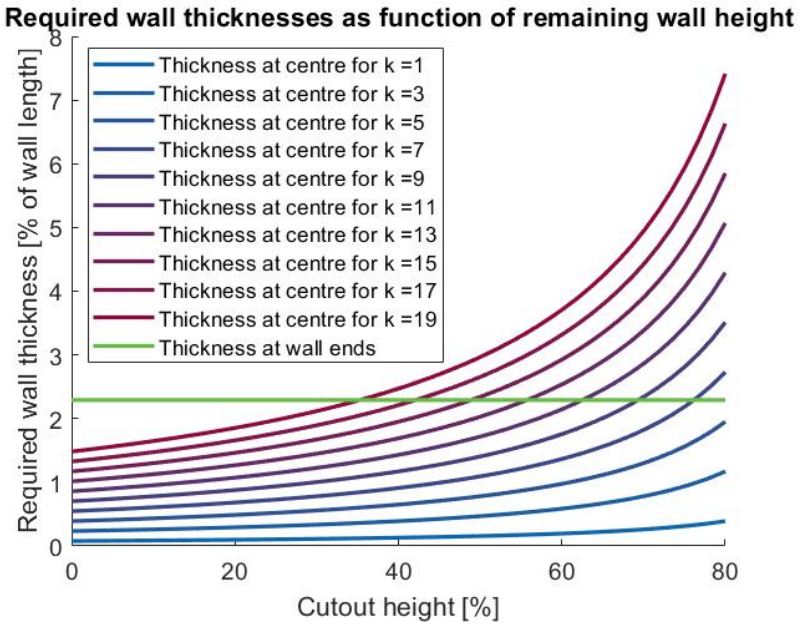

Figure 4.3: Minimum required thickness at the honeycomb wall's end compared to the centre, where stress concentration factor k influences the required thickness at the wall's centre.

The exact value of the stress concentration factor will be determined in Section 4.2.4 since it is linked with the honeycomb cutout height. However, Equation (4.8) can be evaluated for a range of stress concentration factors and honeycomb cutout heights. Figure 4.3 shows the required thickness at the centre of the diagonal walls compared to the required thickness at the ends of the walls. The required thickness at the wall ends can be calculated with Equation (4.7) and is not affected by the notch. The stress at the centre of the honeycomb walls becomes dominant over the stress at the wall ends for high stress concentration factors and cutout height. However, until this happens, reducing the remaining wall height does not affect the required wall thickness. Optimal honeycomb cutout height is, therefore, equal to the location where the two lines intersect. Thus, the honeycomb thickness at the location of the notch and at the ends of the walls are equal for optimal honeycomb cutout height. Therefore, calculating minimum thickness with Equation (4.7) suffices. Finding the optimal cutout height is the subject of the following subsection.

Analogous to creep, the minimum required wall thickness to prevent buckling can be calculated. Equations for buckling are shown in Appendix I. The required thickness to eliminate creep and buckling are shown in Equation (4.7) and Equation (I.1) in Appendix I respectively. Figure 4.4 shows the minimum thickness of the honeycomb plates for creep and buckling as a function of the

external pressure for a fixed honeycomb wall length of 22 mm and honeycomb plate height of 5 mm. Buckling becomes the dominant failure mode for external pressure below 10^3 Pa. However, the external air pressure is equal to 10^5 Pa. Minimum required thickness to eliminate creep is higher than the required thickness for buckling at this air pressure. Therefore, creep is the dominant failure mechanism for the specified geometry. The point where the creep and buckling lines in Figure 4.4 intersect depends on the honeycomb plate height (which is half the panel thickness, as discussed in Section 3.3), as shown in Figure 4.5. Creep is the dominant failure mechanism up to a honeycomb plate height of roughly 13 mm (a panel thickness of 26 mm), where the blue line in Figure 4.5 crosses the dashed line, representing the external air pressure. The honeycomb wall length also affects failure modes. Figure 4.6 shows the minimum required honeycomb wall thickness for multiple failure modes for a ranging honeycomb wall length and an external pressure of 10^5 Pa. Creep can occur in the diagonal and vertical walls due to axial or transverse load. However, creep in the diagonal walls is dominant over all other failure modes for panel thickness lower than 26 mm.

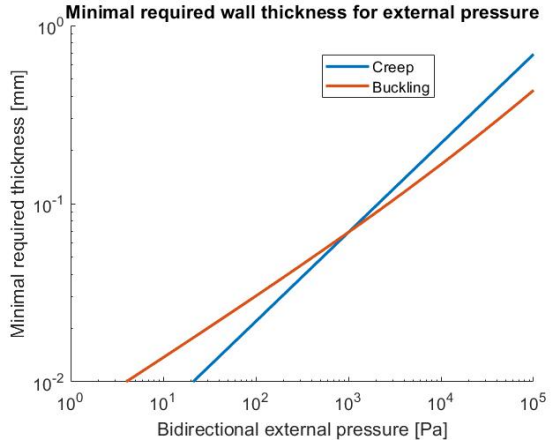

Figure 4.4: Minimum required honeycomb wall thickness for creep and buckling as function of external air pressure for a honeycomb wall length of 22 mm and a honeycomb plate height of 5 mm.

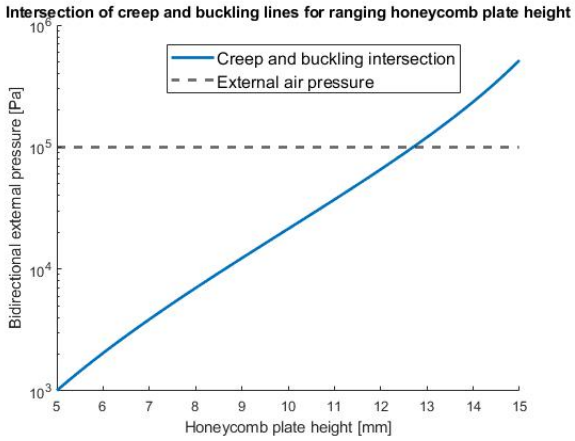

Figure 4.5: Point where the creep and buckling lines, shown in Figure 4.4, intersect for a ranging honeycomb plate height for a honeycomb wall length of 22 mm.

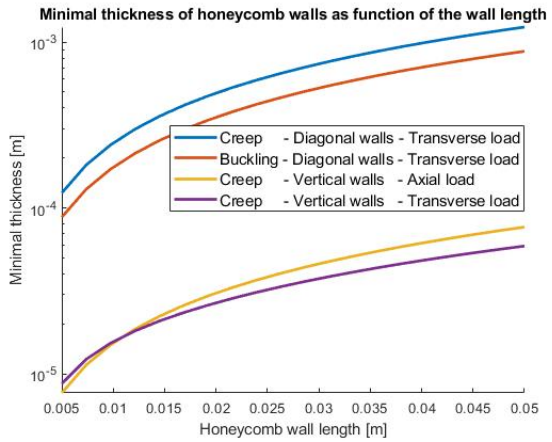

Figure 4.6: Minimum required wall thickness for multiple failure modes as function of honeycomb wall lengths for bidirectional external pressure of 10^5 Pa and a honeycomb plate height of 5 mm.

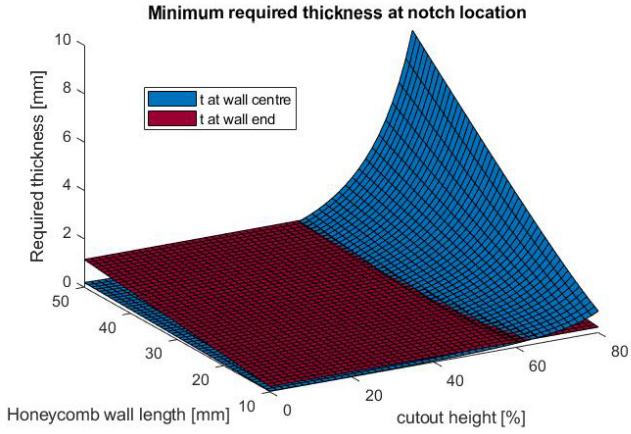

Figure 4.7: Minimum required wall thickness for two locations based on geometry parameters.

4.2.4 Honeycomb cutout height

The required thickness at the diagonal wall's end and centre, calculated with Equations (4.7) and (4.8) respectively, are equal for optimal cutout height. Figure 4.3 shows a range of possible combinations of the stress concentration factor and cutout height. Savruk et al. provide stress concentration factors for combinations of the cutout fraction l/w and notch angle 2β (l , w and 2β are indicated in Figure 4.2). The width of the notch is set equal to the total width of the diagonal honeycomb wall ($2h$ in Figure 4.2), as mentioned in Chapter 3. Therefore, notch angle 2β is a function of l/w and honeycomb wall length l_h, as shown in Equation (F.2) in Appendix F. Subsequently, the stress concentration factor and the required thickness at the centre of the honeycomb wall can be written as a function of honeycomb wall length and cutout height (or cutout fraction). A more elaborate derivation of this method can be found in Appendix F. Figure 4.7 shows the required thickness at wall ends (red), based on Equation (4.7), and at the walls' centre (blue). Appendix F discusses how the blue surface is obtained. Optimal cutout height, or where the red and blue surfaces intersect, ranges between 52% and 64% of the total honeycomb wall height. Larger cutouts are possible. However, thickness will increase significantly, especially for larger honeycomb wall lengths.

4.2.5 Foil thickness

The compressive external air pressure induces stress in the foil. Figure 4.8 shows a side view of the simplified model, similar to Figure 3.16 in Section 3.4. Two states are shown in Figure 4.8: the rest state (in red), where no deflection occurs, and the loaded state (in blue), where deflection does occur. It is possible to use only one of the two sides to determine the necessary foil thickness since the simplified model is symmetric. In this case, the right half is used. Consequently, the external force is divided by two. Creep failure is the dominant failure mechanism for the foil.

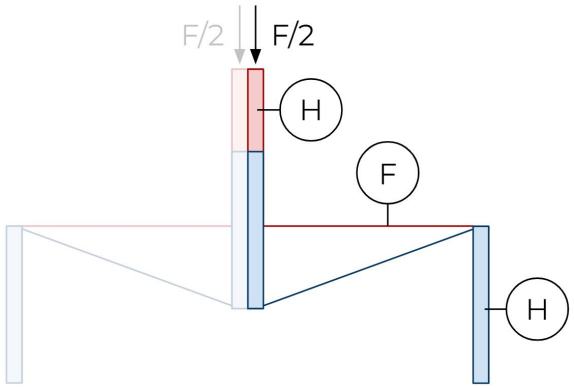

Figure 4.8: Deflection and symmetry shown on side view of the simplified model.

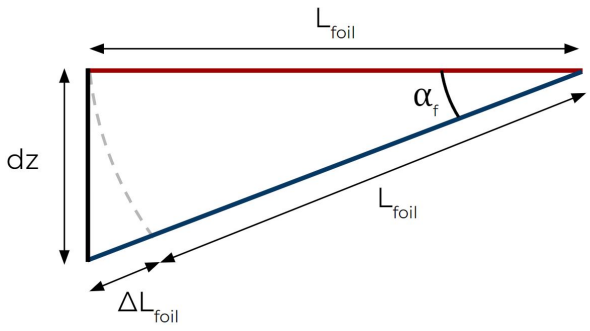

Figure 4.9: Displacement of a deflecting foil.

Therefore, maximum stress in the foil is equal to two-thirds of the yield strength of the material. The foil elongates by ΔL_f due to external loading, as shown in Figure 4.9. Foil angle α_f, vertical deflection dz and the minimum required foil thickness t_f can be calculated with Equation (4.9), Equation (4.10) and Equation (4.11) respectively. Derivations of these equations and L_{foil} can be found in Appendix G.

$$\alpha_f = \cos^{-1} \frac{3E_f}{2\sigma_{y,f} + E_f}, \quad (4.9) \qquad dz = \tan(\alpha_f) L_{foil}, \quad (4.10) \qquad t_f = \frac{3F_{top}}{4 \sin(\alpha_f) \sigma_{y,f} l_h}. \quad (4.11)$$

Contactless foil deflection is critical for the panel's insulating performance. Foil deflection dz can therefore only be a fraction of the honeycomb cutout height. This maximum is set to the honeycomb cutout height divided by a geometric safety factor SF_g. If the foil deflects further than this maximum, the required thickness is calculated again with the deflection set to the maximum allowable deflection. Foil thickness will increase to a point where acceptable deflection occurs.

Foil thickness can also be too thin. Optimal foil thickness depends on the size of the honeycombs. For smaller wall lengths, optimal foil thickness can be in the order of micrometres. Basalt fibre will be selected for the foil, as will be discussed in Section 4.3. The minimum diameter of a single basalt fibre is 6 micrometres [28]. The minimum thickness of a woven fabric made from these fibres is equal to 12 micrometres. Therefore, the minimum allowable foil thickness is set to 12 micrometres.

4.2.6 Panel width

How the panel influences the thermal performance of the panel, which will be discussed in the coming subsections, will be the subject of this subjection. A graphical overview of the R-value of each mode of heat transfer individually and the total panel as a function of panel width is shown in Figure 4.13 in Section 4.2.8. This figure shows that panel width influences thermal resistance to radiation and edge losses.

As mentioned in Section 3.6, the radiative thermal resistance is calculated for an empty, evacuated box with outer dimensions equal to the panel dimensions. Panel width can be found in the form factor in Equation (3.7). Changing the panel width will affect the form factor and thereby the thermal resistance to radiative heat transfer. However, the effect on the total panel performance is relatively small. The R-value for radiative heat transfer for a square-metre panel is 2% lower than for a square-centimetre panel. The dependency of thermal resistance to edge effects on panel width is much larger. Edge effects are present for all panel geometries. However, changing panel size influences the ratio of panel edge to panel area. The thermal performance of a panel with relatively more edge suffers more from edge losses. Therefore, edge effects become relatively larger for smaller panel sizes. The edge losses R-value of a square metre panel is roughly 72% larger (thus better) compared to a square decimetre panel.

The panel should be as large as possible for optimal performance. However, theoretical optimisation of the panel width is not helpful since the eventual panel size is probably heavily influenced by external demands instead of calculated theoretical performance. Transport and application efficiency both influence the ideal panel size. However, these additional wishes fall outside this report's scope and will not be discussed in more detail. Therefore, the panel width will be assumed to be equal to one metre.

4.2.7 Panel thickness and honeycomb wall length

All parameters discussed above can be written as a function of panel thickness or honeycomb wall length. Once these parameters are assigned a value, the geometry of the entire panel is determined. Values for the remaining parameters follow from an optimisation of the panel performance. However, materials need to be chosen for the panel parts before the panel's thermal performance can be estimated. Although an extensive explanation of the material selection will be discussed in Section 4.3, stainless steel honeycomb plates and woven basalt fibre foil are assumed for this analysis.

4.2.8 Analytical thermal performance and optimisation

Therefore, optimal panel thickness and honeycomb wall length should be selected for high performance relative to the conventional VIPs. The R-value of conventional vacuum insulation panels as a function of the panel thickness is determined in Appendix H. The R-value and relative R-value of the panel (compared to current VIPs) as a function of the honeycomb wall length and panel thickness are shown in Figures 4.10 and 4.11. Unfortunately, the shape of surfaces in Figures 4.10 and 4.11 can not be observed when they are orientated equally. Therefore, the surface in Figure 4.11 is rotated anti-clockwise by 90 degrees. This graph shows an optimum relative thermal performance for a panel thickness of 10 millimetres and honeycomb wall length of 22 millimetres. All other parameters can now be calculated by substituting these values in the presented equations in this chapter.

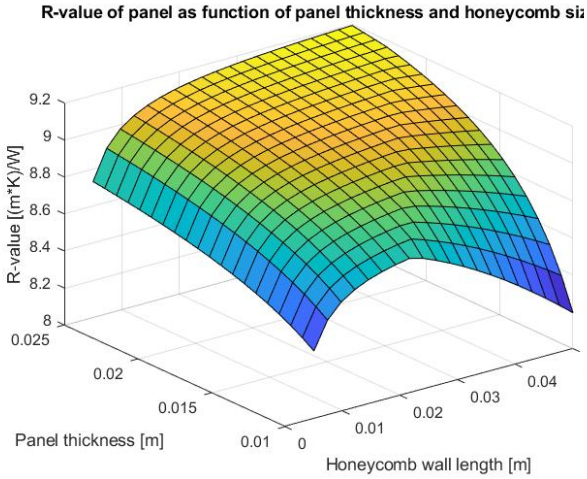

Figure 4.10: Analytically calculated R-value of a panel with stainless steel honeycomb plates and a woven basalt fibre foil as function of panel thickness and honeycomb wall length.

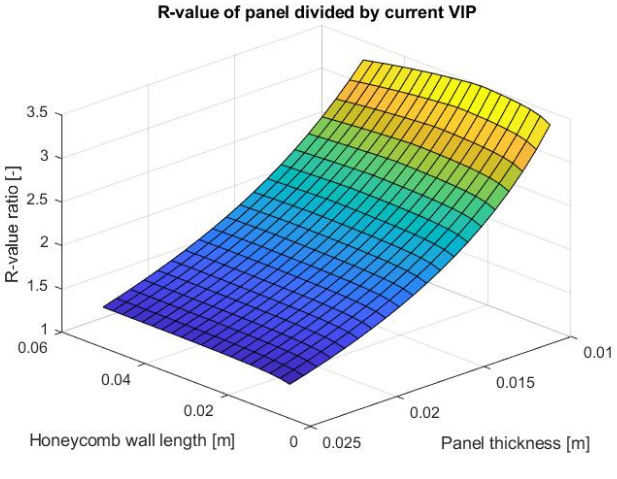

Figure 4.11: R-value of the concept (analytical) divided by a current VIP of equal thickness as function of panel thickness and honeycomb wall length.

Figure 4.12 shows the thermal resistance of each mode of heat transfer for the optimal panel geometry. The total thermal resistance is strongly influenced by the mode of heat transfer with the lowest thermal resistance. Gaseous conduction and convection are dominating heat transfer modes for pressures close to ambient air pressure. When reducing pressure, four things happen. First, at an internal pressure of around $2.5{\cdot}10^{3}$ Pa, the line of convective heat transfer in Figure 4.12 disappears. Convection occurs only for temperatures or pressures above a certain critical value [16]. Below this critical temperature or pressure, heat is transferred through the medium via pure conduction. The internal pressure required for the new panel concept to reach optimal performance lies around 10^{-3} Pa, which is far below the critical pressure. Therefore, convective heat transfer will from hereon be neglected. Second, the thermal resistance to gaseous conductive heat transfer starts to go up significantly at a pressure of around 10 Pa. Third, at a pressure of around 0.1 Pa, thermal resistance to radiative heat transfer becomes the dominant mode of heat transfer. Total thermal resistance is therefore determined mainly by the thermal resistance to radiation. Figure 4.12 shows this effect by the convergence of the light blue total thermal resistance line to the purple thermal resistance to radiation line. Fourth, the total thermal resistance barely changes for pressures below 10^{-3} Pa. Therefore, further reduction of the internal air pressure is not helpful.

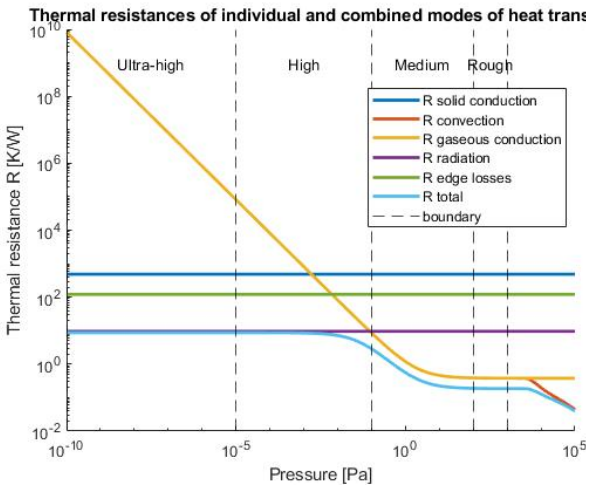

Figure 4.12: Analytically calculated thermal resistance R per mode of heat transfer for a panel thickness of 10mm and honeycomb wall length of 22mm.

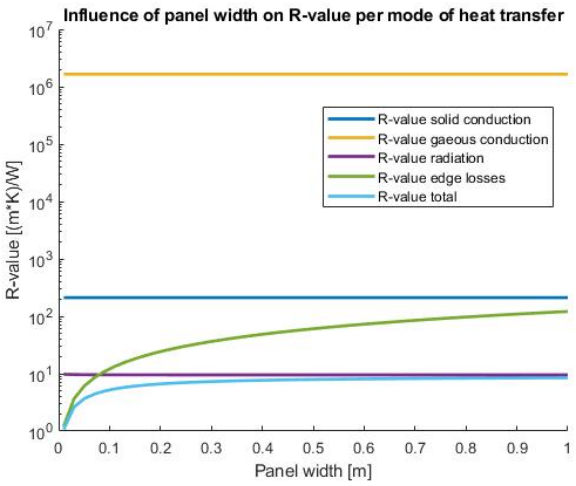

Figure 4.13: Influence of panel width on analytically calculated R-values of individual heat transfer modes heat transfer and total system for a panel thickness of 10mm and honeycomb wall length of 22mm.

Optimising geometry and material for the honeycomb plates and intermediate foil can change the resistance to solid conduction and edge losses, but barely affects gaseous conduction and radiative heat transfer. Optimising the current geometry might not seem helpful since heat transfer is dominated by radiative heat transfer. However, filling the openings in the honeycomb plates with Multi-Layer Insulation (MLI) can drastically reduce heat transfer by radiation [29–32]. A future high-performance product will probably contain these added MLI infills. Optimising the current panel's geometry will prove to be helpful if radiative heat transfer is reduced to a point where it is comparable to or higher than thermal resistance to edge losses and solid conduction.

4.3 Material selection

4.3.1 Material requirements

Requirements can be imposed on the materials used for the honeycomb plates. First, it is essential to select a non-flammable material so the panel can be used safely. Second, a recyclable material with a low carbon footprint should be selected. Existing vacuum insulation panels have a considerable environmental impact, as discussed in Appendix J.4. Third, materials with a sufficiently low vapour pressure at operating conditions should be selected. vapour pressure is the ambient pressure at which a material or an element starts vaporising [33]. A material will slowly transform from a solid into a gas if the ambient pressure is lower than the vapour pressure for that material at a specific temperature. This phase transition reduces the effectiveness of the vacuum and can eventually lead to the failure of the panel. The vapour pressure increases with temperature. A graph of the vapour pressure of some materials for ranging temperatures is shown in Figure K.1 in Appendix K. Ambient pressure of 10^{-5} Pa and a temperature of 50 °C are assumed as operating conditions. An overview of materials or elements with an insufficiently high vapour pressure is shown in Table K.1 in the same Appendix. Materials selected for the panel parts cannot contain any listed elements. The final requirement is that the material should be able to resist creep failure. Consequently, the yield strength should be maximised and the melting temperature should be higher than 2.5 times the operating temperature. A maximum operation temperature of 323 K (50°C) translates to a required melting temperature of at least 807.5 K or 534.5°C.

4.3.2 Material selection approach

Four properties of the panel parts can be minimised: overall heat transfer, environmental impact, cost and weight. Material indices, which show the relevant relation of material properties, are shown in Table 4.1 for each optimisation direction. The performance of materials is optimal for minimised material indices. Furthermore, recyclability, non-flammability, a minimum melting temperature of 534.5°C and composition containing zero per cent of the non-suitable materials listed in Appendix K are material constraints that hold for all materials.

Heat transfer	Environmental impact	Cost	Weight
$M_1 = \frac{k}{\sigma_y}$	$M_2 = \frac{CO_2/kg}{\sigma_y}$	$M_3 = \frac{C}{\sigma_y}$	$M_4 = \frac{\rho}{\sigma_y}$

Table 4.1: Material indices for per optimisation goal.

How much the panel's performance is affected by a reduction of a specific material index differs per panel part. Take, for example, the minimisation of overall heat transfer. Equation (3.3) in Section 3.6 shows that solid conduction depends on geometrical properties (L/A) and the thermal conductivity (k). The geometrical thermal resistance (thermal resistance independent of material parameters) of the honeycomb walls and foil equals 436.32 m^{-1} and 8139 m^{-1} respectively. Materials with a low thermal conductivity increase the thermal resistance to solid conduction for both parts. However, selecting a material with low thermal conductivity for the foil is more effective since its geometrical thermal resistance is 19 times higher. The total thermal resistance to solid conduction through the simplified model is high when the thermal resistance to either one of the two parts is high since the parts are in series, as shown in Equation (3.4) in Section 3.6. Environmental impact and the material cost are more relevant for the honeycomb plates than the foil since more material will be used for the plates. Panel weight reduction is only relevant if the panel will be used in the transport industry. Furthermore, it is unimportant for the thin foil since its mass is negligibly small, regardless of its density. Therefore, only the first three material indices shown in Table 4.1 will be considered for the foil material.

4.3.3 Material selection for the honeycomb plates

Ashby graphs can be constructed for each material index. These are shown in Figures L.1 to L.4 in Appendix L. The solid black lines in these graphs represent points of equal material index value. Moving the line down decreases the material index value. The optimal point for each graph lies in the bottom right-hand corner of the graph since optimal materials can be found by minimising material indices. Two materials are located in the bottom right corner of all graphs: titanium and stainless steel. Aluminium is indicated for reference. All graphs show titanium and stainless steel performing comparable to or better than aluminium. Therefore, aluminium will not be discussed further.

Based on thermal performance and density, titanium is the best material for the part. However, titanium is also relatively expensive and has a large CO_2 footprint compared to steel. Besides, solid conduction is not limiting panel performance in the current version of the concept panel, as shown in Figure 4.12 in Section 4.2.8. Therefore, stainless steel is a better-suited material for the current panel. Titanium might be a usable material for a more high-performance and expensive panel in the future. Some steels have thermal and weight performance comparable to titanium. However, these steels are categorised as tooling steels since they are mostly used for manufacturing tools. The processing properties of those steels are relatively poor. A more conventional stainless steel is selected to avoid manufacturing problems of the panel.

4.3.4 Material selection for the foil

Appendix M shows the Ashby graphs for the three relevant material indices in Figures M.1 to M.3. Basalt fibre is the best overall foil material compared to all other materials. Some materials perform better in primary energy consumption or price divided by yield strength, but they have significantly higher other material indices. Fabrics can be woven from basalt fibres to create a robust cloth that can be placed between the two honeycomb plates. A fibre thickness as low as six µm is achievable [28]. A cloth is not the same as a foil. However, the part between the two honeycomb plates will still be referred to as the foil for clarity.

4.3.5 Material selection for the envelope

The primary purpose of the envelope is to create an airtight layer around the core material. Even with a fully sealed layer, air and water vapour can slowly diffuse through the barrier into the core. A thick aluminium barrier is ideal for countering this permeation [12]. However, using a fully metal envelope results in undesired, high conduction. This allows heat to travel through the envelope around the panel, which can significantly reduce the overall effectiveness [12, 34].

Actual envelopes comprise multiple layers of aluminium and various polymers. These metallised film (MF) envelopes can be composed in many forms. The so-called MF2 envelope establishes the best balance between a low permeation rate and a low conductivity through the envelope. This envelope will be used for the construction of this panel envelope. A complete substantiation for selecting the MF2 envelope can be found in Appendix D.

4.3.6 Material properties

Materials that should be selected for the first product for the honeycomb plates and foil are stainless steel and basalt fibre respectively. Many stainless steel types are suitable. For simplicity's sake a single stainless steel type is selected: Stainless steel, austenitic, AISI 302, HT grade C. Titanium remains relevant because it could prove to be a usable plate material in the future. A selection of mechanical properties of the three materials of interest is shown in Table 4.2. Values of the material indices (shown in Table 4.1) are shown in Table 4.3. Basalt fibre has the lowest material index for all material indices. However, M_4 is not relevant for the foil material.

Material	Yield strength (Gpa)	Melting point ($\cdot 10^3$ °C)	Thermal conductivity (W/(mK))	Price ($\cdot 10^3$ EUR/m^3)	CO_2 (kg/kg)	Density ($\cdot 10^3$ kg/m^3)
Stainless steel	0.52-0.76	1.40-1.42	15-17	19.1-25	3.16-3.74	7.81-8.01
Titanium	1.1-1.16	1.63-1.66	8.3-8.5	107-133	21.3-26.2	4.80-4.82
Basalt fibre	1.43-4.9	1.41-1.49	0.030-0.038	5.06-6.44	0.0543-0.0600	2.50-2.89

Table 4.2: Material properties of three materials of interest for panel construction.

Material	M_1 - Thermal conductivity ($\cdot 10^{-9}$)	M_2 - Environmental impact ($\cdot 10^{-9}$)	M_3 - Cost ($\cdot 10^{-6}$)	M_4 - Density ($\cdot 10^{-6}$)
Stainless steel	29	6.1	41	15
Titanium	7.6	19	97	4.4
Basalt fibre	0.021	0.039	3.5	1.8

Table 4.3: Material index values of three materials of interest for panel construction.

4.4 Final parameters

All parameters that define the optimal geometry of the panel are listed below.

1. Honeycomb angle, $\theta = 40$ degrees
2. Panel thickness, $t_p = 10$ mm
3. Panel width, $w_p = 1$ m
4. Honeycomb wall length, $l_h = 22$ mm
5. Honeycomb thickness, $t_h = 0.53$ mm
6. Honeycomb cutout height, $h_{cutout} = 3.3$ mm
7. Foil thickness, $t_f = 45$ µm
8. Envelope type = MF2 foil
9. Honeycomb material = Stainless steel
10. Foil material = Basalt fibre
11. Geometric safety factor, $SF_g = 1.5$

4.5 Manufacturing

4.5.1 General approach

An analytical evaluation of the panel performance has been presented based on relevant parameters and material properties. However, it is crucial for the realisation of the concept that the panel is manufacturable. Furthermore, a higher vacuum compared to conventional VIPs is required for the panel concept. A vacuum can be established by pumping air out after panel manufacturing or manufacturing the panel in a vacuum chamber. An estimation of the required time for this higher vacuum shows whether it is feasible to use vacuum pumps. The mentioned aspects will be presented in this section. However, the presented results are only meant to indicate manufacturing possibilities rather than a complete evaluation of all aspects that play a role in the manufacturing process.

4.5.2 Honeycomb plate manufacturing

Many techniques exist for honeycomb plate manufacturing, but expanded, adhesive-bonded produced plates are most common [35]. This manufacturing process is graphically represented in Figure 4.14. It starts with a sheet of material. An adhesive is applied in lanes on this sheet of material. An identical new sheet is then placed on the already present sheet. The applied adhesive bonds the two together. This process is repeated until a desired amount of plate is reached. This stacked sheet block is called a HOBE (HOneycomb Before Expansion) block. The last step is pulling the top and bottom sheets of the block apart. This process is called expanding. The honeycomb walls deform plastically near the areas where adhesive is applied, causing the honeycomb structure to retain its shape when expansion stops.

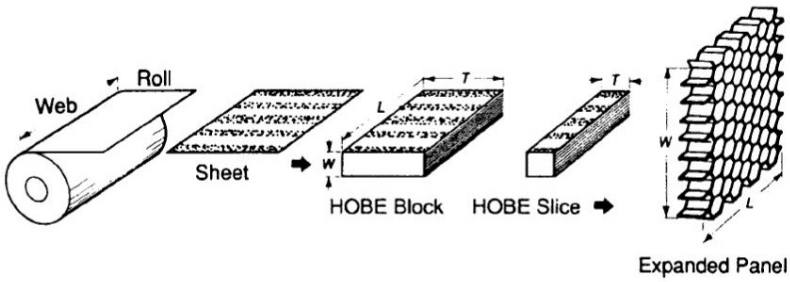

Figure 4.14: Manufacturing process of adhesive-bonded, extruded honeycomb plates [35].

The v-shaped notches required for panel operation can be made during three stages of the manufacturing process. The first option is to make cutouts in individual sheets. These modified sheets can be stacked to create a HOBE block. The second option is to create a HOBE block first and vertically machine rows of cutouts at once. The final option is to expand an intact panel first. Thereafter, incisions can be made.

All cutout processes have advantages and disadvantages. Milling the HOBE block is probably the fastest, but walls can bend during milling. Removing material in the sheet phase can be done accurately by, for example, laser cutting or punching without risk of deformation. However, because all sheets are manufactured individually, this process is slower. As mentioned before, expansion relies on the plastic deformation located at the ends of the diagonal walls. Removing parts of the diagonal walls before expansion might cause the diagonal walls to deform plastically in the centre of the walls. If this happens, no honeycomb plate can be produced. This risk is removed when incisions are made after the expansion phase. However, cutting the diagonal walls in the expanded form can be challenging since they are most vulnerable in this phase. Furthermore, slight misalignment of the diagonal walls can occur during expansion. Created notches can be misaligned if part of the walls is removed by milling in straight lines, causing opposing plates to make contact. Further research should be done to show what manufacturing process is feasible for the cutouts.

4.5.3 Assembly

The vertical honeycomb walls (defined in Section 3.4) need to be connected to the intermediate foil. This can be established with an adhesive or by a mechanical bond. Adhesive-bonding is the most promising manufacturing technique since it is fast, cheap and requires no extra parts. The selected adhesive must not contain any critical materials shown in Appendix K. Like conventional vacuum insulation panels, a vacuum is created in the core and the panel envelope is wrapped around the panel core to seal it [36]. However, the vacuum required for the vacuum insulation panel concept is higher (10^{-3} Pa) compared to the vacuum required for the conventional panels (10^{2} Pa). Creating a higher vacuum takes more time, so the question arises if it remains feasible to pump air out or whether the entire assemblage should be done in a vacuum chamber. The air pressure in this chamber is maintained at the required internal air pressure of the panel. This will be discussed in the following subsection.

4.5.4 Panel Evacuation

Pumping the air out is preferred since it is easier and less expensive. How quickly a panel can be evacuated depends on the panel conductance and the pumping speed of the pump connected to the panel. If both are known, the effective pumping speed can be calculated. Subsequently, the pumping time required to evacuate a specific volume can be established. First, the conductance of the panel will be determined. Second, pumps and their pumping speed will be discussed. Finally, the effective pumping speed and the required pumping time can be calculated.

Conductance

Conductance is a measure of how easily air (or any other gas or liquid) moves through a channel. When the geometry of the channel changes, the conductance changes as well. Besides geometry, conductance through a channel also depends on the dominant flow type. The flow type depends on the Knudsen number, which depends on the air pressure. Three flow regimes exist: viscous flow, molecular flow and Knudsen flow. Knudsen flow is a combination of viscous and molecular flow [33]. Figure 4.15 shows the pressure ranges at which each flow regime is active.

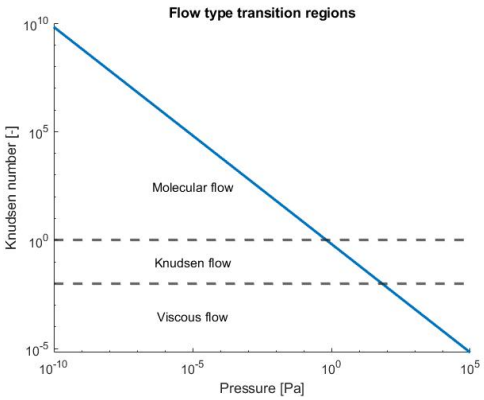

Figure 4.15: Flow regimes based on air pressure.

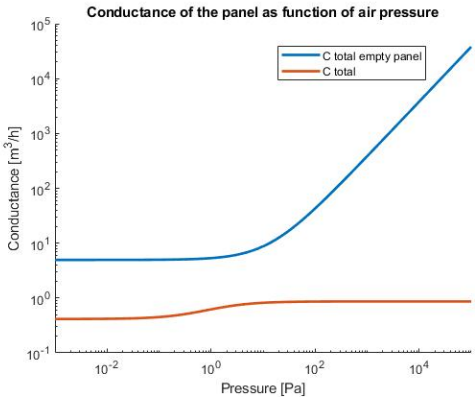

Figure 4.16: Conductance of the panel and an empty panel.

Analogous to structural and thermal calculations discussed at the beginning of this chapter, total conductance can be calculated for the panel's geometry. Again, the unit structure, introduced in Section 3.4, can be used to simplify the total panel. The conductance of a unit volume that contains a unit structure can be calculated. Subsequently, the conductance of the panel can be calculated. All conductance calculations are shown in Appendix N. The conductance of the panel and an empty box with outer dimensions equal to the panel are shown in Figure 4.16. This graph shows that the core lowers the total conductance by at least a factor of ten.

Working range and pumping speed

This report aims to acquire an indication of the time required to evacuate the panel up to an internal air pressure of 10^{-3} Pa, not to generate a full overview of all possible pumps and the associated performances. Therefore, only one pump combination has been considered: a single-stage rotary vane primary pump and a molecular drag pump (MDP) as a secondary pump. The working range of the rotary vane pump lies between ambient air pressure and 0.1 Pa [33]. The MDP has a working range from 10 Pa to 10^{-4} Pa. Combining these two pumps makes it possible to achieve the required final pressure.

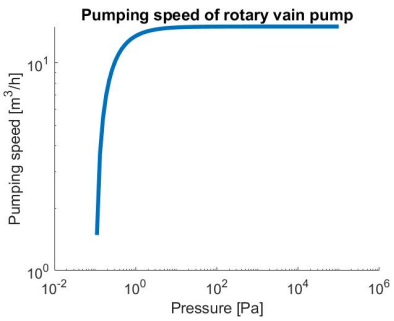

Figure 4.17: Pumping speed of a rotary vane pump as function of pressure.

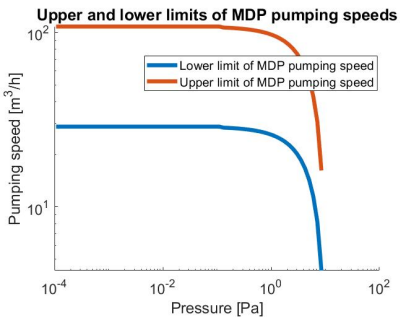

Figure 4.18: Pumping speed of a molecular drag pump as function of pressure.

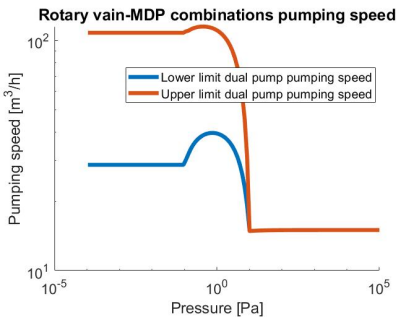

Figure 4.19: Pumping speed of a rotary vane - MDP combination as function of pressure.

Besides the working range, the speed of the selected pumps is essential. A vacuum pump's pumping speed is defined as the removed volume of gas per unit time [33]. The pumping speed of a pump is measured at the pump's inlet and is approximately equal to its nominal pumping speed for most of the working range. However, it drops down near the boundaries of the working range until it is equal to zero for air pressures outside the working range. The nominal pumping speed of a rotary vane pump is 15 m^3/h and the MDP's speed lies between 28.8 m^3/h and 108 m^3/h [33]. The actual pumping speeds of the pumps are shown in Figures 4.17 and 4.18. Figure 4.19 shows the pumping speeds of the two pumps combined. Note that the pumping speed is not the same as the amount of removed gas, which can be obtained by multiplying the pumping speed by the pressure of the medium. Therefore, the MDP does not necessarily pump out more gas even though it has a higher pumping speed.

Effective pumping speed and pumping time

The effective pumping speed can be calculated with Equation (4.12) [33]. It measures how much air is pumped out of a geometry per unit of time. This depends on the pumping speed of the pump at its inlet and the conductance of the geometry. Figure 4.20 shows the effective pumping speeds for both an empty panel (the core is removed) and the actual panel (with the core present). The indicated upper and lower limits result from the pump's upper and lower limits. However, effective pumping is barely affected by the difference in pumping speeds because the conductance of the core is low. Therefore, the difference between the upper and lower limit of the pumping speeds is negligible.

$$S_{eff} = \frac{CS_p}{C + S_p}, \tag{4.12}$$

$$t = \frac{V}{S_{eff}} \ln \frac{P_1}{P_2}. \tag{4.13}$$

Where:

C = Conductance [m^3/h]
S_{eff} = Effective pumping speed [m^3/h]
S_p = Pump speed [m^3/h]
V = Volume of the panel [m^3]
P_1 = Air pressure at pumping start [Pa]
P_2 = Final air pressure [Pa]

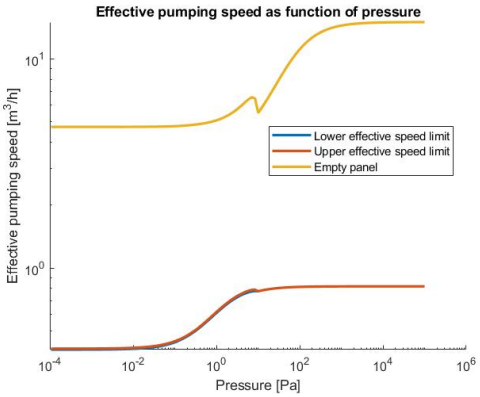

Figure 4.20: Effective pumping speed for the panel geometry and the selected pumps.

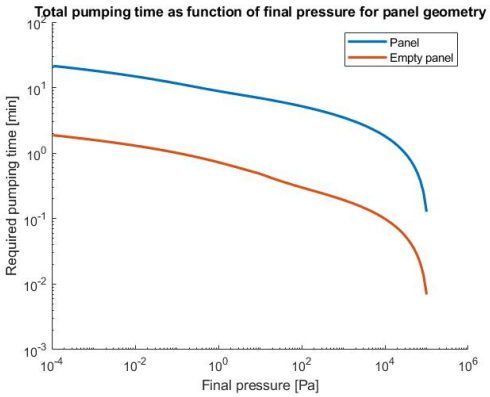

Figure 4.21: Total pumping time required as function of the final internal air pressure in the core.

The time required to evacuate the panel can be calculated with Equation (4.13) [37]. Figure 4.21 shows the required time for a range of final air pressures. An internal air pressure of 10^{-3} Pa is reached after roughly 18 minutes for the current panel geometry and 1.5 minutes for the empty panel. The addition of the honeycomb plates and the intermediate foil increase the pumping time by approximately a factor of 12.

Actual pumping time is expected to be higher than the calculated time since many factors like leak rates, impurities in materials and air, moisture, envelope weld imperfections and probably more have not been considered. This calculation merely serves as an indication of the required pumping times, it is not a perfect representation of reality. Even though the required pumping time is probably underestimated, it is still relatively large. Mass-producing vacuum insulation panels that take eighteen minutes to evacuate will be challenging. Therefore, panel production in a vacuum chamber might be an alternative worth investigating. However, further research into the panel's manufacturability falls outside this report's scope.

4.6 Conclusions

A fully-defined detailed design is presented in this chapter. Geometrical parameters for optimal geometry of the honeycomb plates and the foil are listed in Section 4.4. Stainless steel and basalt fibre are the materials selected for the honeycomb plates and foil respectively. Titanium has lower relative conductivity and weight compared to stainless steel. However, the CO_2 footprint and costs are higher for this material. It might be a feasible alternative for stainless steel in future versions of the vacuum insulation panel. Manufacturing the concept vacuum insulation panel seems plausible. Honeycomb plates for the panel can be manufactured similarly to current honeycomb plate manufacturing and a foil can be adhesively or mechanically bonded to the honeycomb plates. However, further research is required for the manufacturing of cutouts in the honeycomb plates. Besides, the desired bonding method of the foil to the honeycomb plates needs to be selected. Furthermore, feasibly creating a sufficiently high vacuum is challenging. This too requires future research.

Chapter 5 Performance analysis

5.1 Overview

Until now, optimal parameters for the vacuum insulation panel concept have been determined analytically. Multiple simplifications and assumptions have been made to enable the use of the analytical models. However, real thermal and structural performance are probably different from the results generated with the discussed models. Finite element method (FEM) models will be used to simulate more complex situations and thereby generate a more realistic performance estimation of the insulation panel concept. COMSOL Multiphysics is the FEM package used to construct and evaluate FEM models.

In this chapter, structural and thermal performance will be evaluated. First, a more detailed analytical performance overview will be presented. Second, a verification study is performed. Hereby, FEM models that are geometrically identical to the analytical models are simulated and compared to the analytical models. These two models should generate close to identical results. If this is the case, the used boundary conditions, simulation parameters and assumptions are verified. Third, geometrically more complex models that are built similarly to the verified models are used. Their results are deemed reliable since they are verified by simpler models. Mesh convergence of all presented FEM models can be found in Appendix O.

5.2 Structural performance

5.2.1 General approach

The analytical evaluation of structural performance, presented in Chapter 4, shows that creep is the relevant failure mode for both the honeycomb plates and foil for the current panel geometry. Besides creep, buckling, which has been discussed briefly in Chapter 4, can occur in the honeycomb plates. A more detailed literature-based evaluation of the critical buckling load will be presented in the next section. Subsequently, the critical buckling load and stress distribution (relevant for creep) of a FEM model can be compared to literature for a geometrically identical honeycomb. The FEM model can be deemed reliable if its results are comparable to the literature. Which failure mode is dominant will be re-evaluated with the results from this model. Finally, a FEM model representing the concept panel's honeycomb plate can be built and evaluated for the dominant failure mode.

Analogous to the honeycomb plats, analytical performance is compared to the results of a geometrically identical finite element model. The Fem model is verified if the results are similar. Subsequently, a FEM model representing the concept panel's foil can be built and evaluated. The results are deemed reliable since they are verified by simpler models.

5.2.2 Analytical structural performance

Papka et al. [38] used a setup to crush a honeycomb plate in one direction. A calculated force-displacement diagram for this honeycomb plate is shown in Figure 5.1. The dashed lines in this diagram represent different calculated force-displacement curves. Path $o - A - B'$ represents a symmetric linear elastic material model combined with geometrical nonlinearity. Asymmetry is added for $o - A - B$. Paths $o - a - b - c$ and $o - a - b - c'$ represent non-linear behaviour, where $o - a - b - c$ also includes asymmetry. Tested honeycomb plates are expected to follow path $o - a - b - c$ since no linearity or symmetry conditions apply to reality. Figure 5.2 shows the force-displacement diagram for a crushed honeycomb plate specimen. Indeed, it is a rough version of path $o - a - b - c$ in Figure 5.1.

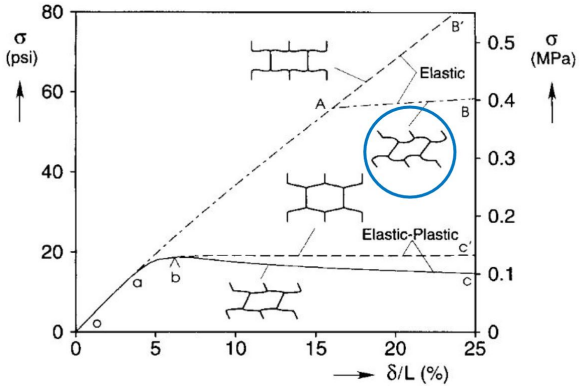

Figure 5.1: Calculated force-displacement response of a crushed honeycomb plate [38].

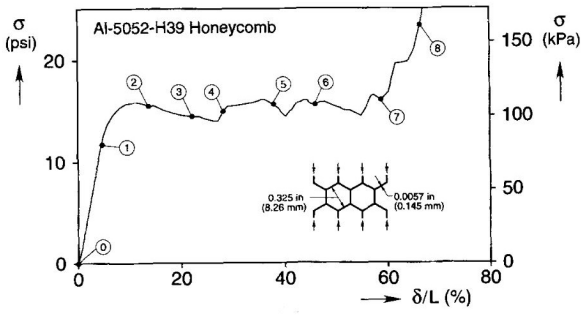

Figure 5.2: Force-displacement response of a crushed honeycomb plate specimen [38].

Honeycomb plates in these tests failed due to the buckling of the honeycomb walls. This happened at an external pressure corresponding to bifurcation point a. This load is the critical buckling load. Klintworth et al. [26] provide equations for buckling mode bifurcation points or surfaces. Appendix I.2 shows the analytical evaluation of the plastic-elastic bifurcation point with equations from Klintworth et al. for material parameters, geometry parameters and operating conditions used in the tests by Papka et al. The evaluated bifurcation point should (and does) match point a in Figure 5.1.

All equations presented by Klintworth et al. can be evaluated for an external transverse load in one direction, as tested by Papka et al., and two directions, as is the case for external air pressure. The plastic-elastic bifurcation point (point a in Figure 5.1) evaluation for the honeycomb plate under bidirectional load equal to the air pressure is shown in Appendix I.

5.2.3 Verification of finite element models for structural performance

Honeycomb wall thickness

The honeycomb plate will be modelled as a thin plate using shell elements in COMSOL Multiphysics. The finite element simulation of the honeycomb plate can be verified if its results are comparable to the results from literature discussed in Section 5.2.2. Figure 5.3 shows the model used for this purpose. The geometry and material of this model are equal to that of the tested honeycomb plate by Papka et al. The diagonal walls of the model are modelled slightly bent instead of perfectly straight. This is done for two reasons. First, modelling a part of an actual plate as a perfect hexagon would be an unrealistic representation since real plates have imperfections. Second, slightly bent walls will bend further in that direction when compressed, whereas perfectly straight honeycomb walls do not have a preferred bending direction. Therefore, perfectly straight walls may not bend at all. Consequently, the simulation will give a more stiff result than would be possible in reality.

One end of the model is pinned (A in Figure 5.3) and a variable displacement in the direction of end A is applied to end B. The external reaction force is evaluated at end B. The slightly bent walls in the model represent the encircled deformation shape (corresponding to path $o-A-B$) in Figure 5.1 since the simulation is expected to follow this path. However, the initial imperfections should result in a more smooth, curved line below the straight $o-A$ and $A-B$ lines.

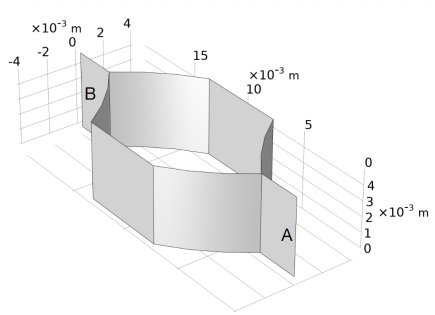

Figure 5.3: Finite element model for literature verification.

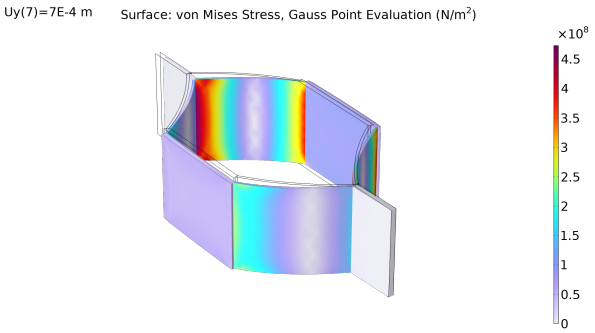

Figure 5.4: Von Mises stress distribution in the literature verification model at an arbitrary prescribed displacement.

The resulting load-strain response of the finite element model, compared to the response from literature, is shown in Figure 5.5. The finite element model behaves as expected. Furthermore, the Von Mises stress distribution in the FEM model is shown in Figure 5.4. Maximum stress is located at the ends of the diagonal walls and stress at the centre of the wall is as good as equal to zero. Both observed phenomena are compliant with the analytical equations presented by Klintworth et al (discussed in Section 4.2.3). Therefore, the FEM model and its results are verified by literature and deemed reliable.

Finally, the failure modes buckling and creep are compared. Stress at the ends of the honeycomb walls (internal) for the same input displacement as the reaction force response (external), plotted in Figure 5.5, is shown in blue in Figure 5.6. This stress is compared to the creep limit (two-thirds of the yield strength, as discussed in Section 2.2.3), shown in red. The two lines intersect at roughly 1% strain. This is well below the strain corresponding to bifurcation point a (shown in Figure 5.5). This means that creep occurs before buckling can occur. Therefore creep is the dominant failure mode of the honeycomb plates of the panel.

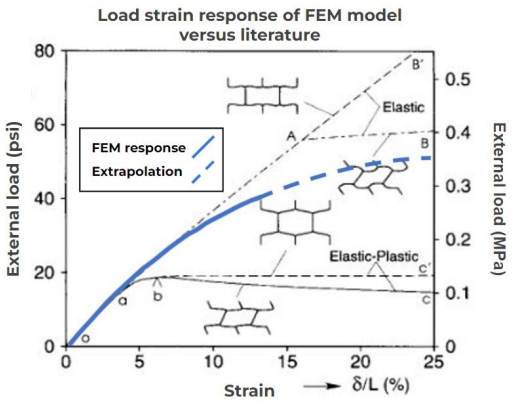

Figure 5.5: Load-strain response for FEM model with geometric and material parameters equal to tested conditions in literature [38], plotted on Figure 5.1.

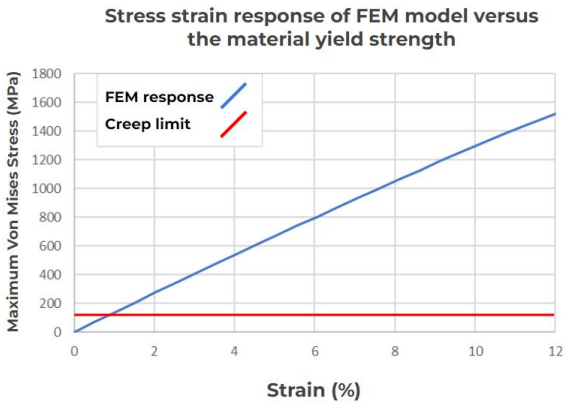

Figure 5.6: Stress-strain response of FEM model plotted with the creep limit (two-thirds the yield strength).

Foil thickness

The simplified model, shown in Figure 3.9 in Section 3.4, is used for calculating the deflection of the foil due to external air pressure. Figure 5.7 shows the FEM model of the foil in the simplified model. The coloured boundaries in this figure indicate different boundary conditions. The blue sides of the foil are pinned supported. A symmetry boundary condition is applied to the sides of the rectangular foil shown in red. The darker grey rectangle in the centre of the foil represents the area where the foil connects to a honeycomb wall from the opposing honeycomb plate. The honeycomb walls are assumed to be infinitely stiff in the FEM models for the foil. Furthermore, the foil is assumed to be uniformly attached to the honeycomb wall. Consequently, this darker grey foil section is modelled as a rigid domain. A load equal to the external air pressure multiplied by the relevant panel area is applied to the rigid domain. The resulting stress distribution is shown in Figure 5.8. The maximum stress indicated in the legend does not converge when the mesh is refined (shown in Figure O.4), which is typical for a numerical stress singularity in the model. This singularity is caused by the sharp edge between the rigid and the plate domains (the dark and light grey domains in Figure 5.7 respectively). However, honeycomb walls are rounded by a small radius in reality, so this stress concentration will not occur. Consequently, the maximum stress is neglected.

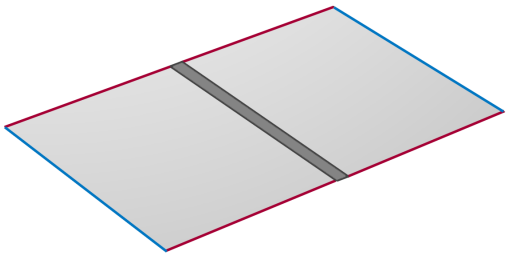

Figure 5.7: Finite element model of simple foil model.

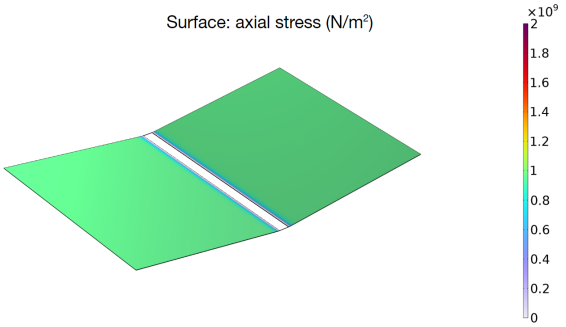

Figure 5.8: Von Mises stress distribution in simple foil model as a result of applied load.

Stress in the green regions in Figure 5.8 equals 962.1 MPa, which is 101% of the analytically calculated stress and roughly two-thirds of the yield strength of the material (Table 4.2). Vertical deflection of the rigid domain equals 2.0 mm, which is 97% of the analytically calculated deflection. The results show that the FEM model is more stiff compared to the analytical model. Analogous to the honeycomb plate model, the foil is modelled as a thin plate. However, the foil is made from woven basalt fibres and is therefore actually a cloth, as mentioned in Section 4.3.4. A cloth's individual fibres can move relative to each other. Consequently, the compressive and bending stiffness of the foil are low. Therefore, the stiffnesses are overestimated by modelling the foil as a thin plate, which is reflected in the FEM results.

5.2.4 Structural performance with finite element models

Honeycomb wall thickness

The FEM model used to evaluate stress in the honeycomb is shown in Figure 5.9. The locations of the honeycomb wall ends and notch tips, introduced in Section 4.2.3, are indicated by the red lines and blue circles respectively. Two pairs of distributed loads, indicated by the red and blue arrows, create a bidirectional compression of the honeycomb. Spring connections with low stiffness are added to the vertical walls to ensure the stability of the model during simulation. Note that this FEM model does not have the previously introduced initially bent walls. Therefore, this model will be used to simulate a perfect honeycomb plate that only exists in theory. Panel deformation will be later introduced to simulate a more realistic honeycomb plate. How the foil affects the structural performance of the honeycomb falls outside the scope of this thesis, as discussed in Section 3.5.

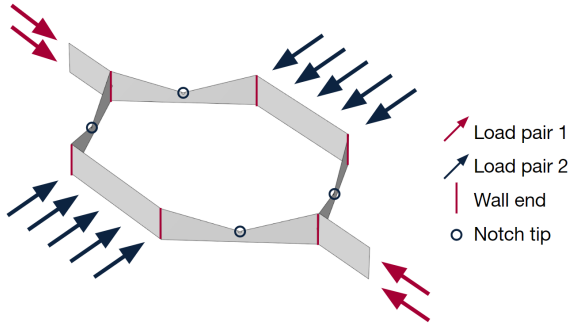

Figure 5.9: Finite element model of a section of the honeycomb plate.

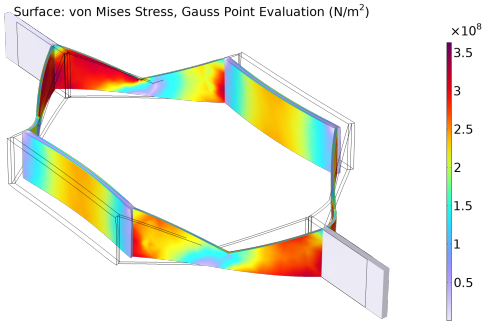

Figure 5.10: Von Mises stress distribution in a section of the honeycomb plate.

The Von Mises stress distribution in the model is shown in Figure 5.10. Visually, stress at the honeycomb wall ends seems to match the stress at notch location in Figure 5.9. However, evaluated stress at the tip of the notch does not converge to a single value. Instead, it goes to infinity for increasing mesh refinement, as is shown in Figure O.7 in Appendix O. This behaviour is typical for a stress singularity in a finite element model. Consequently, stress evaluation at the notch tip does not provide helpful nor reliable results. Therefore, stress close to the notch location is evaluated. This stress will be lower than the actual stress since it is located away from the notch tip. However, this value indicates the stress' order of magnitude in the area near the notch tip. A stress evaluation has been done for a point located 0.05 mm below the notch tip.

The maximum stress at the ends of the honeycomb walls equals 307 MPa, which is 90% of the analytically calculated maximum stress. Stress at the centre of the honeycomb wall equals 274 MPa. Both stresses are of the same order of magnitude. Therefore, the analytically calculated equality of stress at wall ends and notch location, discussed in Section 4.2.3, is deemed plausible. The maximum stress may not exceed a certain threshold to eliminate the failure mode creep. Honeycomb plates are designed for maximum stress of two-thirds of the yield strength of the material. However, up until now, honeycomb plates without imperfections are considered. In reality, no perfect honeycomb plate exists. Therefore, stress will be locally higher. The sensitivity of stress to imperfections in honeycomb geometry is evaluated with a deformed honeycomb model, shown in Figure 5.11. Vertical walls are angled by β_h and diagonal walls are bent by a distance d. Angle β_h and distance d are varied simultaneously from 0 to 10 degrees and 0 to 2 mm respectively. Corresponding stress at wall ends is shown in Figure 5.12. Stress increases significantly for larger values of β_h and d. The thickness of the honeycomb walls can be increased

to reduce the maximum stress in the model. Figure 5.13 shows the maximum stress at the wall ends in the model for ranging honeycomb thickness for β_h and d equal to 10 degrees and 2 mm respectively. The maximum stress is equal to two-thirds of the yield strength (343 MPa) for a honeycomb wall thickness of 0.571 mm, which is a 0.04 mm increase compared to the analytically calculated required honeycomb wall thickness. This thickness will be used further in the thermal performance evaluation.

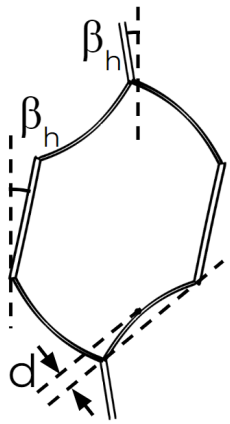

Figure 5.11: The deformed model.

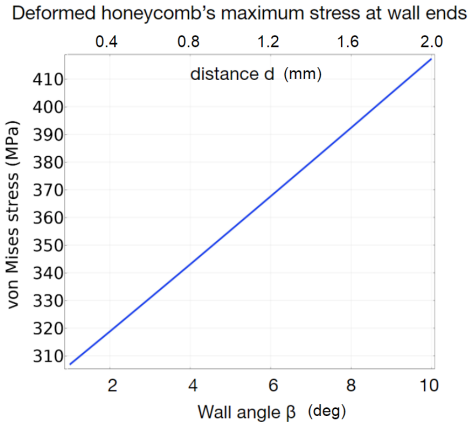

Figure 5.12: Von Mises stress at wall ends for deformed honeycomb geometry.

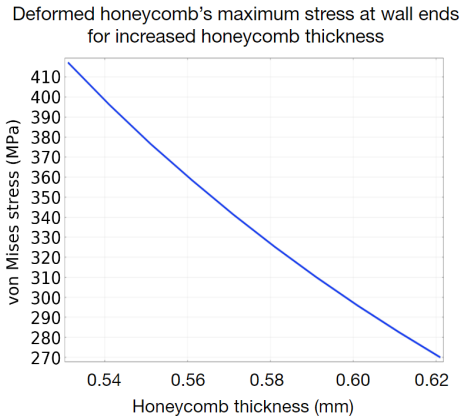

Figure 5.13: Von Mises stress at wall ends for increasing wall thickness of the deformed honeycomb geometry.

Foil thickness

The analytically estimated required foil thickness of 45 µm, discussed in Section 4.2.5, is based on the simplified model. However, in the simplified model, only honeycomb walls in a single row are connected. A new model of a panel section is shown in Figure 5.14. Herein, the rectangle with a black dashed line represents the outline of the simplified model section shown in Figure 5.7. The stress in the simplified model is evaluated at A. Two half simplified models are located to the left and right. A part of the foil between two honeycomb walls from neighbouring simplified models is indicated by B. This part of the foil is neglected in the simplified model, but contributes to the overall stiffness in the complete foil model. The different coloured (red and blue) rectangles in Figure 5.14 represent the honeycomb walls of the two different honeycomb plates. Red areas are fixed and blue areas are modelled as rigid domains where a force equal to the external air pressure multiplied by the corresponding area is pressing down. Symmetry boundary conditions are applied to all remaining free edges of the model.

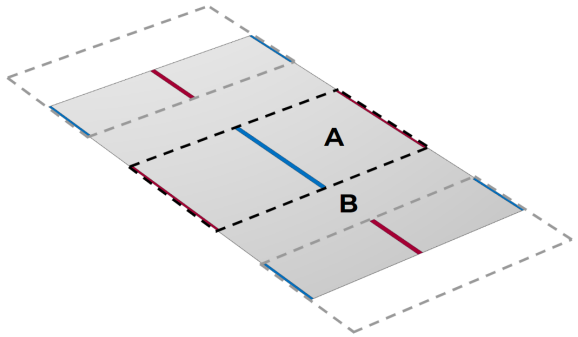

Figure 5.14: FEM model of a foil section. Areas where the foil connects to the honeycomb walls of opposite plates are coloured red and blue.

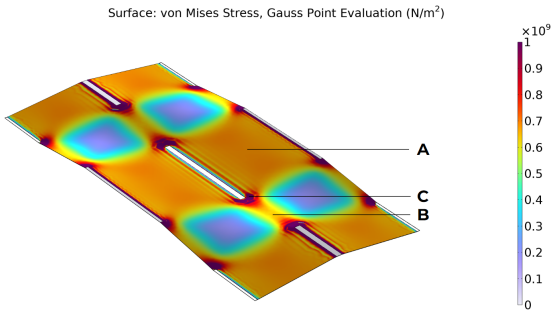

Figure 5.15: Von Mises stress distribution in a section of the foil.

The von Mises stress distribution in the foil is shown in Figure 5.15. Maximum stress occurs at parts indicated by C. However, stress at these parts is overestimated since plates are used for the modelling of the foil (which is actually a cloth). Higher bending stiffness in plates results in higher surface stress, especially for bidirectional bending which occurs in areas similar to the area indicated by C. Furthermore, numerical stress singularities in finite element models contribute to high maximum stress in the model. Actual values for stress at these critical locations could be a topic for further research or could follow from experimental results. High stresses in areas similar to the area indicated by C are ignored for now.

The honeycomb angle influences the length, and thereby stiffness, of the part of the foil indicated by B. The optimal honeycomb angle is where stress at A and B are nearly equal. Figure 5.16 shows stress at A and B for a range of honeycomb angle θ. The lines intersect for an angle between 39 and 40 degrees. Stress at location A is dominant over stress at location B for a rounded-up honeycomb angle of 40 degrees. This is preferred for two reasons. First, the foil thickness is analytically calculated for the simplified model (i.e. the part of the foil indicated with A). These calculations are relevant only if stress in this part of the foil is dominant. Second, the foil has to be thicker for it to handle high stresses at B compared to A since the width of the foil section where stresses are high (i.e. the orange parts in Figure 5.16) is smaller for this section.

The additional stiffness reduces the stress at A by roughly a 28% to 688 MPa. Foil stress at B equals 641 MPa. The negative vertical displacement of the blue areas in Figure 5.14 is equal to 1.79 mm, which is well within the maximum allowed deflection. Therefore, foil thickness can be reduced. Figure 5.17 shows the stress at point A and B in the foil for a range of foil thicknesses. A 39 % foil thickness reduction to roughly 28 µm increases the stress at point A to the analytically calculated stress. However, the actual maximum stress in the foil is expected to be higher. The foil limits the deformation of the honeycomb plate's walls, which increases stress in the foil, as discussed in Section 3.5. Furthermore, slightly higher stress is expected in the foil at locations indicated by C even though the obtained stress concentrations in these regions, shown in Figure 5.15, are expected to be overestimated. Therefore, foil thickness is chosen not to be reduced, and the analytically calculated stress will be used further in this thesis, as an additional safety margin. Future development could show that foil thickness can be reduced to a minimum of 28 µm if all mentioned effects prove to be negligible.

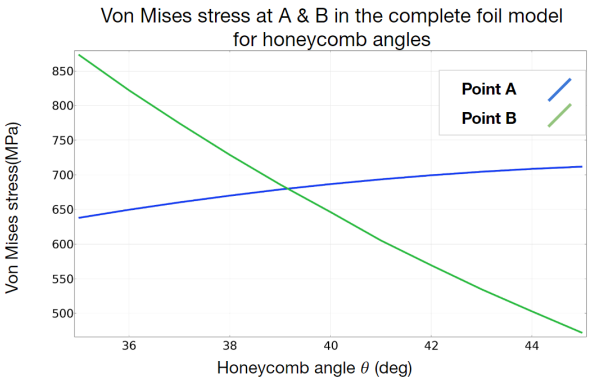

Figure 5.16: Von Mises stress at locations A and B for a range of honeycomb angles.

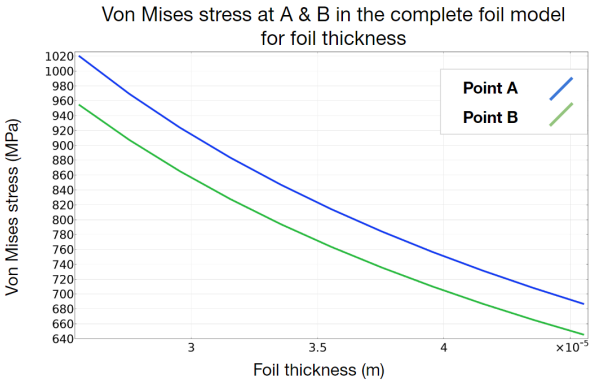

Figure 5.17: Von Mises stress at locations A and B for a range of foil thicknesses.

5.3 Thermal performance

5.3.1 Analytical thermal performance

Thermal resistance per mode of heat transfer can be calculated for the optimal parameters shown in Section 4.4 with equations presented in Section 3.6. The thermal performance of the panel barely changes for internal air pressures below 10^{-3} Pa, as discussed in Section 4.2.8. An overview of the thermal resistance per mode of heat transfer and the thermal resistance to all modes of heat transfer combined at a pressure of 10^{-3} Pa are shown in Table 5.1.

Mode of heat transfer	Thermal resistance at p = 10^{-3} Pa [K/W]
Solid conduction	665.3
Gaseous conduction	797.6
Convection	-
Radiation	9.536
Edge losses	121.4
Total thermal resistance	8.726

Table 5.1: Analytically calculated thermal resistances of all modes of heat transfer at an internal air pressure of 10^{-3} Pa.

5.3.2 Verification of finite element models for thermal resistance

General approach

Two models have been used in the analytical thermal resistance calculations: the simplified model, shown in Figure 3.9 in Section 3.4, and the empty box model, explained in Section 3.6. The simplified model is only used for calculating thermal resistance to solid conduction. Thermal resistances to all other modes of heat transfer are determined with the empty box model. FEM models that correspond to the analytical models are created for each mode of heat transfer.

Even though each FEM model is different, the boundary conditions of all thermal finite element models shown in this and the next subsection are the same. Therefore, the boundary conditions are discussed here and will not be repeated. A temperature of 293.15 K (20°C) is applied to all edges and surfaces located at the bottom of each model and a convective heat flux is applied to all edges and surfaces at panel thickness height (i.e. height equals 1 cm). These top and bottom edges and surfaces will be indicated in the FEM models by blue and red respectively. The external temperature equals 273.15 K (0°C). All other boundaries are thermally insulated. The thermal resistance of the FEM model can be determined with the temperature of the top (blue) edge or surface after simulation. A more elaborate explanation of this method can be found in Appendix P.1.

Solid conduction

A FEM model that is geometrically identical to the analytical simplified model (shown in Figure 3.9 in Section 3.4) is shown in Figure 5.18. The purpose of this model is to compare it to the analytical one. Therefore, the honeycomb wall thickness in this model equals the analytically calculated thickness of 0.53 mm, shown in Section 4.4, not the increased thickness, presented in Section 5.2.4. The FEM model contains only shell elements to reduce the total degrees of freedom. Figure 5.19 shows the temperature distribution over the model. The top of the upper honeycomb wall in the finite element model has a temperature of 273.47 K, which translates to thermal resistance to solid conduction of the total panel of 665.2 K/W, which is almost identical to the analytically calculated resistance, shown in Table 5.1.

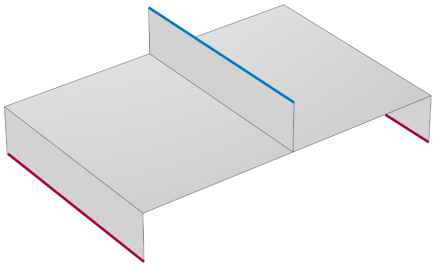

Figure 5.18: Finite element model of the simplified model.

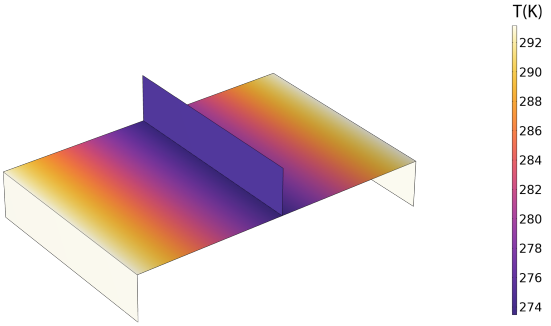

Figure 5.19: Temperature distribution of finite element model of the simplified model as a result of solid conduction.

Gaseous conduction

A finite element model of the empty box model is shown in Figure 5.20. It consists of a single solid domain with thermal conductivity equal to the thermal conductivity of air. Gaseous conduction will be evaluated for an air pressure equal to 10^{-3} Pa. At this pressure, the thermal conductivity of air equals $1.25 \cdot 10^{-5}$ W/mK. Figure 5.21 shows the temperature distribution through the box. The temperature of the cold surface of the empty box is 273.152 K, which translates to a thermal resistance of the model of 799.9 K/W. A result comparable to the analytically calculated 797.6 K/W, shown in Table 5.1. Because the results are similar, finite element modelling is deemed reliable.

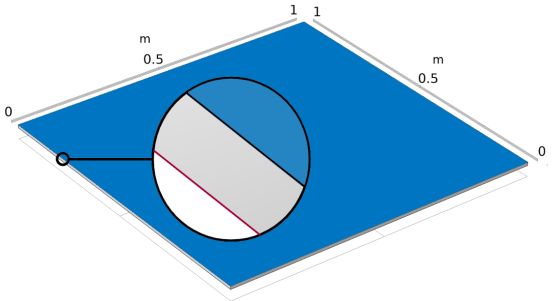

Figure 5.20: Finite element model of the empty box model.

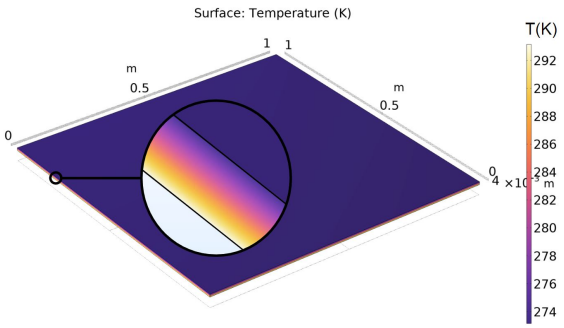

Figure 5.21: Temperature distribution with edge close-up of the finite element model of the empty box model as a result of gaseous conduction.

Radiation

With the empty box model, an analytical thermal resistance to radiative heat transfer of 9.536 K/W (shown in Table 5.1) has been calculated. The model for radiative heat transfer contains two plates spaced by a distance equal to the panel thickness instead of a single solid domain. The FEM model and its temperature distribution are not shown since they look similar to the ones for gaseous conduction, shown in Figures 5.20 and 5.21. The temperature of the cold plate is 273.3562 K for radiative heat transfer. This temperature corresponds to a thermal resistance of the panel of 9.599 K/W, which is close to the analytically calculated value.

Edge losses

Edge losses are caused by solid conduction through the layers of the envelope. The thermal resistance to edge losses is analytically determined by combining the thermal resistance to solid conduction for each envelope layer in Section 3.6. The FEM model used for solid conduction through the envelope is shown in Figure 5.22. This model represents a part of one of the panel's sides by a square plate with sides equal to the panel thickness. A layered material with thermal conductivities and thicknesses of the layers equal to the ones in an MF2 foil, shown in Figure D.1 in Appendix D, is used. The temperature of the top edge equals 288.34 K, which corresponds to a thermal resistance to edge losses of 121.44 K/W for the total panel, which is an exact match with the analytically calculated thermal resistance to edge losses of 121.4 K/W, presented in Table 5.1. Therefore, the analytical value will be used further. Appendix P.2 presents additional steps before equations in Appendix P.1 can be used.

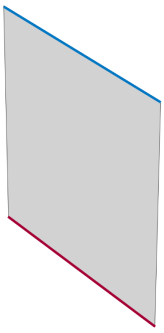

Figure 5.22: Finite element model of the envelope

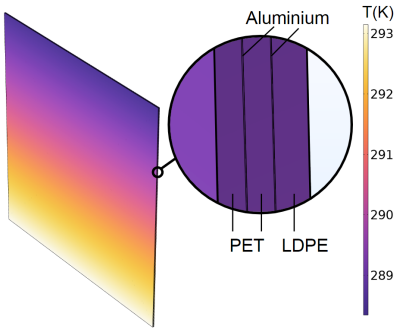

Figure 5.23: Temperature distribution with edge close-up of the envelope's finite element model.

Conclusion

Finite element models for solid conduction, gaseous conduction, radiation and edge losses show results comparable to the analytically calculated values. Therefore, The FEM models are verified. Consequently, the results of more complex finite element models that will be presented next can be deemed reliable.

5.3.3 Thermal resistance with finite element models

Solid conduction

In the simplified model, each honeycomb wall connects to just two other honeycomb walls: one to the left and one to the right. Connections with all other walls are neglected to enable analytical conduction resistance calculations. However, neglected connections between walls do exist. A schematic representation of neglected heat flow is shown in Figure 5.24. Herein, two vertically placed simplified models are shown. The green arrows represent the considered and the red arrows represent the neglected flow direction in the simplified model. All arrows that connect the two simplified models are red. A new FEM model where all honeycomb walls are connected via the foil is used to calculate the thermal resistance to solid conduction of the panel more accurately. The model, shown in Figure 5.25, contains a simplified model, equal to the one shown in Figure 5.18, in the centre and two half simplified models on either side (analogous to Figure 5.14). The honeycomb wall thickness in the finite element models from hereon equals 0.571 mm, as discussed in Section 5.2.4. The foil connects the models so that the influence of neighbouring rows can be observed. The diagonal walls of the honeycomb plates also connect the models in reality, but they are not present in the FEM model. Heat transfer through the diagonal walls is negligibly small since they are not in contact with the foil and no temperature difference between honeycomb walls in a single plate is present. Furthermore, not modelling the diagonal walls results in less required computation time.

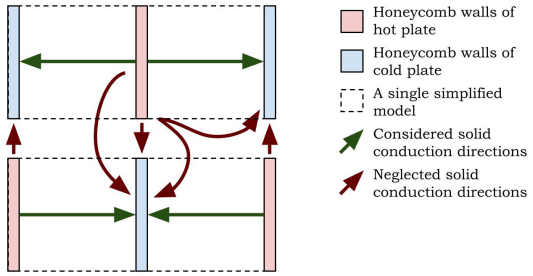

Figure 5.24: Schematic representation of solid conduction directions on a top view of two vertically spaced simplified models.

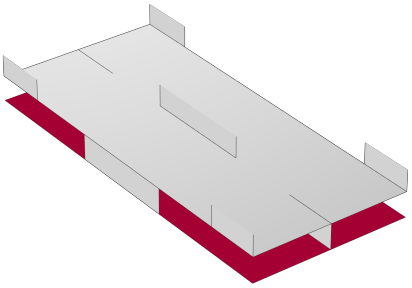

Figure 5.25: Finite element model of a section of the panel without the diagonal walls. The top envelope is removed to show the foil.

Two additional plates on the top and bottom of the model simulate the panel's envelope. These plates' thickness equals the MF2 envelope's thickness of 65 µm [39]. Because the envelope is so thin, its contribution to the total thermal resistance of the panel is negligibly small (0.2 mK/W for this panel). The envelope's thermal resistance to solid conduction does influence the transverse conduction of heat through it. However, only the top envelope's temperature, not its temperature distribution, is relevant for this report. Therefore, a high thermal conductivity of 10^6 $Wm^{-1}K^{-1}$ is used for the envelopes. The top envelope is not shown in Figure 5.18 (and future figures) so the intermediate foil can be observed. The model shown in Figure 5.25 is also symmetric. Two symmetry planes intersecting the model at half the width and the length are constructed. Figure 5.26 shows the part of the symmetry model that can be mirrored across the two symmetry planes. This model is smaller and therefore requires fewer elements for accurate FEM modelling. The model shown in Figure 5.26 will be referred to as the symmetry model from hereon.

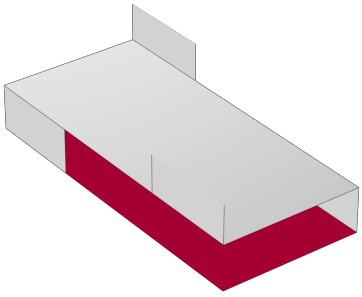

Figure 5.26: Finite element model of the symmetry model. The top envelope is removed to show the intermediate foil.

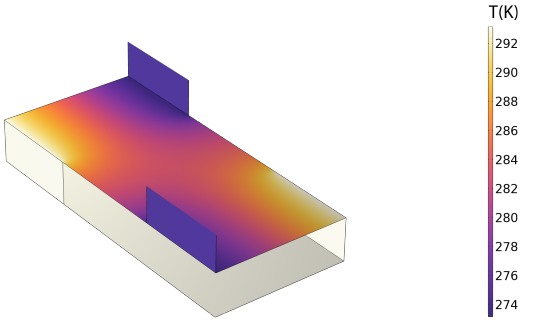

Figure 5.27: Temperature distribution of the finite element model of the symmetry model as a result of solid conduction.

Symmetry boundary conditions have been applied to all sides of the model to generate a panel section. All other boundary conditions are equal to the conditions for the previous model, explained in Figure 5.18. Temperature distribution in the foil for this new model is shown in Figure 5.27. From this figure, it can indeed be observed that the temperature distribution in the foil is not a one, but a two-dimensional problem. The average temperature of the top envelope equals 273.16 K. This temperature translates to a thermal resistance of 230.0 K/W for the total panel, which is only 35% of the analytically calculated thermal resistance. This decrease in thermal resistance is caused by the additional heat transfer between honeycomb walls from neighbouring simplified models. The increase in honeycomb wall thickness barely affects the temperature of the top envelope (order of 10^{-5} K).

The thermal resistance to solid conduction increases to 400 K/W if the foil thickness is decreased to the minimum foil thickness of 2.8 µm, presented in Section 5.2.4. This increased thermal resistance to solid conduction will barely influence the total thermal resistance of the current panel since radiation is the dominant mode of heat transfer. Therefore, this hypothetical thermal resistance to solid conduction will not be used further in this thesis. However, it can prove to be useful for future high-performance versions.

Gaseous conduction

The empty box model and one-dimensional conduction have been assumed for gaseous conduction. However, the panel structure and three-dimensional conduction must be considered for a more realistic model of gaseous conduction in the actual panel. The model that incorporates these demands builds on the existing symmetry model, shown in Figure 5.26. The new model, shown in Figure 5.28, combines the model used for solid conduction with two added domains of air where gaseous conduction occurs. The domains' conductivity equals $1.25 \cdot 10^{-5}$ W/mK, as discussed in Section 5.3.2.

The results of a FEM simulation with a model that combines solid conduction and gaseous conduction should be similar to a combination of results for the individual modes. The total thermal resistance is estimated by calculating the sum of the inverses of both thermal resistances if the two modes are assumed to act parallel to each other. The previously found thermal resistances for solid conduction and gaseous conduction were 230.0 K/W and 799.9 K/W respectively. Subsequently, thermal resistance of a combination of the two modes is estimated to be 178.6 K/W. However, the two modes do influence each other. The total thermal resistance of the combined model is therefore expected to be lower, but not significantly lower, than 178.6 K/W.

The temperature distribution in this model is shown in Figure 5.29. From visual inspection alone, the impact of the added gaseous conduction on the overall heat transfer can be observed. The cold surface has a temperature of 273.16 K. This corresponds to a thermal resistance to a combination of solid and gaseous conduction of 156.8 K/W. This is an 12% reduction of the estimated thermal resistance, which is in line with the previously discussed expectations.

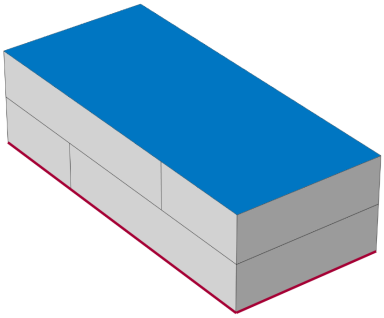

Figure 5.28: Finite element model the symmetry model with added air domains for gaseous conduction.

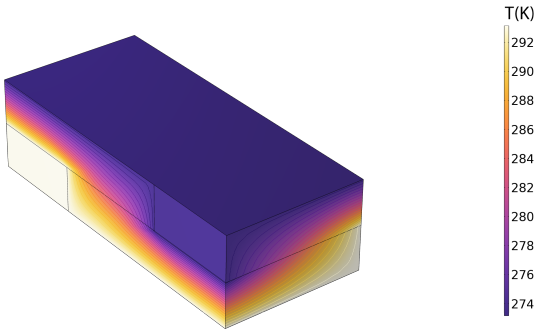

Figure 5.29: Temperature distribution of the finite element model of the symmetry model with added air domains as a result of solid and gaseous conduction.

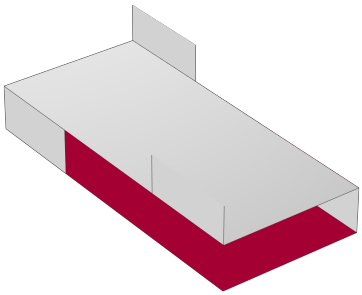

Figure 5.30: Finite element model of the symmetry model for solid conduction and radiation. The top envelope is removed to show the intermediate foil.

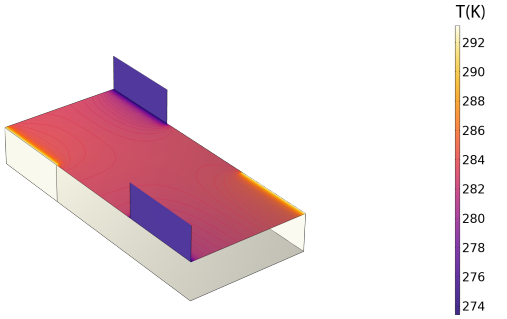

Figure 5.31: Temperature distribution of the finite element model of the symmetry model as a result of solid conduction and radiation.

Radiation

The strategy for a complete evaluation of the thermal resistance to radiative heat transfer is similar to the approach presented for gaseous conduction. An estimation of the result based on a parallel combination of the separate modes will be presented first, followed by an evaluation of the complete model. Thermal resistances of solid conduction and radiation were 230.0 K/W and 9.599 K/W respectively. Combining solid conduction and radiation in parallel results in an estimated thermal resistance of 9.214 K/W. The temperature in the FEM model is expected to be lower, but not significantly lower than this value.

The finite element model, shown in Figure 5.30, has been used to simulate radiative heat transfer combined with solid conduction. It is geometrically identical to the model used to calculate conduction only (shown in Figure 5.26). Radiation occurs between all boundaries that radiate heat inward. Figure 5.31 shows the temperature distribution of the model. The top envelope has been removed so that the temperature distribution in the foil can be observed. The previously found temperature distribution in Figure 5.27 can no longer be observed in Figure 5.31. This can be explained by the fact that radiation dominates. Therefore, foil temperature is determined by radiative heat transfer to the foil. The temperature at the cold side of this model is 273.4 K, which corresponds to a thermal resistance of 7.9 K/W. However, this thermal resistance is expected to overestimate the actual thermal resistance to radiative heat transfer due to modelling errors. An elaborate explanation of these modelling errors can be found in Appendix O.

Thermal performance of the complete panel

The total thermal resistance to all modes of heat transfer can be calculated analytically with Equation (3.9), repeated below. This equation requires heat transfer modes to act parallel to each other. However, finite element models for both gaseous conduction and radiation show that modes of heat transfer interact with each other. Nevertheless, a hypothetical thermal resistance to isolated gaseous conduction and radiation is calculated.

The thermal resistance to solid conduction alone and combined with gaseous conduction and radiation are 230, 156.8 and 7.9 K/W, respectively. These values are substituted in Equation (3.9). All other thermal resistances in this equation are infinite since the corresponding modes of heat transfer do not occur in the models. Subsequently, Equation (3.9) can be solved (for both gaseous conduction and radiation) to find the hypothetical isolated values for $R_{cond,gas}$ and R_{rad} of 493.2 and 8.18 K/W respectively.

The total thermal resistance to all modes of heat transfer is also calculated with Equation (3.9). Thermal resistances to isolated solid conduction, gaseous conduction, radiation and edge losses equal 230.0, 493.2, 8.18 and 121.4 (presented in Table 5.1) K/W respectively. This gives a total thermal resistance of 7.31 K/W. The total thermal resistance of the finite element model is expected to be lower, but close, due to the influence modes of heat transfer have on each other.

$$\frac{1}{R_{tot}} = \frac{1}{R_{cond.solid}} + \frac{1}{R_{cond.gas}} + \frac{1}{R_{rad}} + \frac{1}{R_{edge}} \tag{3.9}$$

All modes of heat transfer except for edge losses are active in the FEM model of the complete panel. Edge losses have not been considered since the model represents a section of the panel's centre. The finite element of the complete model and the temperature distribution in the gaseous domains (and therefore the whole model) look identical to the ones shown in Figures 5.28 and 5.29, and are therefore not shown. The temperature distribution in the foil looks identical to the one shown in Figure 5.31. The temperature of the top surface of the model equals 273.45 K, corresponding to a total thermal resistance of 6.57 K/W for the panel's centre. The thermal resistance of the total panel equals 6.23 K/W after taking edge losses into account. This thermal resistance is calculated analogously to Equation (3.9). Therefore, the panel's centre and edge losses are assumed to act completely in parallel. The total thermal resistance is expected to be slightly lower due to interactions between modes of heat transfer in the panel's centre and solid conduction through the envelope.

The total thermal resistance of the finite element model that incorporates all heat transfer modes is lower than, but close to, the estimated 7.31 K/W. The panel's thermal resistance equals its R-value since a one-square-metre panel is considered. Actual thermal resistance to all modes of heat transfer is expected to be lower since thermal resistance to radiation is expected to be overestimated due to modelling errors (explained further Appendix O) and interaction between heat transfer through the edges and centre of the panel are neglected in this thesis.

5.4 Other performance parameters

5.4.1 General approach

From all performance parameters mentioned in Section 2.2.4, environmental impact and economic performance are not yet discussed. 2.7 kg of stainless steel and 0.11 kg of foil are necessary for the concept panel. The amount of material and the material parameters of the parts determine the concept panel's environmental impact and economic performance. Energy use and the cost of manufacturing and transport have not been considered. Furthermore, no service lifetime assessment has been made. These factors can differ significantly from conventional vacuum insulation panels due to the higher required vacuum. A complete life cycle analysis, life cycle cost analysis and environmental impact study need to be performed before the economic performance and environmental impact can be determined accurately, which falls outside the scope of this thesis. Nevertheless, first estimates are presented here. Although many environmental impact factors exist, only the Global Warming Potential (GWP) will be considered in this section.

5.4.2 Environmental impact

Stainless steel has a GWP of 3.16-3.74 kg/kg and the GWP for basalt fibre ranges from 0.0543 to 0.0600 kg/kg. This corresponds with a GWP of 9.2 ± 0.8 kg and 6.5 ± 0.32 grams $CO_2 - eq$ for the honeycomb plates and the foil respectively. The contribution to the total GWP of the foil is negligible, as was predicted in Section 4.3.4.

5.4.3 Economic performance

Stainless steel has a price of 19.1-25 EUR/m^3 and the price of basalt fibre ranges from 5.06-6.44 EUR/m^3. Raw material costs are 7.58 $\pm$ 1.01 euros and 0.26 $\pm$ 0.03 euros for the honeycomb plates and foil respectively. Total material costs are 7.84 $\pm$ 1.04 euros for the panel's core. This calculation has not considered envelope costs, manufacturing costs, transportation costs and manufacturing losses.

5.5 Comparison between concept and conventional VIPs.

5.5.1 Thermal performance

The R-value of a 1 cm thick concept vacuum insulation panel is estimated to be 6.23 m^2K/W. However, the real value is expected to be lower. Nonetheless, the concept's thermal performance is still higher than conventional vacuum insulation panels, which have an R-value of 2.5 m^2K/W for equal panel thickness.

5.5.2 Environmental impact

The properties of conventional VIPs are presented in Appendix J. For 1 kg of conventional VIP, the GWP ranges from 6.2 to 11.1 kg $CO_2 - eq$. Furthermore, conventional VIPs have a density ranging from 162 to 192 kg/m^3. GWP of a conventional VIP the size of the concept VIP (100cm $\times$ 100cm $\times$ 1cm) equals 15.3 $\pm$ 5.5 kg. Both materials selected for the concept panel have a lower GWP than the conventional VIP, as shown in Table 4.2 in Section 4.3.6. The concept panel with dimensions of 100cm $\times$ 100cm $\times$ 1cm has a GWP of 9.2 $\pm$ 0.8 kg.

The concept VIP seems to have a lower environmental impact than conventional VIPs. However, this calculation has not considered the energy required for manufacturing these panels. Besides, energy saved during the lifetime of a concept panel can not be determined since panel lifetime has not been considered. Further research into the environmental impact of the panel is required. Other environmental impact factors should be included in this research.

5.5.3 Economic performance

Prices of 41.41 and 62.49 euros for 20 and 30 mm thick one square-metre conventional VIPs respectively can be found in literature, as discussed in Appendix J. A price of 21.08 euros for a 10 mm thick panel can be found with linear extrapolation. The material costs of the core of the insulation panel concept are 7.84 $\pm$ 1.04 euros, as presented in Section 5.4.3. Note that the raw material costs of the concept panel are compared to the purchase price of the conventional VIP, which makes the concept panel look better than it might actually be. Moreover, many costs of the concept panel are ignored. A more detailed overview and analysis of these costs is required. Besides the purchase price, future research should include the economic benefits of energy savings. A more expensive concept panel can still be feasible if the savings outweigh the initial cost.

5.6 Conclusions

Finite element simulations show stress in the honeycomb plate that is comparable to the analytically calculated value. Analysis of a honeycomb plate with slight imperfections shows that its wall thickness should be increased by 0.04 mm. The evaluated foil stress is lower than the analytically calculated stress for simpler models. However, actual foil stress is expected to be higher since the foil limits the deformation of the honeycomb plate's walls, which increases the stress in the foil, and stress concentrations are expected to be present in the foil. Therefore, foil thickness is not reduced for the concept panel presented in this thesis. Future research or experiments can show whether foil thickness can be reduced for future versions of the panel. The absolute minimum required foil thickness is evaluated to be 28 µm.

The thermal performance of the panel is evaluated with FEM models as well. First, simpler models for each mode of heat transfer separately are created and compared to analytical calculations. All models show comparable results and are therefore deemed reliable. More complex models based on these simpler models could therefore be used confidently. Eventually, the thermal resistance of a model that incorporates all modes of heat transfer was evaluated to be 6.23 K/W. Since a one-square-meter panel is simulated, thermal resistance equals the R-value of the panel. However, the thermal performance of an actual panel is expected to be lower since thermal resistance to radiation is expected to be overestimated and resistance-lowering interactions between heat transfer through the edges and centre of the panel are neglected.

Other performance parameters are evaluated for the concept vacuum insulation panel. Furthermore, these values are compared to conventional vacuum insulation panels. The evaluated thermal performance of the concept panel is more than two times better than that of a conventional insulation panel. Environmental impact and economic performance seem promising. A GWP of the panel of 9.2 $\pm$ 0.8 kg and a material cost of 7.84 $\pm$ 1.04 euros are evaluated for the panel core. However, many aspects have not been considered for both performance parameters. Therefore, future research is required to evaluate these performance parameters better. Nevertheless, these results show that the concept has promising potential.

Chapter 6 Conclusions and future work

6.1 General approach

This report aims to answer the questions in Section 1.2. The sub-questions from this section are repeated, accompanied by their answer in Section 6.2. Together they form the basis for main research question's answer, shown after the sub-questions in Section 6.3. An overview of topics that require future research is discussed in Section 6.4.

6.2 Sub-questions

1. What are the relevant aspects that play a role in insulation panels?

Arguably the most critical aspect of insulation techniques is the thermal performance. The total thermal performance is commonly expressed as the R-value, which can be found by combining the thermal resistances of each heat transfer mode. The heat transfer modes are solid conduction, gaseous conduction, convection and radiation. Structural performance, especially creep failure, should not be neglected when dealing with high stresses. Other performance parameters need to be considered in a feasibility assessment of the product's economic and environmental performance.

2. What are the relevant parameters and aspects for the specific vacuum insulation panel concept?

Two honeycomb plates and an intermediate foil make up the panel's core. A combination of relevant parameters determines the geometry of the parts. These parameters should be chosen such that heat transfer through the panel is minimised whilst failure of the panel does not occur. Relevant failure modes are creep and buckling. The parameters are analytically determined with the help of models that simplify reality.

3. What is the optimal geometry for the concept panel?

Thin panel parts result in high thermal performance. However, structural requirements pose limits on the relevant parameters. The parameters for an optimal geometry where high thermal resistance is achieved, whilst creep and buckling do not occur, are listed in Section 4.4.

4. What is the optimal material for each panel part?

Environmental impact and cost are paramount for the honeycomb plates, whilst low thermal conductivity is critical for the foil. A low density is only essential for the honeycomb plates if the panels will be used in the transport industry. Combining stainless steel honeycombs and basalt fibre foil is optimal for the vacuum insulation panel concept. However, titanium might be a feasible alternative for future high-performance versions of the concept panel.

5. Is the optimal panel manufacturable?

Honeycomb plates are already being produced right now. Cutouts need to be made in the plates. Multiple methods have been proposed. Constructing prototypes with these methods will show which method is preferred. Panels can be evacuated after construction or manufactured in a vacuum chamber. The pumping time of a panel is estimated to be 18 minutes. Future research, experiments and prototyping are required for further development of the panel.

6. What is the performance of the optimised concept panel?

An R-value of 6.23 m^2K/W is estimated based on finite element simulations. However, the actual R-value of the panel is expected to be lower since thermal resistance to radiative heat transfer is expected to be overestimated. The GWP of the panel core is 9.2 ± 0.8 kg and its raw material costs are 7.84 ± 1.04 euros.

7. How does the performance of the concept and conventional vacuum insulation panels compare?

Performance parameters of the concept panel have been compared to conventional vacuum insulation panels for a panel size of 100cm × 100cm × 1cm. The R-values of the concept and a conventional vacuum insulation panel of this size are 6.23 and 2.5 m^2K/W, respectively. The global warming potential of the concept is 9.2 ± 0.8 kg compared to 15.3 ± 5.5 kg for conventional VIPs. A conventional VIP's price of 21.08 euros is compared to the material costs of the concept panel of 7.84 ± 1.04 euros.

6.3 Main research question

The main research question of this report is:

To what extent is an optimised concept vacuum insulation panel a potentially feasible alternative for conventional vacuum insulation panels?

The insulation panel concept introduces an alternative design for the core of VIPs. This core consists of two honeycomb plates and an intermediate foil. Relevant parameters determine the geometry of the core's parts. Heat transfer through the panel is minimised whilst the relevant failure modes creep and buckling do not occur. Furthermore, Stainless steel and basalt fibre are the best materials for the honeycomb plates and the foil respectively. The concept panel's performance parameters have been compared to conventional vacuum insulation panels for a panel size of 100cm × 100cm × 1cm. The thermal performance of the concept panel is higher with an R-value of 6.23, compared to 2.5 m^2K/W for a conventional vacuum insulation panel. The global warming potential of the concept is 9.2 ± 0.8 kg compared to 15.3 ± 5.5 kg for conventional VIPs. A conventional VIP's price of 21.08 euros is compared to the material costs of the concept panel of 7.84 ± 1.04 euros. All performance parameters of the concept panel seem promising. However, thermal performance is expected to be lower and the environmental impact and panel price higher. Further research is required into performance-influencing aspects and the panel's manufacturability. Nevertheless, this thesis shows that the vacuum insulation panel concept has promising potential.

6.4 Future work

6.4.1 General approach

This thesis has been done during the conceptual phase of the development of the panel. Therefore, many subjects require further research or development to evaluate the panel's performance. The relevant subjects are the panel's manufacturing, performance, and further development. Each category will be discussed separately in the coming subsections.

6.4.2 Manufacturing

Manufacturing of the honeycomb plates

Different methods for the honeycomb walls cutouts' manufacturing have been presented in Section 4.5. However, how these methods affect structural, economic and environmental performance requires further research. The preferable method can be determined based on the findings from its findings. Furthermore, prototypes and tests can be used to substantiate the results.

Panel evacuation

A vacuum can be created by pumping air out or by manufacturing a panel in a vacuum chamber. Further research into both methods is necessary before one can be selected. The pumping time required for the necessary vacuum is roughly estimated to be equal to 18 minutes, as shown in Section 4.5.4. Eighteen minutes for a single panel is quite long. Besides, many factors that negatively influence pumping time, like leak rates, impurities in materials and air, moisture, envelope weld imperfections and probably more, have not been considered. An overview of all relevant parameters should be made. Required pumping time should be re-evaluated with all these parameters included. Vacuum chamber manufacturing is an alternative method. The vacuum chamber is kept at a constant pressure by continuous evacuation. Further research on whether vacuum chamber manufacturing suits the concept vacuum insulation panel is required.

6.4.3 Performance

Structural performance

The structural performance is only evaluated for separate parts. Evaluating a combination of the foil and honeycomb plates still needs to be done. The foil between the two honeycomb plates influences the structural rigidity of the honeycomb plates. Furthermore, only a section at the centre of the panel has been evaluated. The structural performance of the panel's edges still needs to be evaluated. Local panel reinforcements might be necessary if the edges are critical. Besides, the honeycomb plates could be changed to different plate types. Square lattice panels are a promising alternative since the walls of these plates would only be axially loaded.

Thermal performance

An R-value of 6.23 m^2K/W for a 1 cm thick insulation panel is exceptionally high compared to conventional VIPs (mentioned in Appendix J). However, the actual R-value is expected to be lower since many aspects of this concept panel still need to be considered. The actual R-value can be obtained as a result of the further research presented in this subsection.

Service lifetime

Appendix D shows an evaluation of the ageing mechanics of conventional VIPs. Water and air diffusion through the envelope contribute to a performance decrease over a period of 25 years. The effect of ageing mechanics on the concept panel's performance still needs to be considered. How ageing affects the concept panel is expected to differ from conventional VIPs since a higher vacuum is present in the concept panel's core. A different envelope might be required to maintain this high vacuum. MF2 foil is used for current VIPs. This foil is assumed to be good enough for the concept panel. However, future research should be done to validate this assumption.

Costs and energy use

Costs and energy use during panel manufacturing (and transportation) have been neglected in the performance estimation shown in Section 5.4. However, these two factors are probably relatively high compared to conventional insulation material manufacturing. Future research might show that expensive and energy-intensive manufacturing of these panels does not outweigh the advantage of higher thermal performance. Furthermore, other environmental impact factors, presented in Appendix J, should be considered in a future environmental impact study (besides the GWP, the only factor considered in this thesis). Future research should include the effect of ageing in a life cycle cost analysis (LCCA) and the environmental impact study.

Acoustic properties

Acoustic properties are relevant for insulation materials since these materials should not only limit the transport of heat, but also sound for real-life applications. Acoustic properties have not been considered in this thesis, but are definitely relevant for the further development and realisation of the vacuum insulation panel concept.

Panel size

Implementation or transportation standards might influence the further development and realisation of the panel. A square panel with sides of one metre has been assumed for this report. However, a different panel shape and size might have a different optimal geometry and performance. Future research into requirements for insulation material implementation should be done.

6.4.4 General further development

All results presented in this report are theoretical estimates. No prototype has been built. No tests have been performed to evaluate claims made in this report. Prototyping and testing are critical steps in the further development and realisation of the vacuum insulation panel concept.

Appendix A List of symbols

Variable	Meaning
α	Thermal diffusivity
α_f	Foil deflection angle
β	Notch angle geometry parameter
β_h	Honeycomb imperfection angle
ϵ	Surface emittance of material
θ	Honeycomb angle
$\lambda_{g,0}$	Gaseous conductivity at time $t = 0$
$\lambda_{wv,0}$	Conductivity due to water vapour at time $t = 0$
μ	Dynamic viscosity
ν	Kinematic viscosity
ρ	Density of a medium
σ	Stefan-Boltzmann constant
σ_y	Yield strength of a material
τ_g, τ_w, τ_{wv}	Time constants
ϕ	Relative humidity
ϕ_e	External relative humidity of air
A	Area of a medium or surface
a, b	Rectengular tube parameters
C	Conductance
c_{get}	Maximum capacity of the getter
c_{des}	Maximum capacity of the desiccant
c_p	Specific heat capacity
c_v	Constant volume specific heat
F	Load on a side of the unit cube
F_{12}	Shape factor of hot and cold surface
f	Form factor
g	Gravitational acceleration constant
h	Heat transfer coefficient
h_{cutout}	Honeycomb cutout height
k	Thermal conductivity
k_{air}	Conductivity of air
k_0	Conductivity of air at room temperature
l	Length of a medium
l_h	Honeycomb wall length
M	Molar mass
m_{get}	Mass of getter
m_{des}	Mass of desiccant
p	Air pressure
p_g	Gas pressure
p_{wv}	Water vapour partial pressure
$\dot{Q}$	Heat transfer
q	Heat flux
R	Gas constant
R_{mode}	Thermal resistance to specific mode

Continued on next page...

...Continued from previous page

Variable	Meaning
R_{val}	R-value
R_{surf}	Surface resistance of emitting surface
R_{space}	Space resistance
S	Pumping speed
SF_g	Geometric safety factor
t_f	Foil thickness
t_h	Honeycomb wall thickness
t_p	Panel thickness
T	Temperature
T_m	Mean temperature
u	Water content in the core
V	Volume of a medium
GTR	Gas transfer rate
$WVTR$	Water vapour transfer rate
w	Width a medium
w_p	Panel width

Table A.1: Variables and constants.

Appendix B Convective heat transfer coefficient calculations

Calculating the convective heat flux consists of multiple steps. First the kinematic viscosity and the thermal diffusivity of the gas or fluid are calculated with Equations (B.1) and (B.2) [16] respectively. Note that the conductivity depends on air pressure and temperature as shown in Equation (2.5) in Section 2.2.2. Next the Grashof (Equation (B.3) [16]), Prandtl (Equation (B.4) [16]), Rayleigh (Equation (B.5) [16]) and average Nusselt numbers need to be calculated. To calculate the average nusselt number, three Nusselt numbers for vertical wall convection can be calculated (Equation (B.6) [40]). The average Nusselt number is equal to the largest of the three Nusselt numbers (Equation (B.7) [40]). Finally, the heat transfer coefficient can be calculated as shown in Equation (B.8) [16].

$$\nu = \frac{\mu}{\rho}, \tag{B.1}$$

$$\alpha = \frac{k}{\rho C_p}. \tag{B.2}$$

Where:

ν = Kinematic viscosity [m^2/s]
μ = Dynamic viscosity [kg/m s]
ρ = Density [kg/m^3]
α = Thermal diffusivity [m^2/s]
k = Thermal conductivity [$Wm^{-1}K^{-1}$]
C_p = Specific heat capacity [$Jm^{-3}K^{-1}$]

$$Gr_L = \frac{\Delta(T) g L^3}{T_m \nu^2}, \tag{B.3}$$

$$Pr = \frac{\nu}{\alpha}, \tag{B.4}$$

$$Ra_L = Gr_L Pr. \tag{B.5}$$

Where:

ΔT = Temperature difference between two opposing plates [K]
g = Gravitational acceleration constant (=9.81) [m/s^2]
L = To be traveled length between the plates [m]

$$\begin{aligned} Nu_1 &= 0.0605 Ra_L^{1/3} \\ Nu_2 &= \left[1 + \left(\frac{0.104 Ra_L^{0.293}}{1 + (6310/Ra_L)^{1.36}} \right)^3 \right]^{1/3} \\ Nu_3 &= 0.242 \frac{Ra_L}{W/L}^{0.272} \end{aligned} \tag{B.6}$$

Where:

W = Width of the plate

$$\overline{Nu}_L = max(Nu_1, Nu_2, Nu_3), \tag{B.7}$$

$$h = \frac{k}{L} \overline{Nu}_L. \tag{B.8}$$

Appendix C Concept panel renders

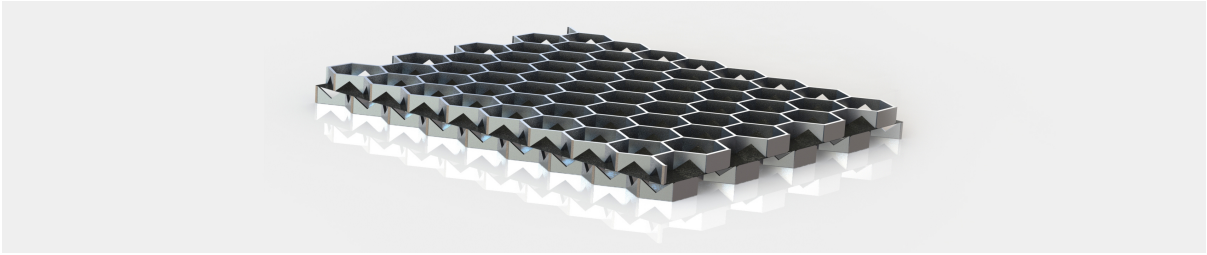

Figure C.1: The core of the panel.

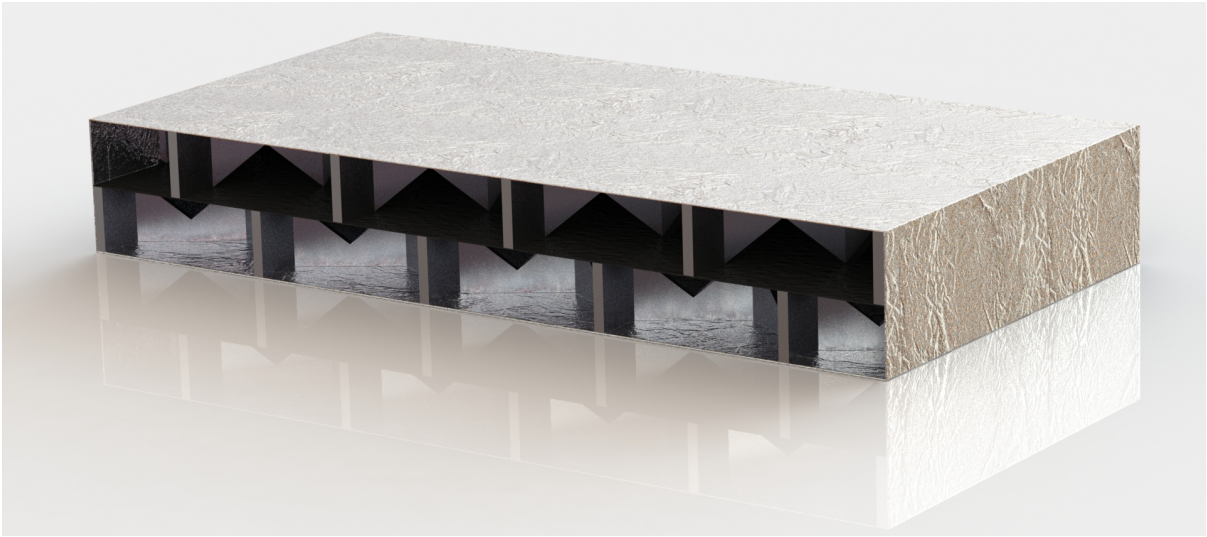

Figure C.2: Cross section of the total panel.

Figure C.3: Side of the panel's core

Appendix D Literature survey chapter 3.3.3: Properties of the envelope

The main purpose of the envelope is to create an airtight layer around the core material. Even with a fully sealed layer, air and water vapour can slowly diffuse through the barrier into the core. A thick aluminium barrier is ideal to counter this permeation [12]. However, using a fully metal envelope results in undesired, effortless conduction. This allows heat to travel through the foil around the VIP which can significantly reduce the effectiveness of the entire panel [12, 34].

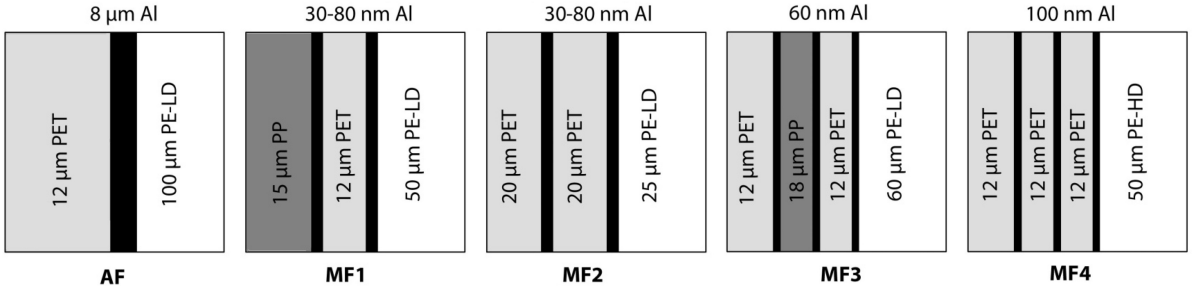

Figure D.1: Different types of envelope materials [39].

Actual envelopes comprise of a multi-layer structure that can be composed in many different forms, as shown in Figure D.1. The aluminium foil (AF) is the simplest and consist of a relatively thick layer of aluminium with an added outer PET protection layer. The metallised film (MF) foils use multiple layers of aluminium and various polymers.

Figures D.2 and D.3 show a comparison of the five foil types. It is clear that the aluminium foil is the best air and water vapour blocking envelope. The starting conditions in both graphs are assumed to be zero pressure and zero mass percent water at time equals zero. Also no changing laminate properties, getters or desiccants have been taken into account.

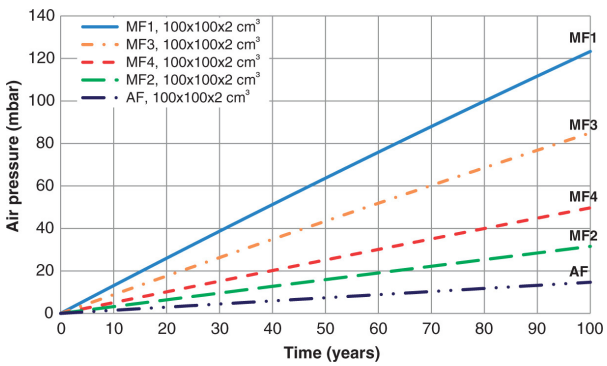

Figure D.2: Air pressure for various laminate types [39].

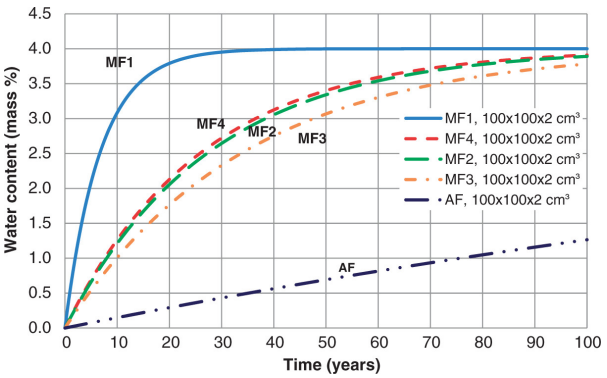

Figure D.3: Water content for various laminate types [39].

The thermal conduction through the envelope creates thermal bridges at the edges that lower thermal resistance of the panel as a whole. The performance at the edges is further reduced due to the presence of air or water in not fully sealed voids. All performance reducing effects at the edges combined are called edge losses. The thermal transmittance through aluminium foil and metallised film as function of the panel thickness is depicted in Figure D.4. Edge conduction becomes negligible for large panel thickness because the path length and therefore the thermal resistance of the envelope increases significantly. Edge conduction goes to zero for small panel

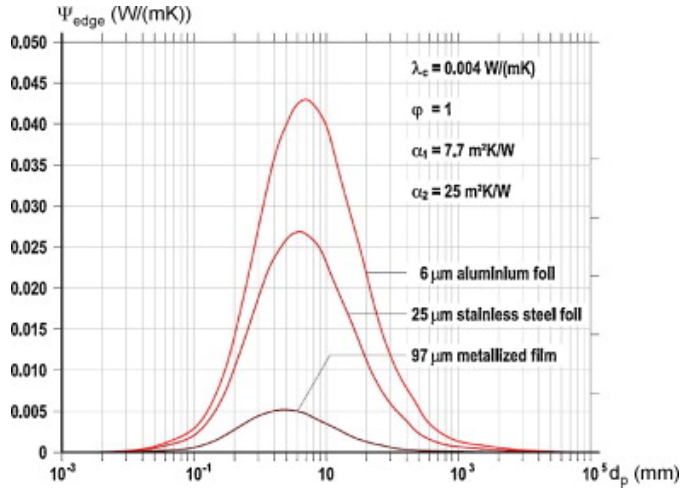

Figure D.4: Behaviour of the linear thermal transmittance as function of the panel thickness d_p for different VIP envelopes and for a centre-of-panel thermal conductivity of 0.004 W/(m K) [12].

thickness as well because thermal conduction of the total panel is dominated by the conduction through the core material for small panel thickness.

The AF and MF2 both have acceptable resistance to the permeation of air. The AF does have a better resistance to diffusion of water vapour, but the benefits do not outweigh the negative effects of edge losses due to the higher thermal conductivity. This makes the MF2 the most favorable foil composition for the use of VIPs [12, 13].

Appendix E Geometry of the unit cube

The unit cube (and its geometry) has been introduced in Section 3.4. A graphical representation of the panel's unit cube is repeated below as Figure E.2. The height of the unit cube is equal to the the panel height, which is one of the relevant parameters presented in Section 3.3. Multiplying this height by the width or length of unit cube results in the areas of the two sides. The width and length make up the top area.

The location of the top surface is shown in Figure E.3. Horizontal edges of the top surface intersect the diagonal walls of the hexagons at half the wall length. The distance between these edges is equal to the width shown in Figure E.2. The vertical sides of the top surface are located at half the thickness of the vertical honeycomb walls. The distance between these edges is the length shown in Figure E.2. The length and width of the top surface depend on the geometry of a hexagon. All hexagon sides are equal to l_h, as discussed in Section 3.3. Honeycomb angle θ determines the angle of the diagonal walls of the honeycomb. Both honeycomb wall length l_h and honeycomb angle θ are shown in Figure E.4.

Length L of the top surface can be calculated with Equation (E.1). Note that l_h defines the inner sides the hexagon. Therefore, honeycomb thickness t_h does not does not affect the length of the hexagon sides, but does affect length L.

Before the method for calculating the width of the top surface is introduced, it is important to explain what the horizontal boundaries of the top surface represent. The structure inside the unit cube will be repeated both horizontally and vertically. There are multiple widths W for which the structure inside the box can be repeated in a manner results in a pattern of hexagons. Repetition of one or multiple rows results in a perfect pattern. Because width W represents a distance for which the system can be repeated, vertical distances between two equal points in a hexagon pattern automatically fulfill the conditions for W. Herein two equal points are identically located on the hexagon and vertical to each other. An example of two points that meet this condition are the two red points shown in Figure E.1. The distance between these two points is not the smallest possible width, shown in Figure E.3. However, the width required to repeat two rows (as shown in Figure E.1) is twice the width required for repeating a single row.

Calculating the width for a single row is done by calculating the width for two rows and dividing it by two. However, the thickness of the honeycomb plate walls creates a spacing between the hexagons. The location of this spacing is indicated with by the blue circle in Figure E.1. There are two of those gaps between the two red points. One is encircled, the other is located right beneath the upper red dot (it is not encircled so that the upper red point is more visible). Figure E.5 shows a close-up of the encircled part in Figure E.1. Three dotted lines are added. The blue line divides the upper space between hexagons of thickness t in two equal parts of half the thickness. The green line is an extension of the top left diagonal line. The red line connects the bottom points of the vertical hexagon sides. Distance v in Figure E.5 is the vertical distance that needs to be calculated.

Vertical distance v can be determined with the help of the two triangles shown in Figure E.6. The blue triangle consists of a line perpendicular to the diagonal hexagon lines with a length equal to the thickness of the honeycomb walls, a vertical line of length a and a line parallel to the diagonal hexagon sides. The shape of this blue triangle will not change if it is moved along the diagonal hexagon line. The red triangle is constructed with the dotted lines from Figure E.5. it

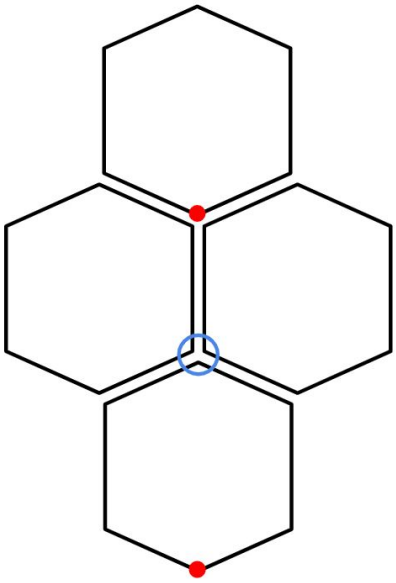

Figure E.1: Example of two vertically spaced equal red points. A gap between the hexagons is indicated with a blue circle.

consists of a horizontal line of length t/2, a vertical line of length b and a diagonal line parallel to the diagonal line from the hexagon. Both triangles have an angle equal to honeycomb angle θ. Vertical distance v is equal to a - b, which is shown in Equation (E.2)

The total distance between the two red dots in Figure E.1 and thereby W can now be calculated with Equation (E.3). The areas of the surfaces A_{top} (equal to $L*W$), $A_{side,1}$ (equal to $L*t_p$) and $A_{side,2}$ (equal to $W*t_p$) can be calculated withEquation (E.4), Equation (E.5) and Equation (E.6) respectively.

$$L = 2\cos(\theta)l_h + t_h \tag{E.1}$$

$$v = \frac{t_h}{\cos\theta} - \frac{1}{2}t_h \tan\theta \tag{E.2}$$

$$W = \frac{(1+\sin\theta)2l_h\cos\theta + (2-\sin\theta)t_h}{2\cos\theta} \tag{E.3}$$

$$A_{top} = \frac{4l_h^2\cos^2\theta + 4l_h^2\cos^2\theta\sin\theta + 6t_h l_h\cos\theta + (2-\sin\theta)t_h^2}{2\cos\theta} \tag{E.4}$$

$$A_{side,1} = (2l_h\cos\theta + t_h)\,t_p \tag{E.5}$$

$$A_{side,2} = \frac{((1+\sin\theta)2l_h\cos\theta + (2-\sin\theta)t_h)t_p}{2\cos\theta} \tag{E.6}$$

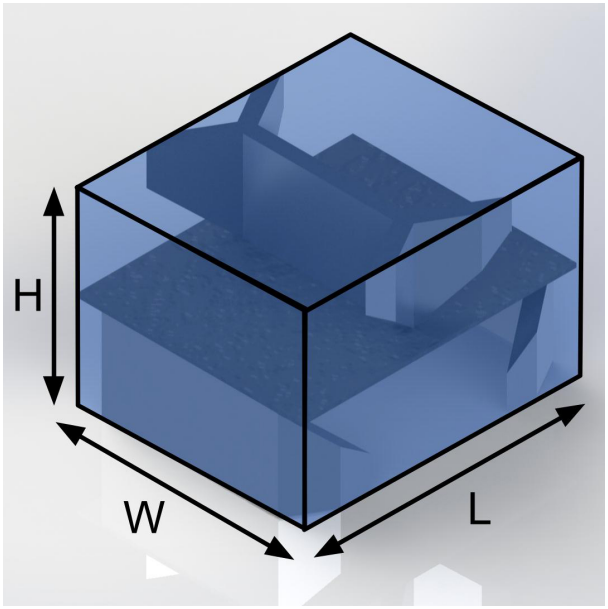

Figure E.2: Model of panel unit cube.

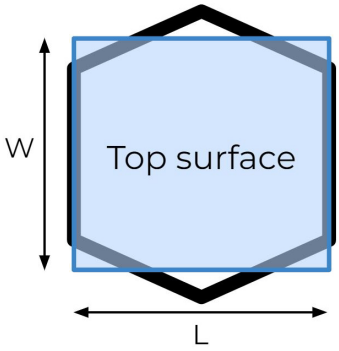

Figure E.3: Location of the top rectangle on top of a single hexagon.

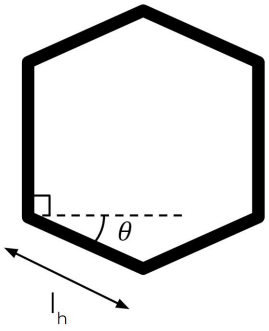

Figure E.4: A single hexagon with indicated angle and hexagon side length.

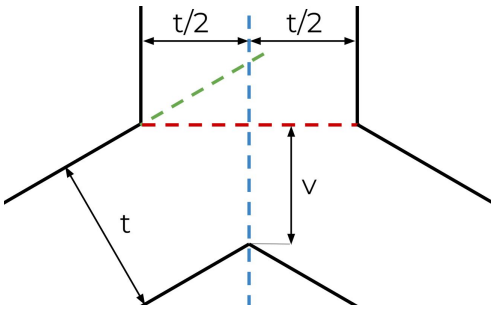

Figure E.5: Close-up of the gap between hexagons with three additional lines, indicate thicknesses and indicates vertical distance v.

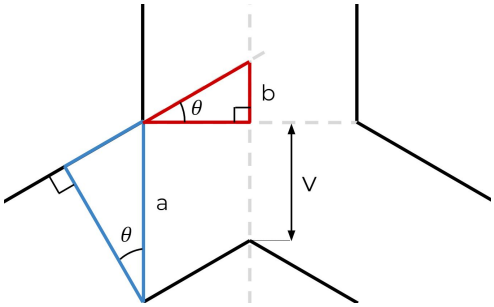

Figure E.6: Triangles for calculating the vertical distance v.

Appendix F Stress concentration factor k_{cutout}

Axially loaded rectangular specimens with a V-shaped cutout can be parameterised as shown in Figure F.1 [27]. Figure F.2 shows values for k_{cutout} that correspond to geometry parameters 2β and l/w, which are shown in Figure F.1. A graphical representation of these data points can be found in Figure F.3. A fourth-order surface, defined by Equation (F.1), can be fitted through these data points. The fourth order surface is shown in Figure F.4.

Both parameters that define the value of the stress concentration factor (2β and l/w) depend on the geometry of the notch. The notch spans the entire diagonal walls of the honeycomb plate. Equivalently, the notch will have a width of $2h$, as shown in Figure 4.2. Subsequently, the stress concentration factor is no longer independent of the honeycomb wall length since the wall length influences 2β, which can be calculated with Equation (F.2). The stress concentration factor can now be fully defined by two geometry parameters: l_h and l/w (for a fixed panel thickness), where l/w represents the fraction of the honeycomb wall that is cut away. Figure F.5 shows the stress concentration factor based on panel geometry parameters. Up until now, the minimum thickness of the honeycomb wall was a function of panel geometry and stress concentration factor. It can now be expressed as a function of solely panel parameters since stress concentration factor k_{cutout} has also become a function of panel geometry. Figure F.6 shows the required minimum thickness as a function of panel geometry parameters graphically.

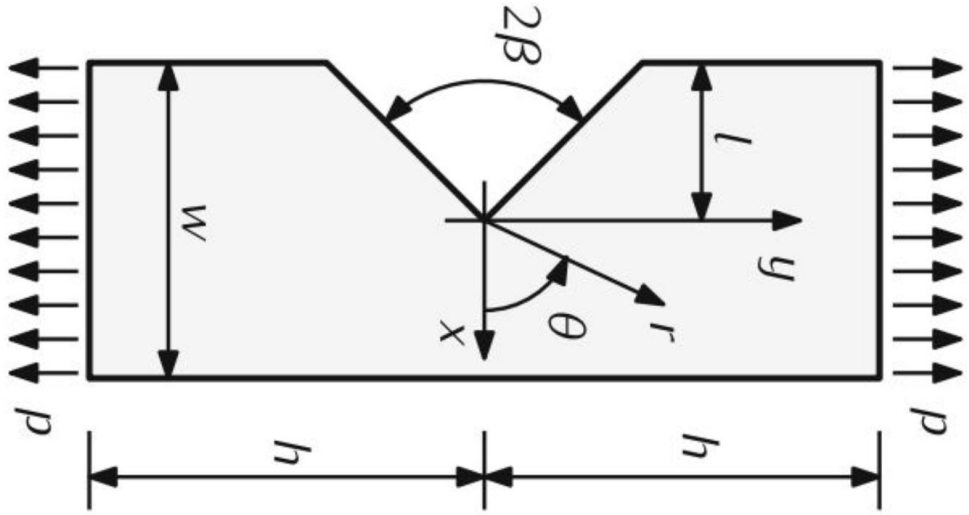

Figure F.1: Geometry of an axially loaded specimen with symmetrical V-shaped notch [27].

2β	l/w					
	0.2	0.3	0.4	0.5	0.6	0.7
0	1.085	1.614	2.369	3.539	5.537	9.422
$\pi/6$	1.097	1.630	2.389	3.569	5.579	9.491
$\pi/3$	1.169	1.724	2.520	3.756	5.859	9.979
$\pi/2$	1.366	1.978	2.888	4.297	6.736	11.515
$2\pi/3$	1.804	2.593	3.766	5.630	8.934	15.551

Figure F.2: Stress concentration factor k_{cutout} at tip of V-shaped notch [41].

$$S(x,y) = 4.748 - 4.386x - 45.03y + 3.329x^2 + 26.73xy + 191.4y^2 - 1.104x^3 - 12.23x^2y - 49.81xy^2 - 323.5y^3 + 0.1576x^4 + 1.98x^3y + 10.92x^2y^2 + 29.16xY^3 + 222.2y^4 \quad \text{(F.1)}$$

$$2\beta = 2\arctan\frac{l_h}{l/wt_p} \quad \text{(F.2)}$$

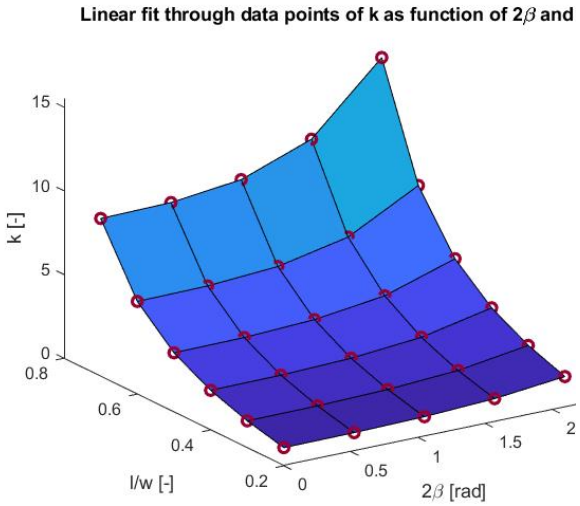

Figure F.3: Linear surface fit plotted through data points from Figure F.2.

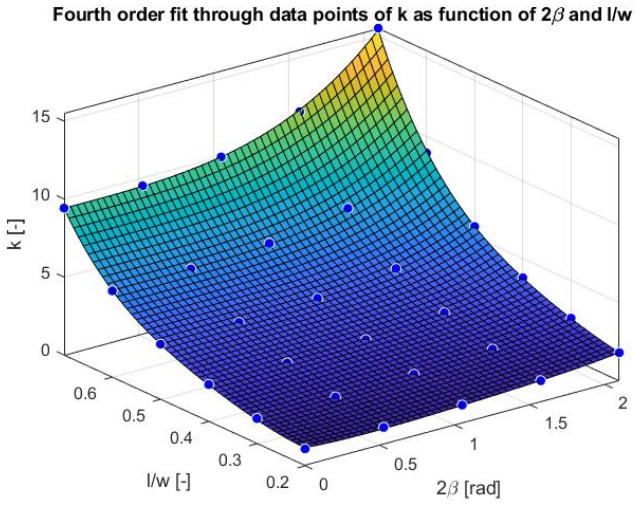

Figure F.4: Fourth order surface fit plotted through data points from Figure F.2.

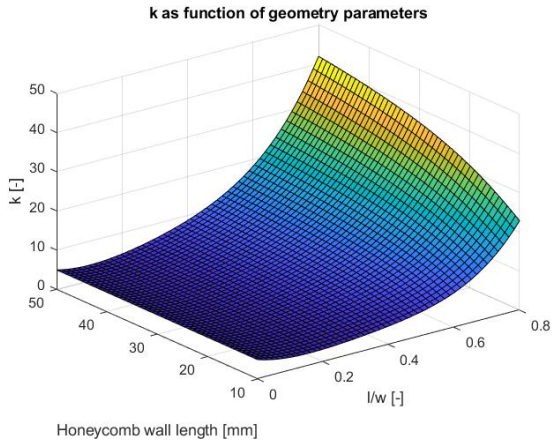

Figure F.5: Stress concentration factor based on panel geometry.

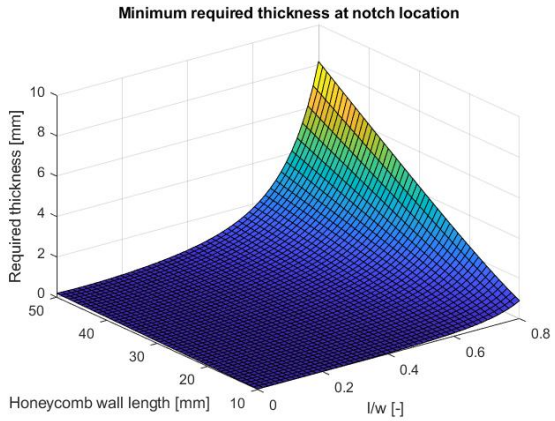

Figure F.6: Minimum required honeycomb wall thickness based on panel geometry.

Appendix G Equation derivations

G.1 α_f

Figure 4.9 is repeated in Figure G.1. ΔL_{foil}, dz and α_f all change when the foil deflects due to the externally applied load. α_f follows from geometry, as shown in Equation (G.1). ΔL_{foil} can be written as function of the strain ϵ and the initial length of the foil L_{foil}, shown in Equation (G.2). Substituting Equation (G.2) in Equation (G.1) results in Equation (G.3). L_{foil} can be divided out of Equation (G.3) and the strain ϵ can be replaced by σ/E using Hooke's law, resulting in Equation (G.4). The stress and elasticity modulus are two thirds the yield strength of the foil material ($2/3\sigma_{y,f}$) and the elasticity modulus of the foil material E_f. Substituting both values and slightly rewriting Equation (G.4) results in Equation (4.9), repeated below.

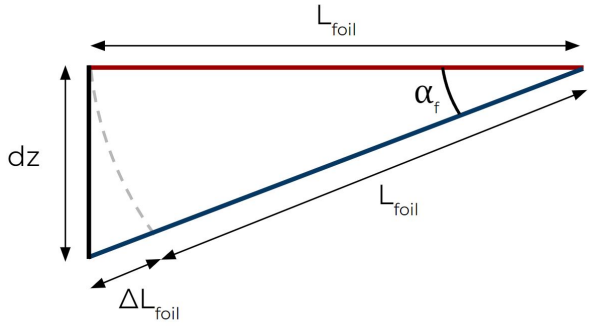

Figure G.1: Displacement of a deflecting foil.

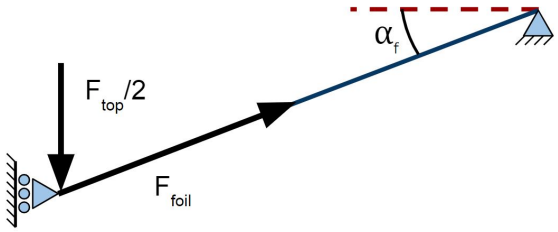

Figure G.2: Free body diagram of the deflected foil.

$$\alpha_f = \cos^{-1} \frac{L_{foil}}{\Delta L_{foil} + L_{foil}} \tag{G.1}$$

$$\Delta L_{foil} = \epsilon L_{foil} \tag{G.2}$$

$$\alpha_f = \cos^{-1} \frac{L_{foil}}{\epsilon L_{foil} + L_{foil}} \tag{G.3}$$

$$\alpha_f = \cos^{-1} \frac{1}{\sigma + 1} \tag{G.4}$$

$$\alpha_f = \cos^{-1} \frac{3E_f}{2\sigma_{y,f} + E_f}, \tag{4.9}$$

G.2 t_f

A free body diagram of the deflected foil is shown in Figure G.2. All foil dimensions are similar to the ones shown in Figure G.1. Both Figures G.1 and G.2 show only half of the simplified model. Therefore, the external force acting on the simplified model is divided by two. Furthermore, a roller is applied to the point where the foil connects to the other half of the foil. It is hereby assumed that both sides of the foil are geometrically identical and exert equal foil force F_{foil}.

The foil elongates due to the externally applied force at the top F_{top}. This elongation results in a strain and therefore a stress in the foil. The foil's stress is equal to two-thirds the yield strength of the material since the foil is designed for creep (explained in Chapter 2). F_{foil} can be determined by the stress and the geometry of the foil. The cross-sectional area of the foil is assumed to be a rectangle with height equal to the foil thickness t_f and width equal to the honeycomb wall length l_h. Subsequently, F_{foil} can be calculated with Equation (G.5). Furthermore, the magnitude of the vertical component of F_{foil} is equal to F_{top} since the system shown in Figure G.2 is in equilibrium. Therefore, F_{foil} can also be expressed as a function of F_{top}, as shown in Equation (G.6). Substituting Equation (G.5) in Equation (G.6) and rewriting for t_f results in Equation (4.11), repeated below.

$$F_{foil} = 2/3\sigma_{y,f} t_f l_h \tag{G.5}$$

$$F_{foil} = \frac{F_{top}}{2\sin\alpha_f} \tag{G.6}$$

$$t_f = \frac{3F_{top}}{4\sin(\alpha_f)\sigma_{y,f} l_h}. \tag{4.11}$$

G.3 L_{foil}

Figure G.3 shows the geometry of a single honeycomb. A honeycomb wall from the opposite plate (shown in blue) is added in the centre of the single honeycomb. The foil as it is used in the simplified model is shown in red. The length of the foil L_{foil}, as used in Equation (4.10) and Figure G.1, is the distance between neighbouring honeycomb walls, as indicated in Figure G.3. L_{foil} can be calculated with Equation (G.7).

$$L_{foil} = \cos\theta L_h - t_h \tag{G.7}$$

G.4 $t_{h,ends}$

Equations (4.4) and (4.6) show equations for the axial and bending load on diagonal wall AB respectively and are repeated below. Stress caused by both loads can be calculated with Equations (G.8) and (G.9). Maximum fibre distance y in Equation (G.9) equals $t_h/2$ and second moment of inertia I in the same equation equals $h_h t_h/12$. Maximum stress occurs at the ends of the walls ends [26]. This maximum stress is a combination of σ_{Pab} and σ_{Mab} and can be calculated with Equation (G.10). Rewriting this equation for t_h (with the ABC-Formula) results in Equation (G.11). However, the maximum allowed stress is known, since this equation will be used to evaluate maximum thickness required to eliminate creep failure. Substituting $2/3\sigma_{y,h}$ for $\sigma_{max,ab}$ results in Equation (4.7), repeated below.

$$P_{AB} = -\sigma_x h(L + L\sin\theta)\cos\theta - \sigma_y hL\cos\theta\sin\theta - \tau_{xy}h(L + L\sin\theta) \tag{4.4}$$

$$M_{AB} = [\sigma_x hL(L + L\sin\theta)\sin\theta - \sigma_y h(L\cos\theta)^2 - \tau_{xy}hL^2\cos\theta]/2 \tag{4.6}$$

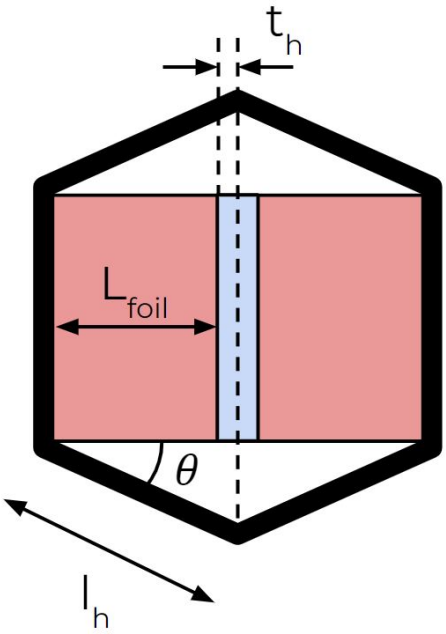

Figure G.3: Geometry of a single honeycomb, a honeycomb wall from the opposite plate (blue) and the simplified model's foil (red).

$$\sigma_{Pab} = \frac{P_{AB}}{h_h t_h} \tag{G.8}$$

$$\sigma_{Mab} = \frac{M_{AB} y}{I} \tag{G.9}$$

$$\sigma_{max,ab} = \frac{P_{AB} t_h + 6 M_{AB}}{h_h t_h^2} \tag{G.10}$$

$$t_{h,ends} \geq \frac{P_{AB} + \sqrt{P_{AB}^2 + 24 \sigma_{max,ab} h M_{AB}}}{2 \sigma_{max,ab} h} \tag{G.11}$$

$$t_{h,ends} \geq \frac{3 \left(P_{AB} + \sqrt{P_{AB}^2 + 16 \sigma_{y,h} h M_{AB}} \right)}{4 \sigma_{y,h} h} \tag{4.7}$$

Appendix H R-value of conventional VIPs

Thermal conductivity of isolated vacuum insulation panels ranges from 4 $\mathrm{mWm^{-1}K^{-1}}$ at the start of the panel lifetime to 8 $\mathrm{mWm^{-1}K^{-1}}$ at the end, as mentioned in Appendix J. Aging effects have not been considered for the concept vacuum insulation panel. Therefore, only a comparison between new panels is relevant. Consequently, a thermal conductivity of 4 $\mathrm{mWm^{-1}K^{-1}}$ will be used for conventional VIPs.

The thermal resistance of the panel can be calculated with Equation (3.3), repeated below. Herein, length of the object L equals the thickness of the VIP. Analogous to Figure 4.10 for the concept panel, the R-value of conventional VIPs can be expressed as a function of panel thickness and honeycomb wall length as well, as shown in Figure H.1. No honeycomb wall are present in conventional VIPs, so the honeycomb wall length will not influence the R-value of VIPs. Dividing all data points in Figure 4.10 by the corresponding values in Figure H.1 results in Figure 4.11. Note that the orientation of this graph differs from Figure 4.10.

$$R_{cond} = \frac{L}{kA} \tag{3.3}$$

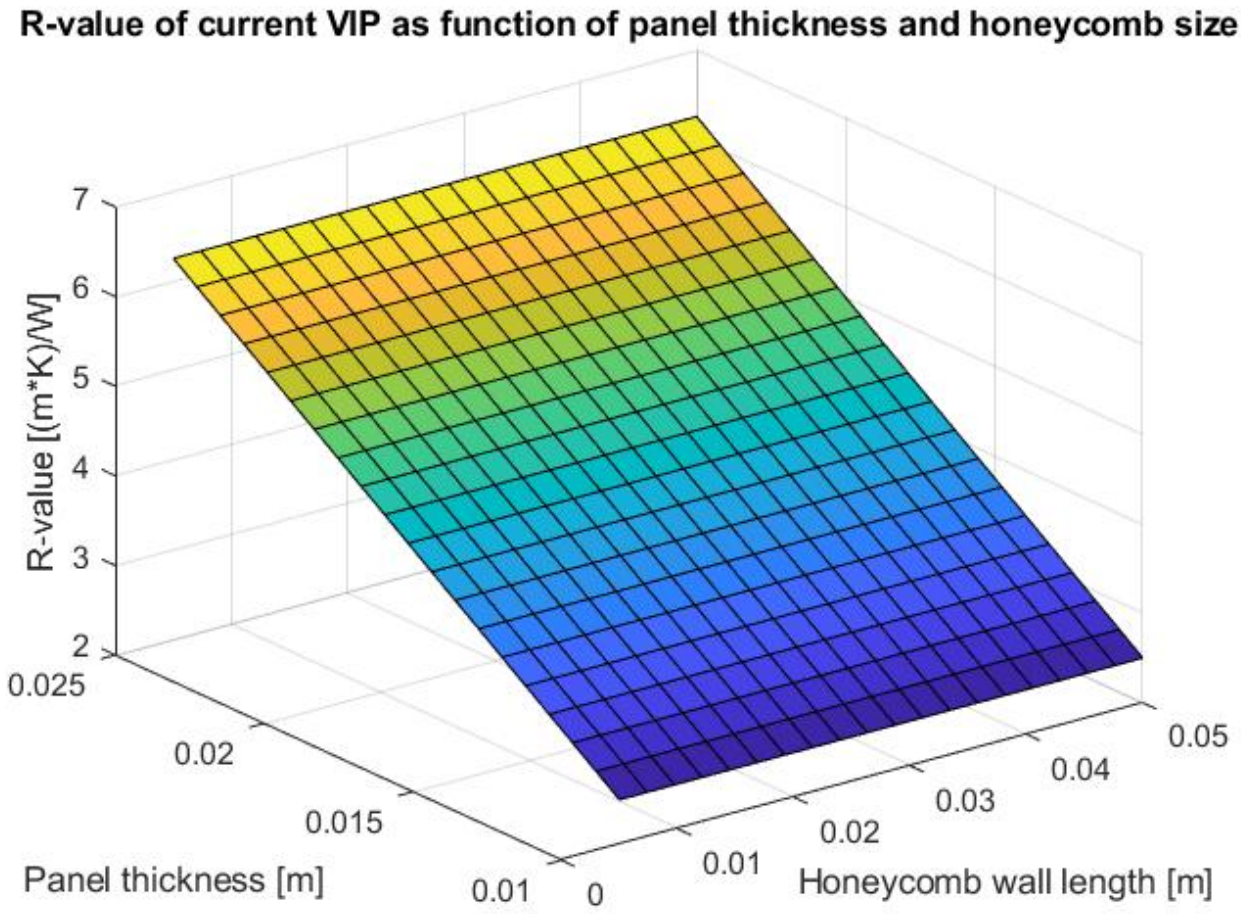

Figure H.1: R-value of conventional VIPs as function of panel thickness and honeycomb wall length.

Appendix I Buckling

I.1 Buckling equations

The first plastic-elastic buckling bifurcation point can be calculated with Equation (I.1) [26]. Parameters used in this equation are expressed as a function of material parameters and geometry in Equations (I.2) to (I.6). Equation (I.1) can be solved for honeycomb thickness.

$$p_{ext}\left(\frac{1}{\sum_x}+\frac{1}{\Psi_x}\right)+p_{ext}\left(\frac{1}{0.346\phi_y\sum_y}-\frac{1}{\Psi_y}\right)=1 \tag{I.1}$$

Where:

$$\phi_y=\sin(\theta) \tag{I.2}$$

$$\sum_x=\frac{\pi^2 E_h t_h^3}{12L_h^2\cos\theta(L_h+L_h\sin\theta)} \tag{I.3}$$

$$\sum_y=\frac{\pi^2 E_h t_h^3}{12L_h^3\cos\theta\sin\theta} \tag{I.4}$$

$$\Psi_x=\frac{t_h^2\sigma_{y,h}}{2L_h(L_h+L_h\sin\theta)\sin\theta} \tag{I.5}$$

$$\Psi_y=\frac{t_h^2\sigma_{y,h}}{2L_h^2\cos^2\theta} \tag{I.6}$$

I.2 Critical buckling load for literature comparison

As mentioned in Section 5.2.2, Klintworth et al. [26] provide equations for the bifurcation points or planes where buckling of honeycomb plates occur. Papka et al.[38] used the setup, shown in Figure I.1 to crush a honeycomb in one direction. Figure I.2 shows the corresponding force-displacement response. Bifurcation surfaces for mode 1 and 5 are approximated with Equations (I.7) and (I.8) respectively by Klintworth et al. [26]. Point A corresponds with buckling mode 1 and a with mode 5. Load directions of σ_x and σ_y are shown in Figure I.3. The tested honeycomb plates by Papka et al. were crushed in the direction of σ_y. Therefore, σ_x is equal to zero. σ_y for both modes can be obtained from Figure I.2. Equations (I.7) and (I.8) should hold if all other honeycomb parameters in Equations (I.2) to (I.6) are also chosen such that they correspond with the parameters of the tested honeycombs. However, working out the left sides in Equations (I.7) and (I.8) (and checking if they are indeed equal to one) is not particularly useful. Instead, solving Equations (I.7) and (I.8) for t_h gives the thickness for which the honeycomb plates will buckle at the given loads. This thickness is therefore the minimum required honeycomb wall thickness to eliminate the failure mode buckling.

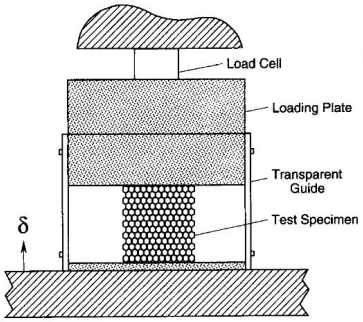

Figure I.1: Schematic of test fixture used for in-plane crushing of a honeycomb plate [38].

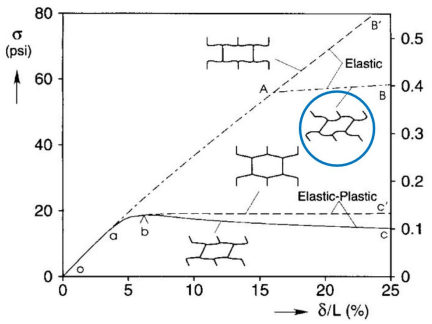

Figure I.2: Force-displacement response of crushed honeycomb plate [38].

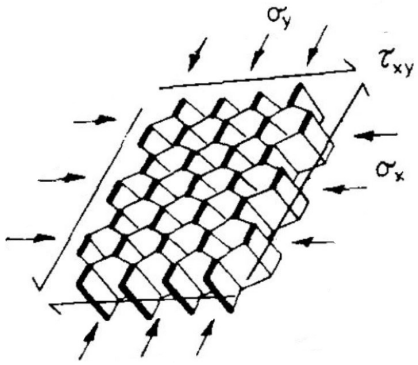

Figure I.3: Honeycomb load conditions [26].

The thickness of the tested honeycomb plates (by Papka et al.) was 0.145 mm. Critical thickness from solving Equation (I.7) for point A and Equation (I.8) for point a is equal to 0.142 and 0.143 mm. These values are similar to the tested 0.145 mm plates. Equation (I.8) can now be used confidently to estimate the minimum required thickness of the honeycomb plates. Both load directions equal the external air pressure for the concept vacuum insulation panel. Therefore, Equation (I.1) shows the relevant form of Equation (I.8) for the panel.

$$-\frac{\sigma_x}{\sum_x} - \frac{\sigma_y}{0.346\Psi_y \sum_y} = 1 \tag{I.7}$$

$$-\sigma_x \left(\frac{1}{\Sigma_x} + \frac{1}{\Psi_x}\right) - \sigma_y \left(\frac{1}{0.346\Phi_y \Sigma_y} - \frac{1}{\Psi_y}\right) = 1 \tag{I.8}$$

Appendix J Literature survey chapter 3.4: Performance of existing VIPs

J.1 Thermal performance

Thermal conductivity of isolated vacuum insulation panels ranges from 4 $mWm^{-1}K^{-1}$ at the start of the panel lifetime to 8 $mWm^{-1}K^{-1}$ at the end [12, 42–45], although conductivity of actual panels in operating conditions might be slightly higher than the claimed performance [46, 47]. Edge losses in operating conditions are a significant contributor to this lower performance [12, 34]. Regardless of the increase in thermal conductivity, the VIPs still significantly outperform the conventional insulation materials shown in Table J.1. This enables VIPs to be thinner than conventional materials for similar heat transfer, which is graphically represented in Figure J.1.

Insulation material	λ [$mWm^{-1}K^{-1}$]	Cost [€ /m^2]	Refs
EPS	35	32	[43, 48–51]
XPS	33	46	[48–51]
PU	25	59	[43, 48, 50–52]
Rock wool	40	36	[49, 50, 52–54]
Glass wool	38	43	[50, 51, 53, 54]

Table J.1: Thermal conductivity and cost per square-metre calculated for set R-value of 10 m^2KW^{-1} of insulating materials, part of Table from [55].

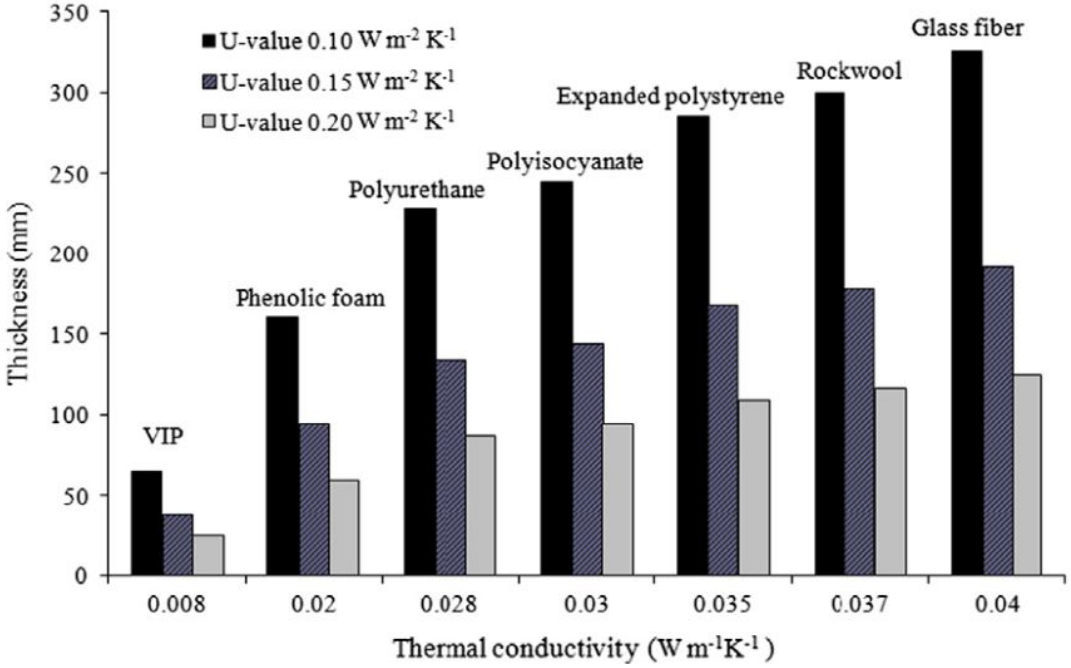

Figure J.1: Thicknesses of different insulation materials required to achieve different U-values $Wm^{-2}K^{-1}$ [10].

Since the core used in current VIP designs is just a simple block of material, the only relevant parameter to compare performance between different panel types is, edge losses asides, the thermal conductivity of the material. Especially if standard size panels are constructed and tested, the thermal conductivity is the only parameter affecting the total insulating performance of the panel. The R-value does change if the panel is scaled or stacked.

Insulation	R value for a 25mm thick panel [Km^2/W]
VIP - evacuated	3.1
VIP - atmospheric pressure in core	1.1
Phenolic foam	1.3
Polyurethane foams	1.0
Polyisocyanate	0.83
Extruded polystyrene	0.76
Expanded polystyrene	0.71
Glass wool	0.66
Rock wool	0.63
Glass fibre	0.63

Table J.2: Insulation materials and their R-value for a 25 mm thick panel.

The thermal conductivity of VIPs depends on the air pressure inside the core. Normally, a vacuum is present inside the core. If the panel envelope is perforated however, the air pressure inside the core of the panel will quickly rise to atmospheric pressure. For intact panels with a fumed silica core the conductivity lies around 8 $mWm^{-1}K^{-1}$ at end of life [42]. For panels with no vacuum present anymore, the conductivity lies around 22.5 $mWm^{-1}K^{-1}$ [47]. The corresponding R-values for a 25mm thick panel are 3.1 Km^2/W with internal vacuum and 1.1 Km^2/W without. These values are compared to conventional insulation materials for equal thickness in Table J.2. The damaged VIP still outperforms nearly all conventional insulation materials in the area of thermal insulation.

J.2 Service lifetime

The range in thermal conductivity discussed in the previous section is a result of aging. The aging mechanisms of the panel and the definition of total service life are discussed in this section. Panel lifetime is linked with the economical and environmental feasibility of VIPs compared to conventional insulation materials. Before it is possible to quantify lifetime, it is necessary to define the factors contributing to a decline in performance of the panel first.

Mechanical failure in the form of creep will not be a problem in current VIPs since the compressive strength and the maximum service temperature of the fumed silica core are far higher than the service conditions of regular buildings insulation [56]. The main failure mechanism of current panels is leakage through the barrier envelope. This can occur for three different reasons. Two cause immediate failure of the panel: defects in the foil caused by faulty production of the panel and mechanical damage occurring in the operation phase. A small tear in the envelope enables air from the surroundings to enter the panel, eradicating the vacuum inside. The last failure mechanism is slow permeation of air and water vapour through the barrier foil. This happens even if the foil is fully intact [12, 13].

The last mentioned failure mechanism is the most interesting to study in more detail. The first two mechanisms can easily be countered by testing the panels before operations and replacing faulty panels. Protective layers around the panel could solve the issue of failure due to damage of the fragile envelope. An easy fix for the slow permeation through the barrier does not exist. Therefore, predictions for the panel lifetime are required.

Diffusion of air and water vapour over time both contribute to an increase in the thermal conductivity of the panel. The useful service life of a VIP ends when it exceeds a certain threshold. This maximum value for the thermal conductivity defines the lifetime of a panel

[57, 58]. A value of 8 $mWm^{-1}K^{-1}$ is often used for this upper limit [59].

Simple models show an inner pressure increase due to gaseous diffusion of 0.01 to 1 mbar per year [13]. Figure J.2 graphically shows the increase in thermal conductivity as a function of pressure increase. Water vapour also diffuses in and reaches equilibrium at a partial pressure between 10 to 20 mbar. Studies [12, 60–62] show an increase in conductivity due to water vapour content of approximately 0.5 $mWm^{-1}K^{-1}$ per mass percent water. A final increase of 2 $mWm^{-1}K^{-1}$ is reached at saturation. Combined with the increase due to air diffusion, the total thermal conductivity reaches a value of around 8 $mWm^{-1}K^{-1}$ after 25 years [13, 42].

The equation for the overall time dependent thermal conductivity of the panel is shown in Equation (J.1) [39]. The time dependent variables of this equations are further specified in Equations (J.2) to (J.4) [39]. The underlying equations describing these variables or constants are not inserted in this report for the sake of readability, but an overview of the variables and their meaning can be found in Table A.1 in Appendix A. As discussed in Appendix D, the diffusion rates of gas and water vapour depend on the envelope type. A graphical representation of the total increase in thermal conductivity with time for different types of foils is shown in Figure J.3.

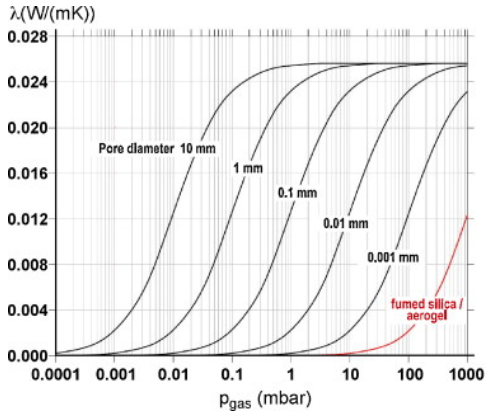

Figure J.2: Thermal conductivity of air as a function of the air pressure and the average pore diameter of the medium [12].

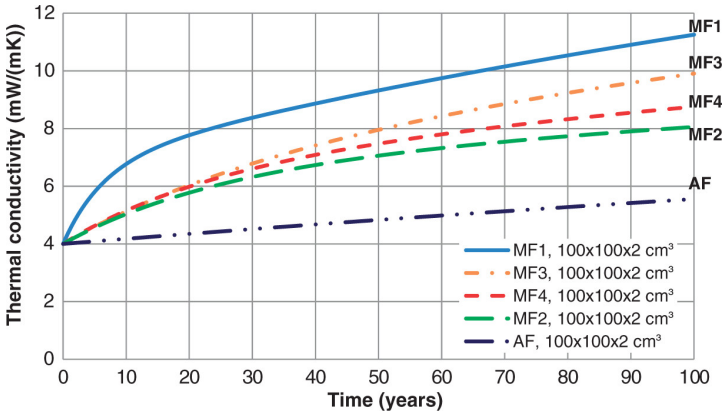

Figure J.3: Total thermal conductivity for various laminate types. Note: The inner air pressure is assumed to be zero at t=0. It is assumed that laminate properties remains the same during the entire period. No getters and desiccants have been taken into account [39].

$$\lambda_c(t) = \lambda_{evac} + \lambda_g(t) + \lambda_{wv}(t) + \lambda_w(t) \tag{J.1}$$

Where:

$\lambda_c(t)$ = Total thermal conductivity of the panel over time.
λ_{evac} = Thermal conductivity of the evacuated panel (start state).
$\lambda_g(t)$ = Conductivity of permeated air gasses over time.
$\lambda_{wv}(t)$ = Conductivity of permeated water vapour over time.
$\lambda_w(t)$ = Conductivity of absorbed water in the core material over time.

$$\lambda_g(t) = \frac{\lambda_{g,0}}{1 + p_{1/2,g}/p_g(t)} \tag{J.2}$$

$$\lambda_w(t) = \frac{\partial \lambda_c}{\partial u} \frac{\mathrm{d}u}{\mathrm{d}\varphi} \varphi_e (1 - e^{-t/\tau_w}) \tag{J.3}$$

$$\lambda_{wv}(t) = \frac{\lambda_{wv,0}}{1 + p_{1/2,wv}/p_{wv}(t)} \tag{J.4}$$

Equations for the time dependent terms in Equations (J.2) and (J.4) are shown in Equations (J.5) and (J.6) [39].

$$p_g(t) = (1 - e^{-t/\tau_g}), \tag{J.5}$$

$$p_{wv}(t) = (1 - e^{-t/\tau_{wv}}). \tag{J.6}$$

Getters and desiccants in the vacuum chamber can prolong the service life. The gas pressure and water vapour content inside the core remain constant until the getters and desiccants are saturated. Thereafter the aging behaviour for panels containing saturated getters and desiccant will be the same as for panels without added chemicals. This delay in aging can be represented by adding a time shift t_{get} and t_{des} to Equations (J.5) and (J.6) resulting in Equations (J.7) and (J.8). Equations (J.9) and (J.10) show the expressions for the time shifts [63].

$$p_g(t) = (1 - e^{-(t-t_{get})/\tau_g}), \tag{J.7}$$

$$p_{wv}(t) = (1 - e^{-(t-t_{des})/\tau_{wv}}). \tag{J.8}$$

$$t_{get} = \frac{c_{get} m_{get}}{GTR(T, \phi)(p_{g;e} - p_{g;i;0})} \tag{J.9}$$

$$t_{des} = \frac{c_{des} m_{des}}{WVTR(T, \phi)(p_{wv;e} - p_{wv;i;0})} \tag{J.10}$$

J.3 Economical feasibility

Two studies on the economical feasibility of implementation of vacuum insulation panels in buildings have been done. Both show a Life Cycle Cost Analysis, or LCCA.

The first of the two studies was published in 2013 and shows a comparison between two VIPs (20 mm and 30 mm thickness) and conventional styrofoam insulation panels (SIP) [44]. The first difference between the VIP and the conventional insulation material is the price per square-metre. The price of vacuum insulation panel depends on many factors such as thickness, producer, quality and materials used. This dependence results in different prices in literature [14, 44, 46, 64]. The price for the 20 mm and 30 mm VIPs used in [44] is 41.41 and 62.49 euro per square-metre respectively and for conventional SIP a price of 5.92 euro per square-metre is used.

The three insulation techniques were tested for a prototype house, representing standard housing. The initial costs for the complete insulation of the prototype house with vacuum insulation panels is much higher compared to the use of SIP. However, the total life cycle costs of the vacuum insulation panels are much lower when the total energy saving per year is taken into account. The paper [44] concludes that a 88.28 and a 136.92 percent economic advantage can be achieved with the 20mm and 30mm thick panel respectively after 40 years.

This result shows that VIPs could be economically beneficial for the insulation of housing, but the result itself is not very informative. The lifespan of the panels is simply set to 40 years,

which could be a stretch based on the information discussed in Appendix J.2. No effects of aging of the panels are taken into account either. The conductivity of the panel remains unchanged for the total lifetime of the panel. Furthermore, the results of this paper are only valid for these panels used in this specific prototype house.

A newer publication (2021) [14] is aiming to bridge these gaps. This paper compares VIPs to EPS instead of SIP. The first main difference is that the initial price is given in price per cubic-metre. This is useful since it can be used to calculate the price per square-metre for all thicknesses. The VIPs are 3000 euro per cubic-metre and EPS comes in at 120 euro per cubic metre. Next, new elements of influence are added to the LCCA. Floor area increases when the thinner VIP insulation is used, compared to the conventional insulation. This extra floor space results in higher property value or more rentable space, resulting in more income. Also, the rental price per square metre of an apartment is added in the analysis. Furthermore, a difference in service lifetime is added. The VIPs now have a lifetime of 25 years and EPS 40 years.

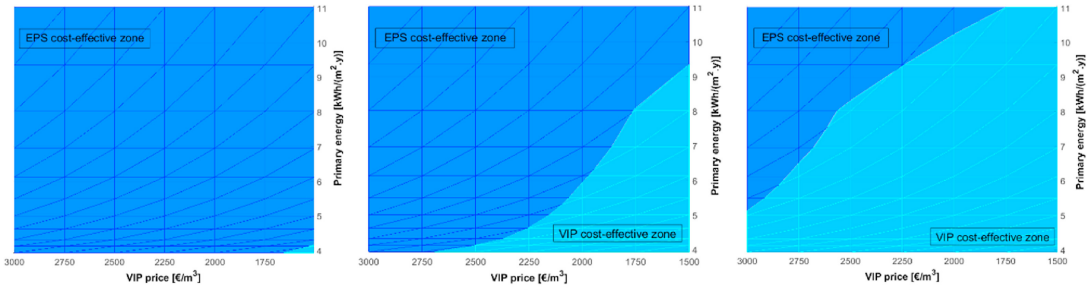

Figure J.4: VIP price analysis for financial perspective: a) fixed rental cost of 150 € $m^{-2}year^{-1}$; b) fixed rental cost of 250 € $m^{-2}year^{-1}$; c) fixed rental cost of 350 € $m^{-2}year^{-1}$ [14].

The result of this study shows that the VIPs are not always the most economic solution. Figure J.4 shows that the VIP cost effective zone is strongly dependent on panel price for all three fixed rental prices. With the current, high panel price, the existing VIPs only become attractive for the higher rental prices. Rental prices in the Netherlands are currently between 120 and 200 € $m^{-2}year^{-1}$ with the exception of 240 € $m^{-2}year^{-1}$ for Amsterdam [65]. These prices are comparable with situation a) in Figure J.4, which shows that installing existing VIPs is not a viable option. Figure J.5 shows that the required payback period, like cost effectiveness, also dependents on the initial panel price. This figure also shows the influence of panel thickness is very large at small thicknesses and relatively small at larger thickness.

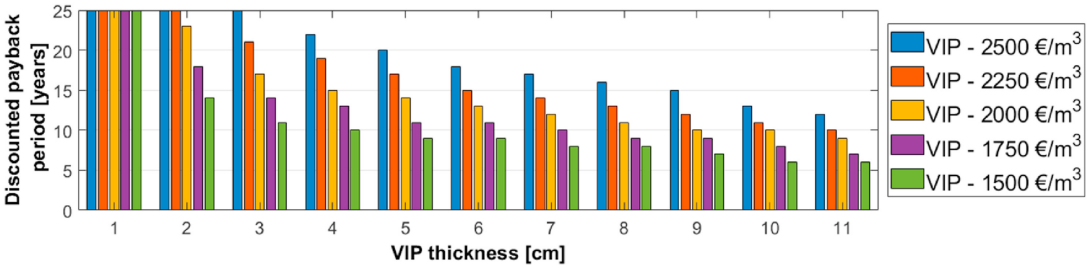

Figure J.5: Discounted payback period results for financial perspective – VIP price analysis [14].

The conclusion of this paper states that the VIPs are not feasible in most cases because of their high pricing. Vacuum insulation only becomes an attractive solution in the more expensive housing range. The main components contributing to an economically beneficial panel design mentioned in this paper were panel price, thermal insulation performance and panel thickness.

Retrofitting buildings with VIPs is even less viable than the results of [14] show. This paper compares costs of VIPs with EPS. Costs that are equal for both materials, like removing the existing insulation material, are not taken into account since they do not favor either one above the other. These costs are present for retrofitting houses however. Di Giuseppe et al. [66] state that benefits from retrofitting with current VIPs never outweigh the investments costs.

J.4 Environmental impact

Karami et al. [36] provide a complete overview of the values for the environmental impact factors mentioned in Section 2.2.4 of two types of conventional insulation material (EPS and mineral wool), VIPs and different types of construction materials (not particularly relevant for this report). They describe a case study where the values for these different materials are compared in three types of buildings. The first is a standard building, the second is a well-insulated building with conventional insulation materials and the third is a well-insulated building with vacuum insulation panels. Figures J.8 to J.12 show the results for production of all products per environmental impact factor. The different building types are shown as bldg type I,II and III.

The production of VIPs scores highly on nearly all environmental impact factors and therefore has a large, negative impact on the environment. Only the ODP is higher for mineral wool than for VIPs. The GWP and PE use are especially high for VIPs, compared to the alternatives. For 1 kg of VIP the GWP ranges from 6.2 to 11.1 kg CO_2 eq and the PE from 149 to 226 MJ depending on the panel type [36, 67]. With a density ranging from 162 to 192 kg/m^3 for a panel with dimensions 300 mm $\times$ 300 mm $\times$ 25 mm [61] the GWP and PE for a panel of these dimensions roughly translates to 3.3 $\pm$ 1.3 kg CO_2 eq and 71.7 $\pm$ 21.4 MJ respectively.

Figures J.6 and J.7 show the total GWP and the PE use for complete product lifetime for the three different types of housing. The lighter bars represent the energy required to produce the insulation material and the darker bars represent the energy needed in the operation phase. The VIPs have the highest insulation value, so in both figures the black bars are the smallest. The energy saved by this insulation advantage is not enough however to compensate for the energy intensive and polluting manufacturing. The well insulated building with regular insulating material scores best in both figures. The VIP even scores the worst in the total primary energy use over total product lifetime. This concludes that the existing vacuum insulation panels are not a solution to reduce the environmental impact of the housing sector.

The problem of the current vacuum insulation panels is the high energy demand in the production phase. 90% of energy required for the construction of a total panel comes from the production of the core material [67]. The authors of [36] also conclude that the VIP offers promising energy saving potential, but that it is wise to further develop this technique with a different core material.

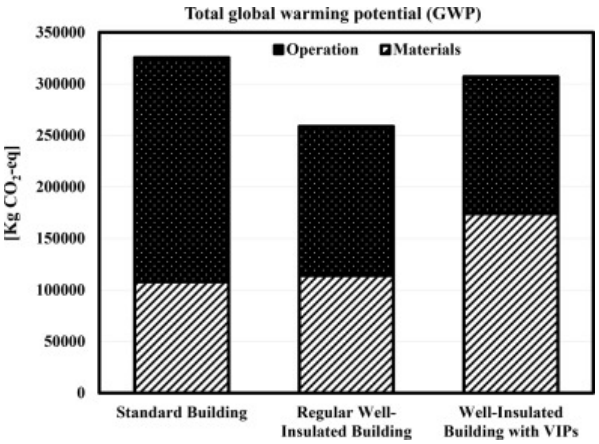

Figure J.6: Total GWP of three hypothetical buildings for production and operation [36].

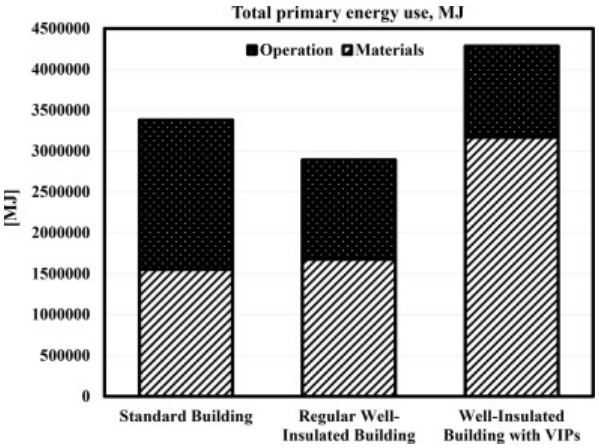

Figure J.7: Total primary energy use of three hypothetical buildings for production and operation [36].

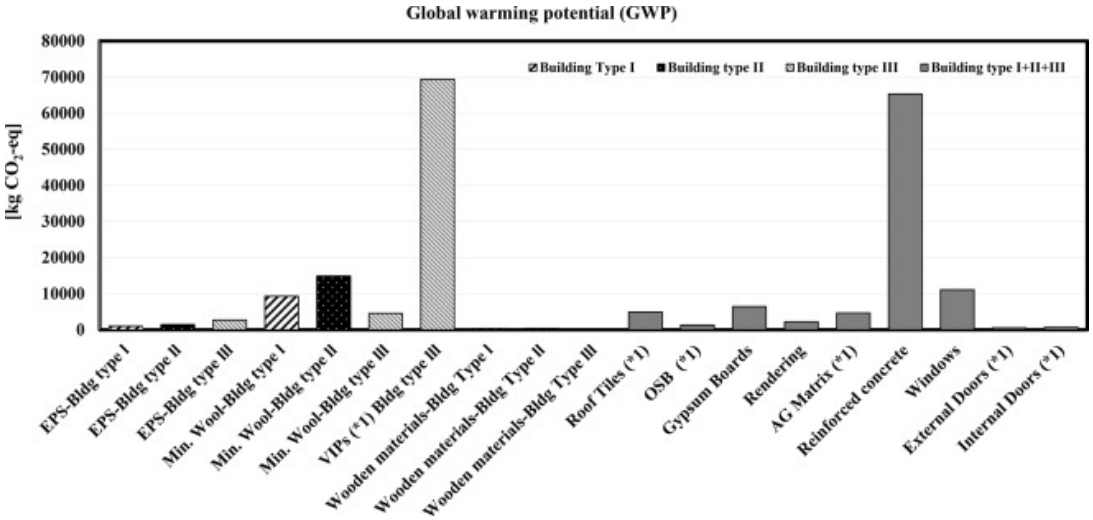

Figure J.8: The GWP of the production stage of the different building materials and components[36].

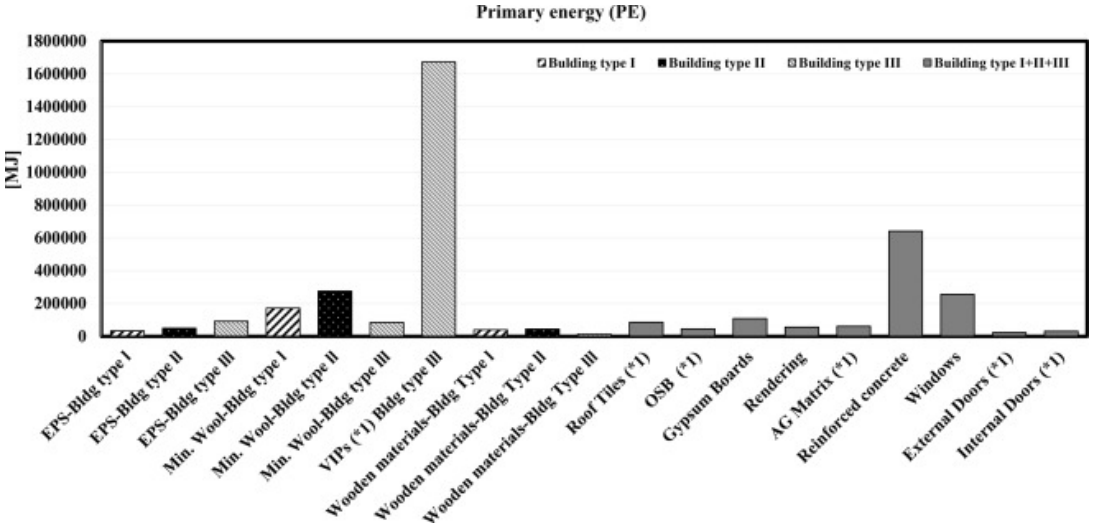

Figure J.9: The PE of the production stage of the different building materials and components [36].

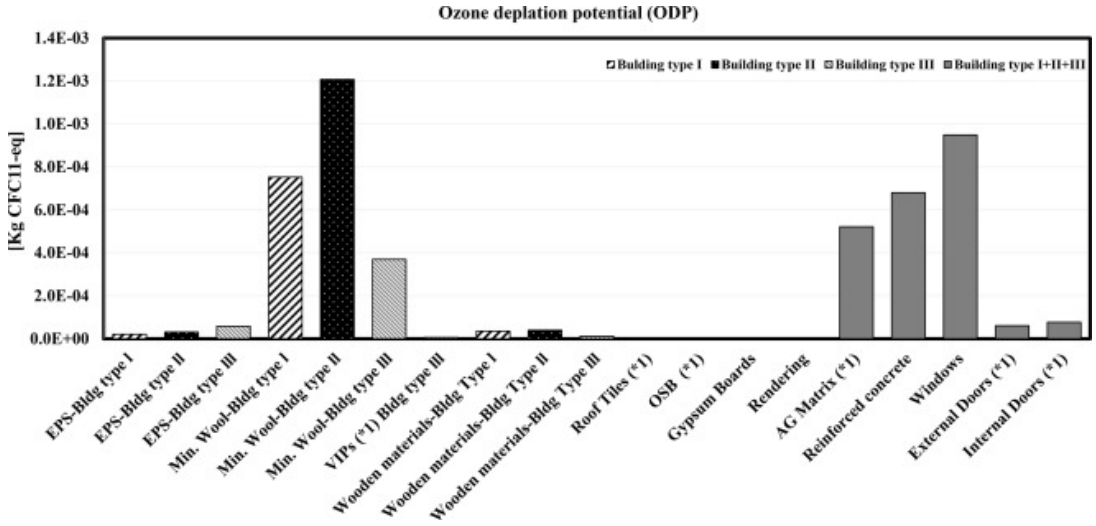

Figure J.10: The ozone depletion potential of the production stage of the different building materials and components [36].

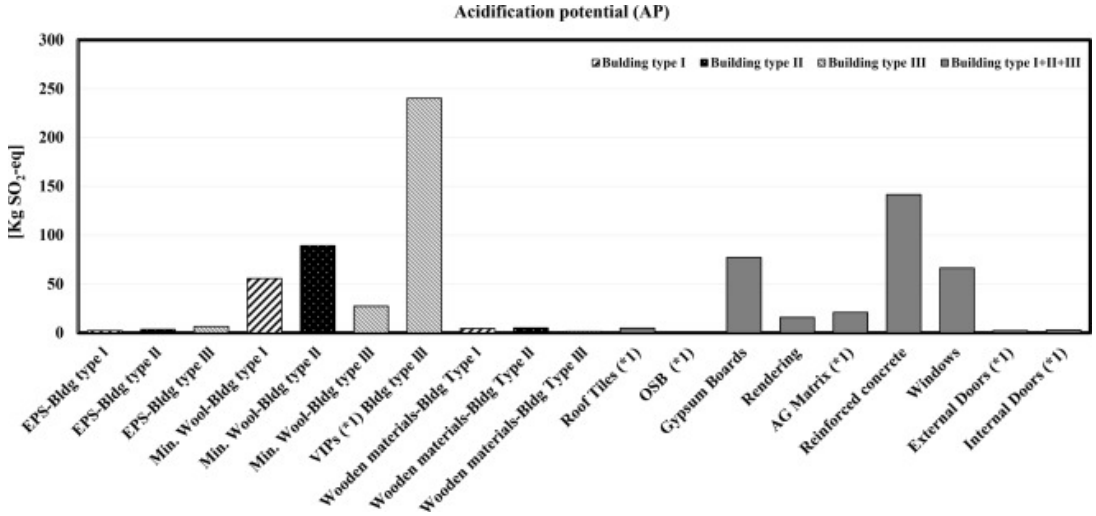

Figure J.11: The acidification potential of the production stage of the different building materials [36].

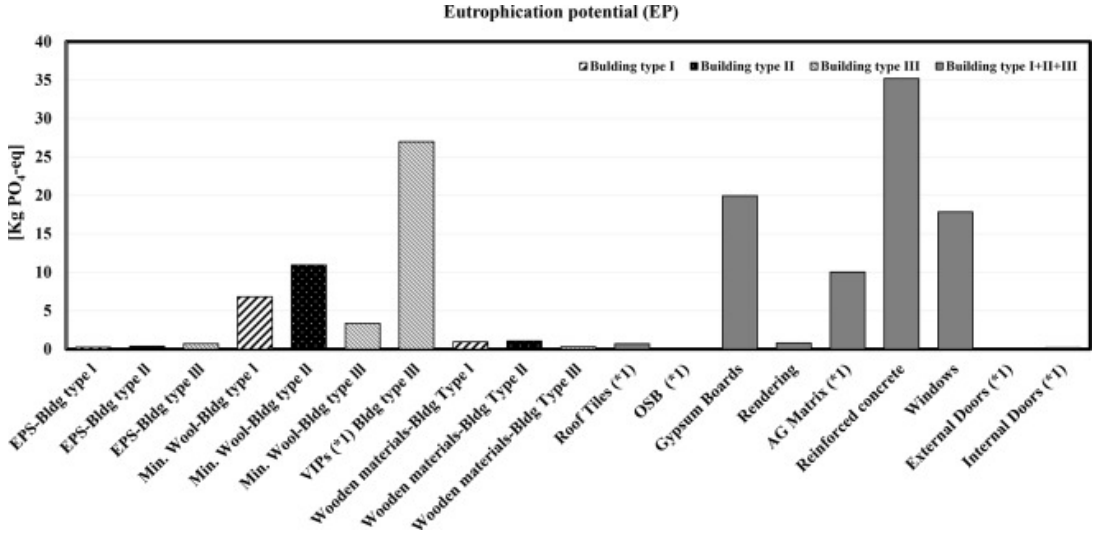

Figure J.12: The eutrophication potential of the production stage of the different building materials and components [36].

Appendix K vapour pressure of materials

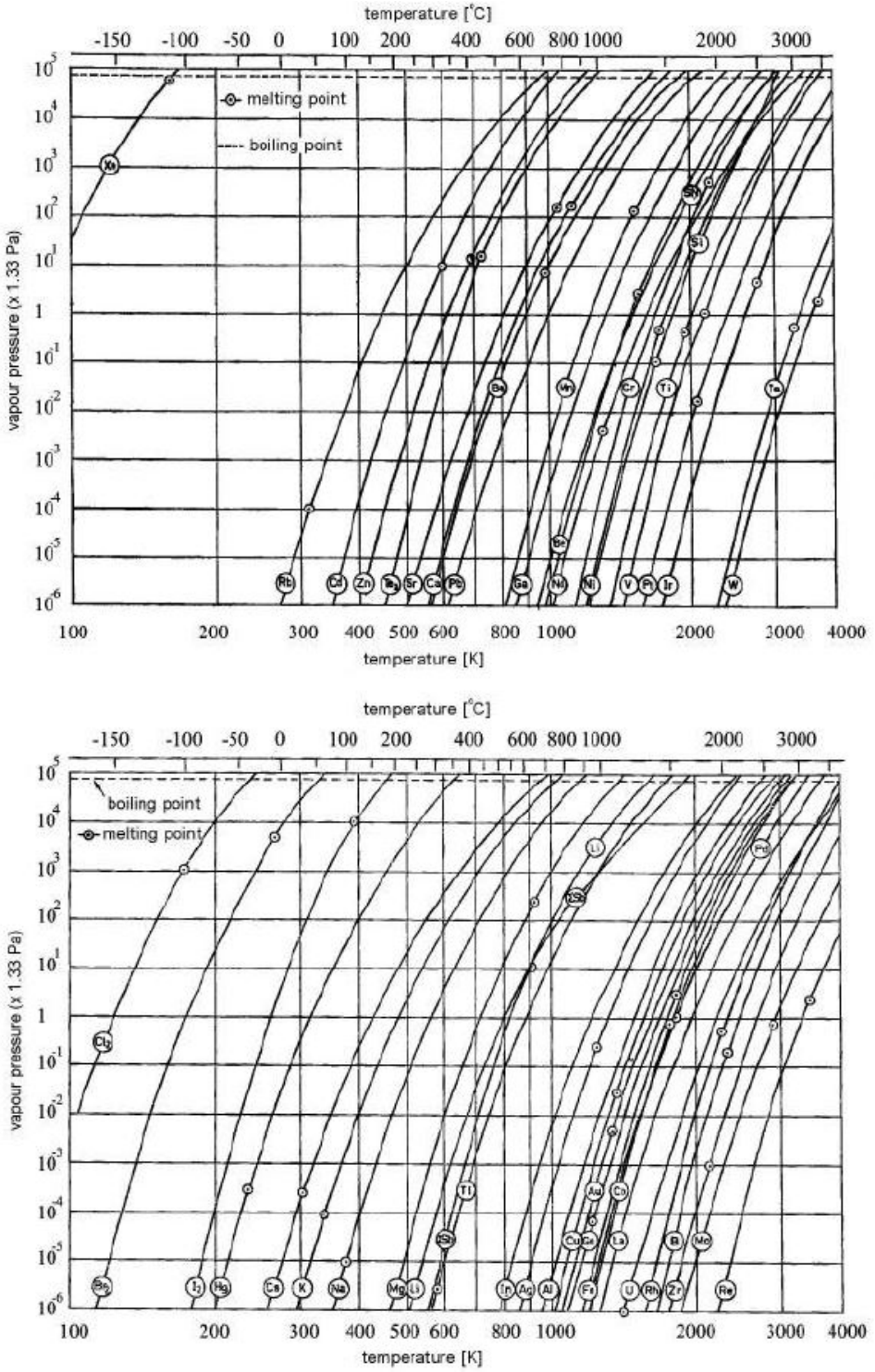

Figure K.1: Vapour pressure of some materials as a function of their temperature [33].

Symbol	Material
Xe	Xenon
Rb	Rubidium
Cd	Cadmium
Zn	Zinc
Te_2	Tellurium
Cl_2	Chlorine
Br_2	Bromine
I_2	Iodine
Hg	Mercury
Cs	Cesium
K	Potassium
Na	Sodium

Table K.1: Materials with insufficiently high vapour pressures at T=50°C.

Appendix L Ashby graphs for the honeycomb plates' material indices

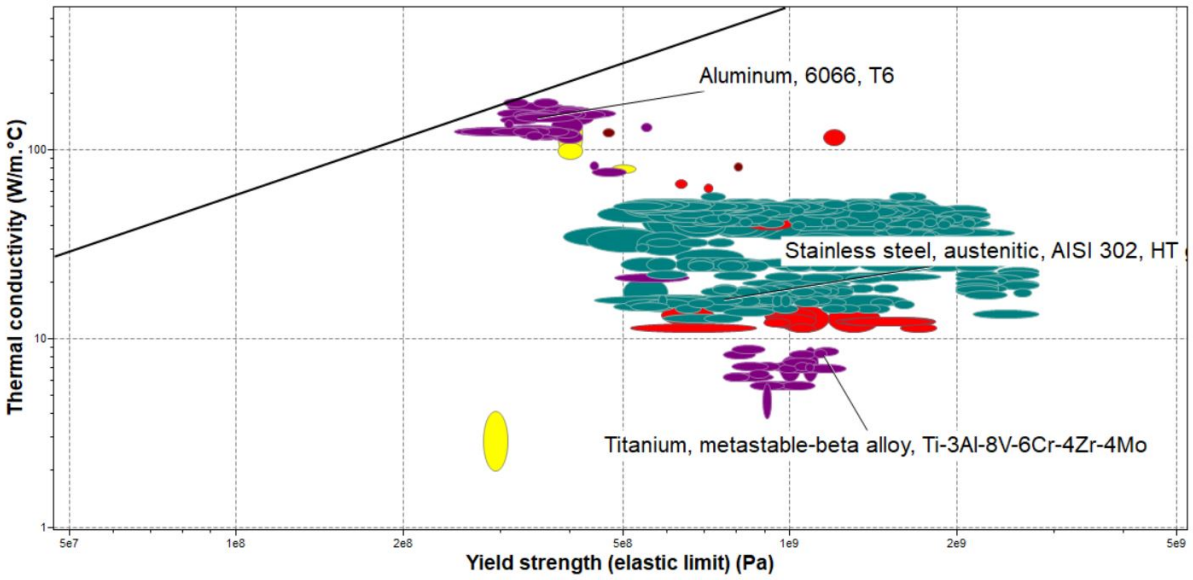

Figure L.1: Ashby graph for honeycomb material index optimised for maximum thermal resistance to conduction [68].

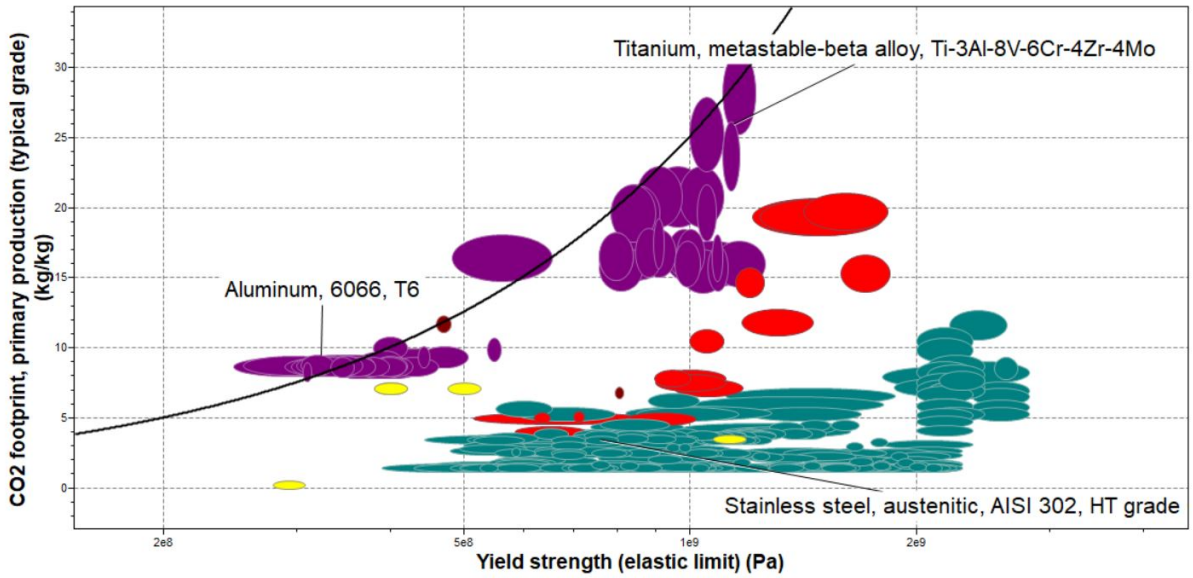

Figure L.2: Ashby graph for honeycomb material index optimised for minimum carbon footprint [68].

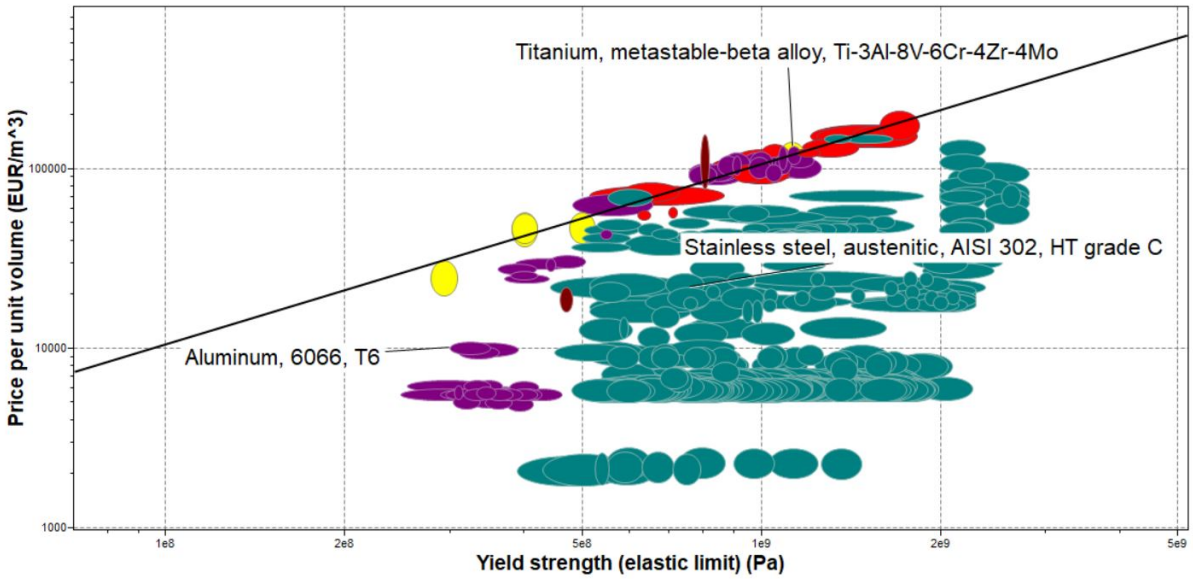

Figure L.3: Ashby graph for honeycomb material index optimised for minimum panel price [68].

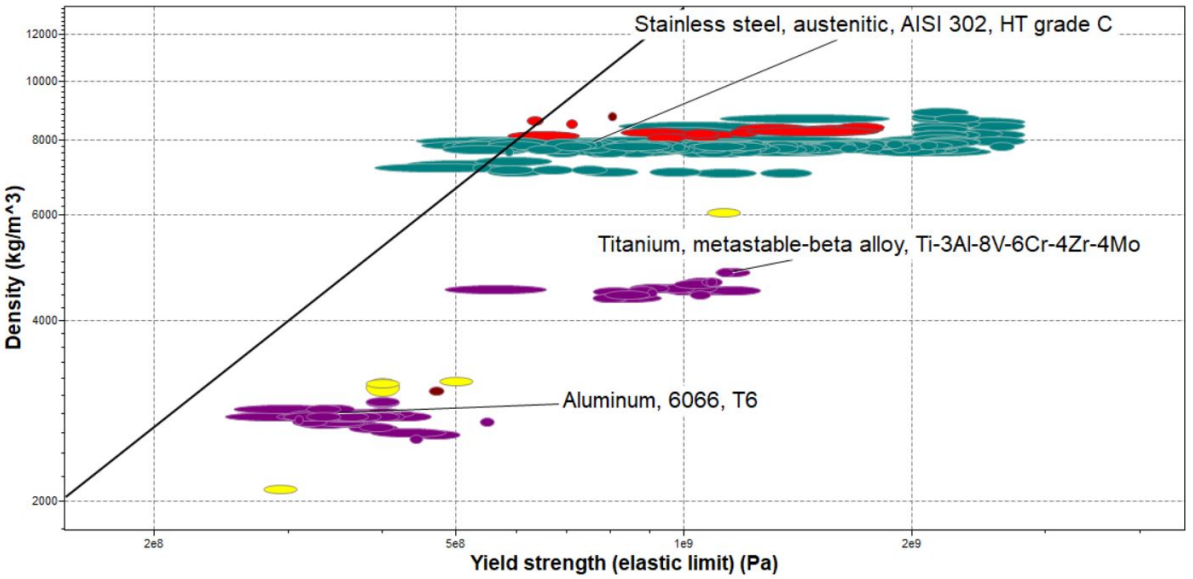

Figure L.4: Ashby graph for honeycomb material index optimised for minimum weight [68].

Appendix M Ashby graphs for the foil's material indices

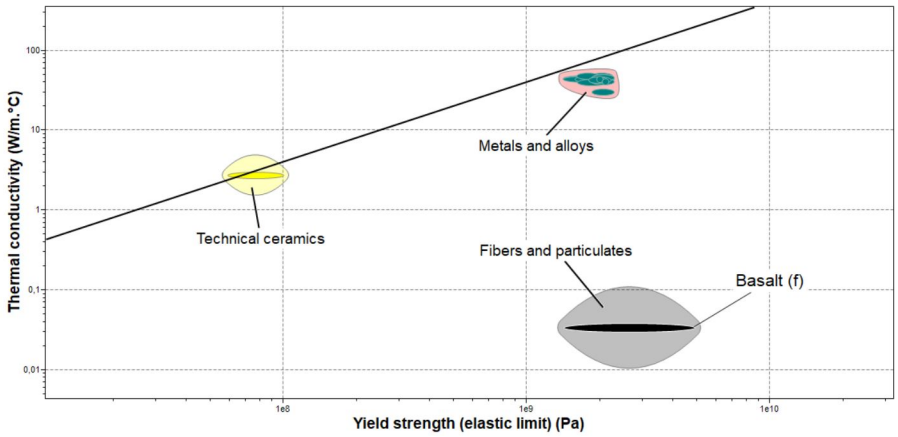

Figure M.1: Ashby graph for foil material index optimised for minimum thermal conductivity [68].

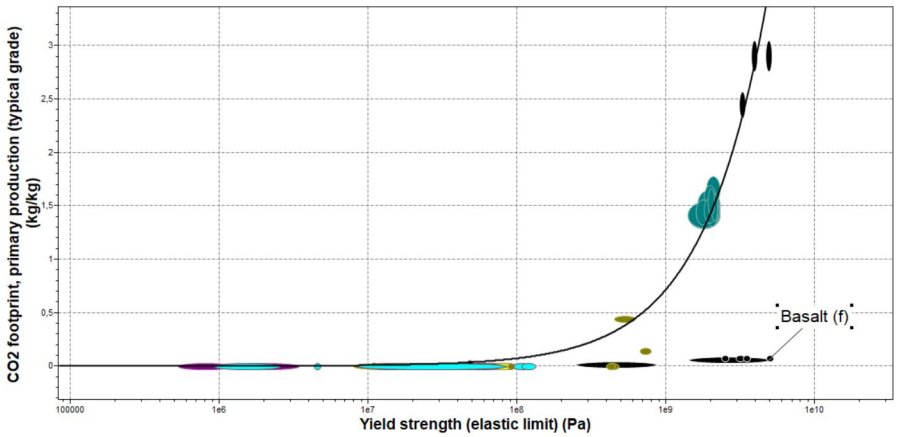

Figure M.2: Ashby graph for foil material index optimised for minimum carbon footprint [68].

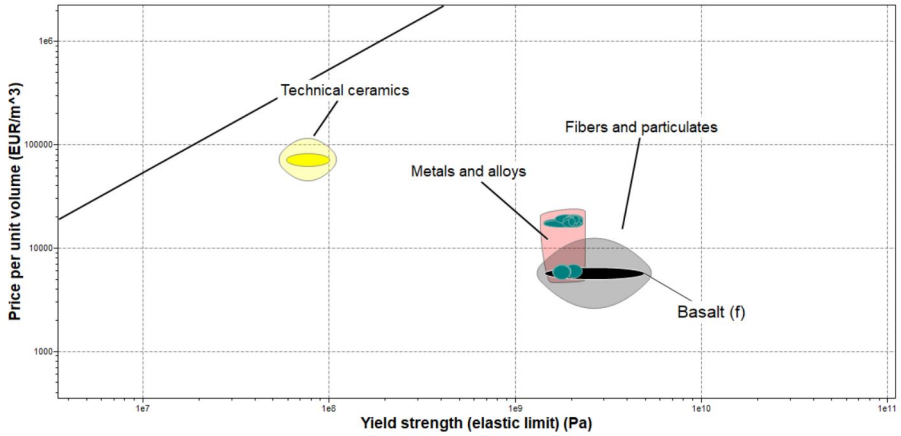

Figure M.3: Ashby graph for foil material index optimised for minimum panel price [68].

Appendix N Conductance calculations

Equations (N.1) and (N.2) [33] can be used to calculate the conductance for a rectangular tube. Shape factors f_1 and f_2 depend on characteristic lengths a and b of the tube's cross-section. Corresponding shape factors for a few tube geometries are shown in Tables N.1 and N.2 [33]. Fourth order polynomials Equations (N.3) and (N.4) can be fitted through these points, where x represents the factor b/a. The norm of residuals of 0.0022 for the f_1 fit and 0.0065 for the f_2 fit, which indicate that it is a good fit. Now values for both f_1 and f_2 can be calculated for a continuous range of a and b.

$$C_{volume,viscous} = \frac{1.92 * 10^3 a^2 b^2}{l} p f_1 \tag{N.1}$$

$$C_{volume,molecular} = \sqrt{\frac{2\pi RT}{M_{air}} \frac{a^2 b^2}{(a+b)(l+2.66ab)}} f_2 \tag{N.2}$$

Where:

a	= Longest side of rectangular tube [m]
b	= Shortest side of rectangular tube [m]
l	= Tube length [m]
p	= Air pressure [Pa]
R	= Gas constant [$m^3PaK^{-1}mol^{-1}$]
T	= Temperature [K]
M_{air}	= Molar mass of air [kg/mol]
f_1	= Form factor [-]
f_2	= Form factor [-]
A_{tube}	= Cross-sectional area of the rectangular tube [m^2]
$A_{orifice}$	= Area of the orifice [m^2]

b/a	f_1
0.1	0.23
0.2	0.42
0.3	0.58
0.4	0.71
0.5	0.82
0.6	0.90
0.7	0.95
0.8	0.98
0.9	0.98
1	1

Table N.1: Shape factor f_1 for laminar conductance of rectangular tubes [33].

$$f_1(x) = 0.9504x^4 - 2.5152x^3 + 2.5059x^2 - 1.1754x + 0.7045 \tag{N.3}$$

$$f_2(x) = 0.7867x^4 - 1.3500x^3 - 0.5813x^2 + 2.1168x + 0.0267 \tag{N.4}$$

b/a	f_2
0.1	0.61
0.2	0.55
0.4	0.50
0.6	0.48
0.8	0.47
1	0.47

Table N.2: Shape factor f_2 for molecular conductance of rectangular tubes [33].

The unit cube is a short rectangular tube with a unit structure placed in this tube. The unit structure inside the unit cube lowers the conductance by blocking most of the flow path. The openings where air can flow through are the cutouts made in the diagonal honeycomb walls. Air can flow through the panel in two directions, shown in Figure N.1. The conductance differs for both flow directions. The front and side view of the unit structure are shown in Figures N.2 and N.4 respectively. The total orifice area is a multiple of the area of a single orifice. The height and width of the single orifice triangle are indicated by h and w respectively. Height h equals the cutout height. Width w is determined by projecting the diagonal wall on the front or side plane. Therefore, it is equal to $\sin(\theta)l_h$ for the front view and $\cos(\theta)l_h$ for the side view. The slope of the diagonal wall is equal to height h divided by width w and will, from hereon, be referred to with a, also indicated in Figures N.2 and N.4.

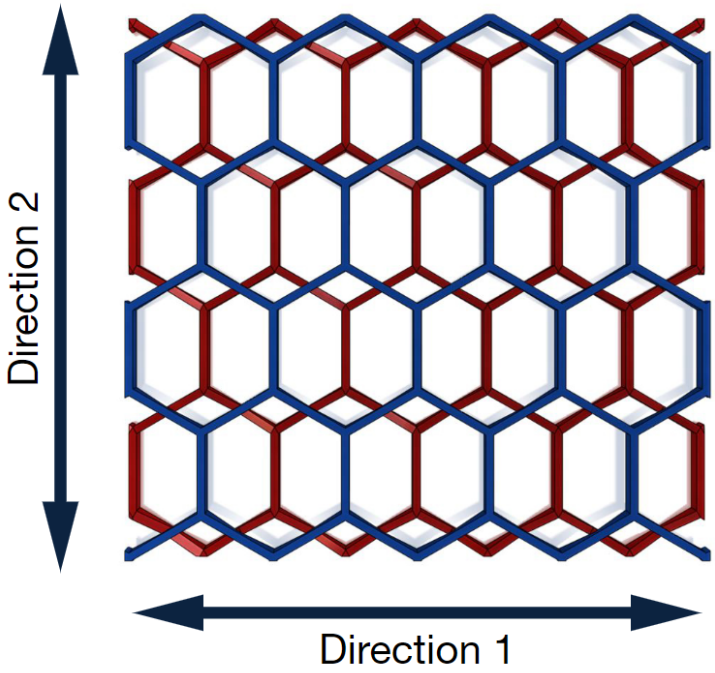

Figure N.1: Top view of the panel with indicated flow directions

The orifices' area decreases when the panel is evacuated due to the deflection of the foil. Graphical representations of the remaining open areas for the front and side view of the panel are shown (not to scale) in Figures N.3 and N.5 respectively. The area of the reduced single orifice can be calculated with Equation (N.5) for both sides. The total orifice areas for the front and side view of the unit structure can be calculated with Equations (N.7) and (N.8) respectively. Hereby, the effect of the foil is neglected since its thickness is assumed to be negligibly small. Furthermore, note that w in these equations needs to be substituted by $\sin(\theta)l_h$ or $\cos(\theta)l_h$,

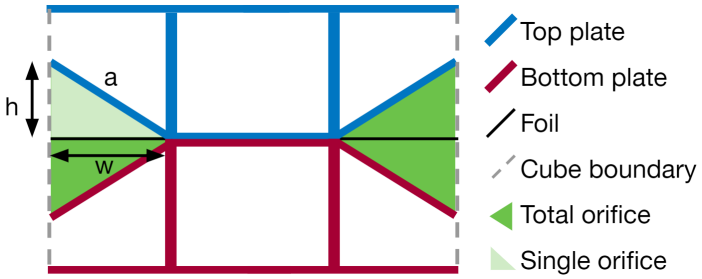

Figure N.2: Schematic front view of the unit structure (flow direction 1).

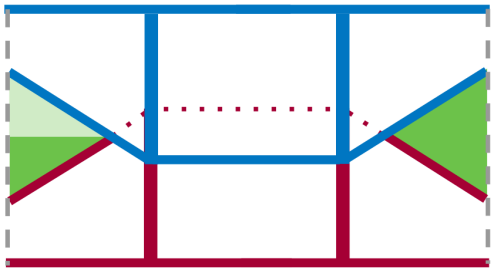

Figure N.3: Schematic front view of the unit structure after deflection (flow direction 1). Legend shown in Figure N.2.

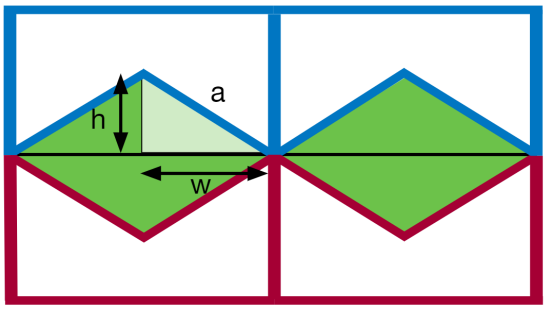

Figure N.4: Schematic side view of the unit structure (flow direction 2). Legend shown in Figure N.2.

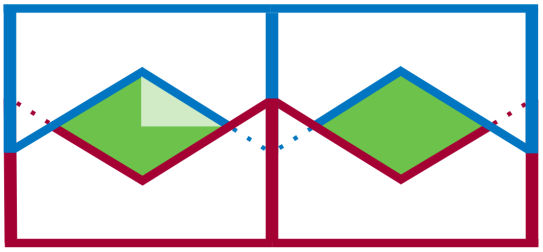

Figure N.5: Schematic side view of the unit structure after deflection (flow direction 2). Legend shown in Figure N.2.

depending on the side.

$$A_{single,orifice} = \frac{1}{2}(h - dz)(w - \frac{h - dz}{a}) \quad \text{(N.5)} \qquad C_{orifice} = \sqrt{\frac{RT}{2\pi M_{air}}}\frac{A_{tube}A_{orifice}}{A_{tube} - A_{orifice}} \quad \text{(N.6)}$$

$$A_{orifice,front} = 2(h - dz)(w - \frac{h - dz}{a}) \quad \text{(N.7)} \qquad A_{orifice,side} = 4(h - dz)(w - \frac{h - dz}{a}) \quad \text{(N.8)}$$

The conductance of a wall with an orifice of arbitrary shape can be calculated with Equation (N.6) [33]. Both viscous and molecular flow occur in parallel. The total conductance can be calculated with Equation (N.9) [33]. Both the viscous and molecular flow consists of the volume conductance and the conductance of a wall with an orifice. The total conductance of a single unit cube for one flow direction can be calculated with Equation (N.10). The total panel can be constructed with a grid of unit structures. The total equivalent conductance of the grid can be calculated with Ligong Han's resistance calculator [69].

$$C_{tot} = C_{viscous} + C_{molecular} \quad \text{(N.9)}$$

$$C_{unit\ volume} = \frac{1}{\frac{1}{C_{orifice}} + \frac{1}{C_{volume,viscous}}} + \frac{1}{\frac{1}{C_{orifice}} + \frac{1}{C_{volume,molecular}}} \quad \text{(N.10)}$$

Appendix O Mesh convergence of FEM models

O.1 General approach

Models used in finite element simulation are divided up into a finite amount of small elements. Each element has a certain amount of degrees of freedom (DOF), depending on the element order. The total amount of degrees of freedom in a model is determined by the amount of DOF in a single element and the amount of elements present in a model. A higher amount of DOFs gives more accurate results, but also increases computation time. Therefore, it is essential that the total number of DOFs is kept as low as possible whilst still achieving a converging solution.

A mesh convergence study for all models presented in Chapter 5 will be presented here. Structural models will be evaluated first, followed by thermal models. The evaluated parameter should converge for refined models. Models can be refined by using more elements in the model mesh or by using higher-order elements. Both methods increase the number of degrees of freedom in the model.

Honeycomb walls in the symmetry model can be modelled as solids or shells. Solid honeycomb walls are meshed with three-dimensional elements. Shells on the other hand, are surfaces, so only two-dimensional elements are present in the mesh. Fewer degrees of freedom are present in this model with only shell elements. Therefore, shell elements are preferred.

Elements used in the meshes of shells can be of order 1 (linear) or 2 (quadratic) in structural performance models. Third-order elements (cubic), fourth-order elements (quartic) and fifth-order elements (quintic) can also be used in thermal models.

Mesh size is determined by 5 parameters in COMSOL multiphysics: maximum element size (1), minimum element size (2), maximum element growth rate (3), curvature factor (4) and resolution of narrow regions (5). Two general, coupled parameters are defined for mesh size: *size* and *par*. *size* ranges from 1 to 10 with steps of 1 and *par* ranges from 0.1 to 1 with steps of 0.1 for mesh refinement steps from 1 to 10. Values for mesh parameters can be calculated with Equations (O.1) to (O.5).

$$mesh1 = 0.0231^{-0.374*size} \tag{O.1}$$

$$mesh2 = 0.0093^{-0.664*size} \tag{O.2}$$

$$mesh3 = 2.1 - par \tag{O.3}$$

$$mesh4 = 1.1 - par \tag{O.4}$$

$$mesh5 = par \tag{O.5}$$

O.2 Models for structural performance

O.2.1 Verification models

Honeycomb plate

Quadratic elements have been used for the honeycomb plate model shown in Figure 5.3 in Section 5.2. Maximum stress in the model has been evaluated for a range of input described displacements. Figure O.1 shows the mesh convergence plot for an arbitrary input displacement, shown on the x-axis of Figure 5.6 in Section 5.2. Convergence can be observed in Figure O.1. The exact magnitude of the stress is not important since this value is one of many plotted in Figure 5.6 in Section 5.2.

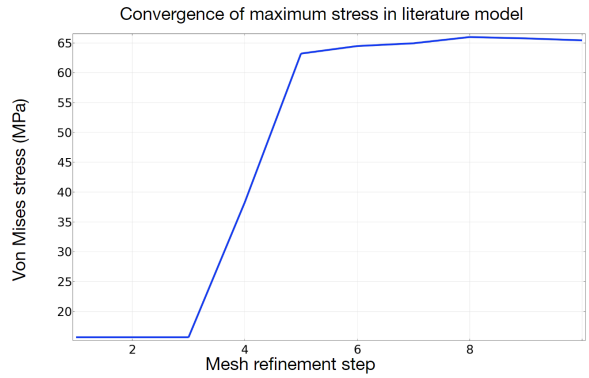

Figure O.1: Mesh convergence of stress at honeycomb wall ends for arbitrary prescribed displacement.

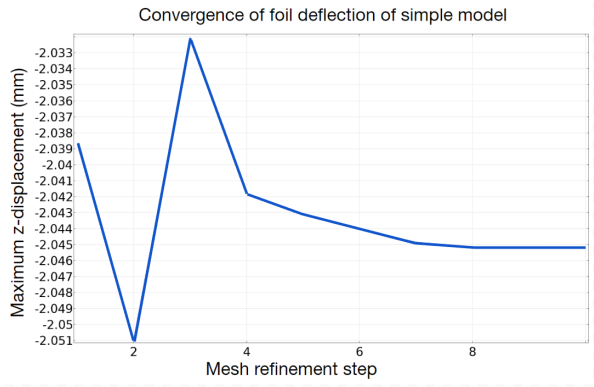

Figure O.2: Mesh convergence of maximum deflection of the foil in the simplified model.

Foil simplified model

Quadratic elements have been used in the finite element model for evaluation of maximum foil stress and deflection of the simplified model. Maximum deflection converges to -2.045 mm and foil stress converges to 962.1 MPa. Convergence plots of maximum deflecion and foil stress are shown in Figures O.2 and O.3 respectively. The maximum stress in the foil does not converge, as shown in Figure O.4. This is typical for a numeric stress singularity in the model.

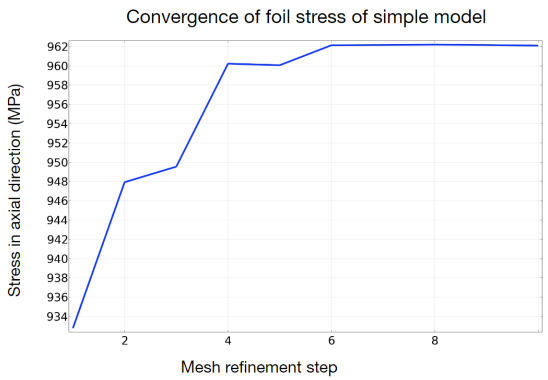

Figure O.3: Mesh convergence of axial foil stress in the simplified model.

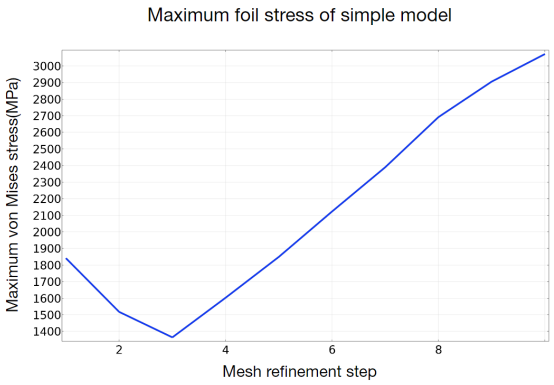

Figure O.4: Mesh convergence of maximum foil stress in the simplified model.

O.2.2 Structural performance models

Honeycomb plate

A close-up of the stress distribution in the honeycomb model for structural performance evaluation is shown in Figure O.5. Stress in the honeycomb model is evaluated at the wall end, indicated with A in Figure O.5, notch location, indicated with B and 0.05 mm below the notch, indicated with C. Quadratic elements have been used in the model. Mesh convergence plots for stress at these three locations are shown in Figures O.6 to O.8. Stress at notch location does not converge to a single value. Instead, it goes to infinity for increased mesh refinement. This is typical for a numerical stress singularity in the model. Consequently, stress at location B does not provide usable information about stress at notch location. Therefore, stress at C has been evaluated as well. This stress is expected to be lower than stress at B. However, stress at B should be the same order of magnitude as stress at A. Stress at A converges to 307 MPa and stress at C to 274 MPa. Since these to values have the same order of magnitude, stress at wall ends and notch location are expected to be equal.

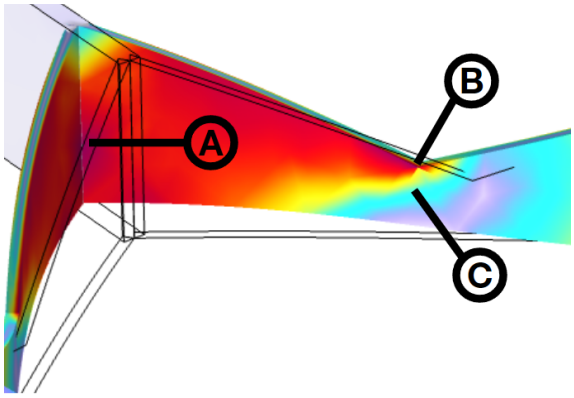

Figure O.5: Close-up of honeycomb plate stress distribution, shown in Figure 5.10.

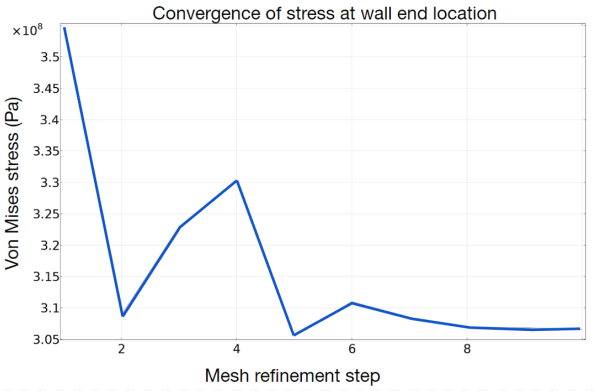

Figure O.6: Mesh convergence of stress at honeycomb wall end location (A).

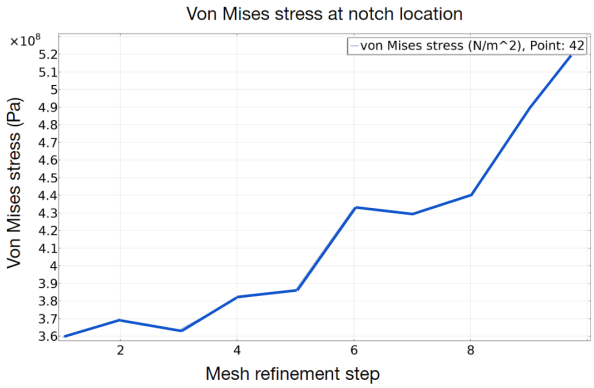

Figure O.7: Mesh convergence at notch location for mesh refinement (B).

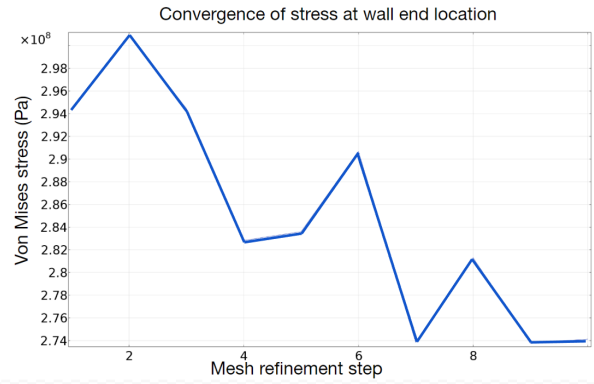

Figure O.8: Mesh convergence of stress at (C) (0.05 mm below B).

Foil

Foil stress and deflection have been evaluated with the model shown in Figure O.9. Stress in this model has been evaluated at three locations, indicated with coloured dots. The location of the blue dot is comparable to the stress evaluation of the simplified model. The red dot evaluates stress between two neighbouring simplified models. The green dot is located at location of maximum stress. Mesh convergence for stress at the blue, red and green dot is shown in Figure O.11 by the blue, red and green line respectively. The green line goes to infinity for

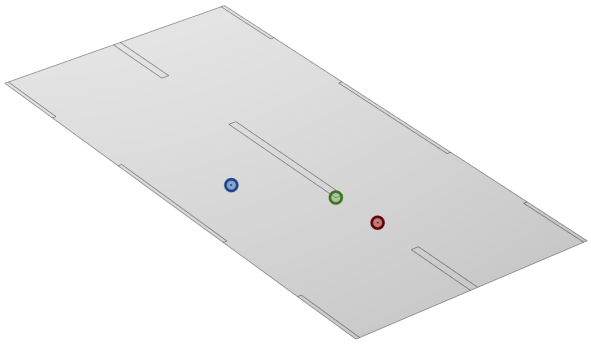

Figure O.9: Locations of foil stress evaluation.

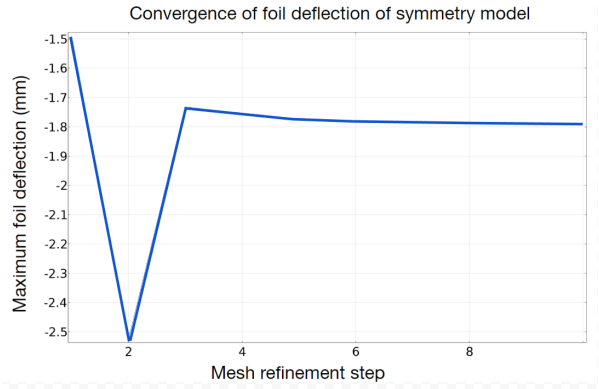

Figure O.10: Mesh convergence of maximum deflection of the foil in the symmetry model.

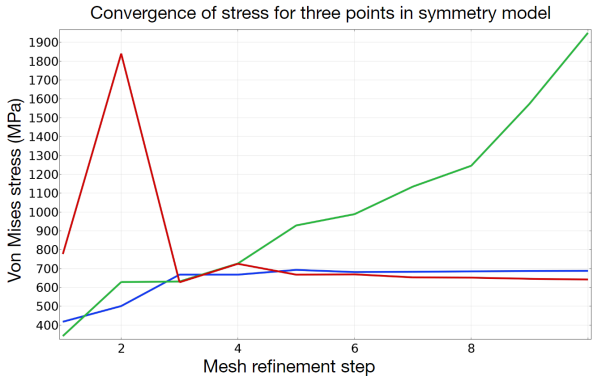

Figure O.11: Mesh convergence of stress at three points in the symmetry model.

increased mesh refinement. Therefore, stress concentration at the location of the green point is caused by numerical singularity and does not give accurate information about stress at this location. Stress at the blue point converges to 687.529 MPa and stress at the red point converges to 641.446 MPa. Maximum deflection of the foil is evaluated at the green point. It converges to -1.7886 mm, which is well within the maximum allowed deflection.

O.3 Models for thermal performance

O.3.1 Verification models

Solid conduction and gaseous conduction

Quartic elements have been used for both the solid and gaseous conduction models. The final temperature for the 10 mesh refinement steps is shown in Tables O.1 and O.3 for solid and gaseous conduction respectively. Relative difference between values is low (order of 10^{-10}% for solid conduction and 10^{-12}% for gaseous conduction). Furthermore, fluctuations in these values are of random nature. This is typical for rounding errors. Refining the mesh further will not have an effect on the acquired temperatures. Corresponding mesh convergence plots are shown in Figures O.12 and O.13. These plots do not show convergence to a certain value, as expected.

Edge losses

Quartic elements have been used for the envelope model. The final temperature for the 10 mesh refinement steps is shown in Table O.3. Relative differences between the evaluated temperatures of consecutive mesh refinement steps are low (order of 10^{-14}%). Furthermore, fluctuations in these values are of random nature. This is typical for rounding errors. Refining the mesh further will not have an effect on the acquired temperatures. The Corresponding mesh convergence plot is shown in Figure O.15. This plot does not show convergence, as expected.

Radiation

The empty box model has been modelled as two shells placed at a distance equal to the panel thickness from each other. The shell domains are modelled with quartic elements. Increasing the degrees of freedom for surface-to-surface radiation only results in slower convergence. Therefore, the least amount of degrees of freedom is chosen for this domain. Hemicube surface-to-surface radiation method with a resolution of 32 and linear discretisation is used. Figure O.14 shows the mesh convergence plot of the model. Temperature converges to 273.3562570 K.

Mesh refinement step	Nr. of DOFs	Temperature (K)
1	253	273.4665358435258
2	293	273.4665358435049
3	505	273.4665358434817
4	981	273.46653584353095
5	2025	273.46653584356096
6	3925	273.46653584349343
7	7641	273.46653584347763
8	15257	273.46653584331426
9	31585	273.46653584278994
10	65733	273.46653584434483

Table O.1: Temperature of the simplified model's top edge (solid conduction) for mesh refinement.

Mesh refinement step	Nr. of DOFs	Temperature (K)
1	10645	273.1525070856864
2	41125	273.1525070856874
3	90637	273.1525070856865
4	158601	273.15250708568504
5	247257	273.1525070856692
6	356851	273.1525070856827
7	485023	273.15250708567396
8	622253	273.1525070856854
9	813815	273.1525070856825
10	1532865	273.1525070856685

Table O.2: The empty box model's top surface temperature (gaseous conduction) for mesh refinement.

Mesh refinement step	Nr. of DOFs	Temperature (K)
1	257	288.3414987823776
2	457	288.34149878237747
3	985	288.34149878237736
4	1949	288.34149878237696
5	3853	288.34149878237616
6	8057	288.3414987823741
7	16953	288.34149878236815
8	35413	288.34149878237184
9	74033	288.3414987823251
10	156457	288.34149878231744

Table O.3: Temperature of the envelope model's top edge for mesh refinement.

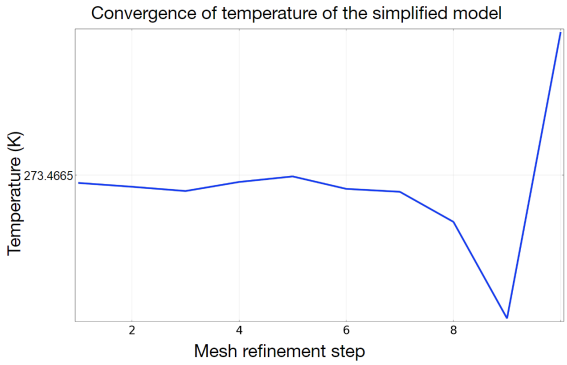

Figure O.12: Mesh convergence of temperature of top surface of the simplified model as a result of solid conduction.

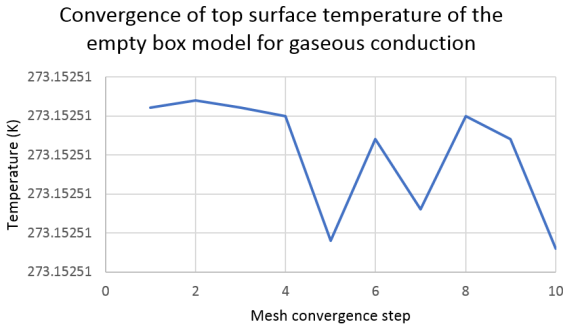

Figure O.13: Mesh convergence temperature of top surface of the empty box model as a result of gaseous conduction.

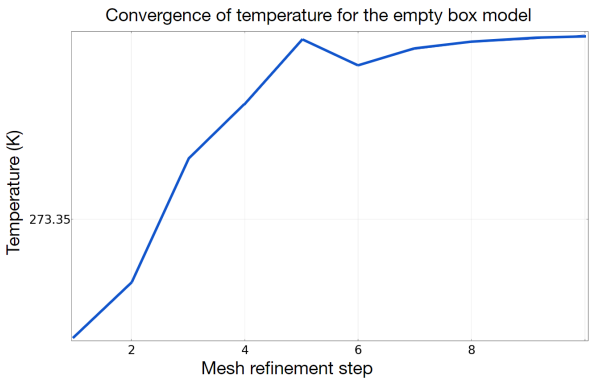

Figure O.14: Mesh convergence of average temperature of the top empty box model plate as a result of radiation.

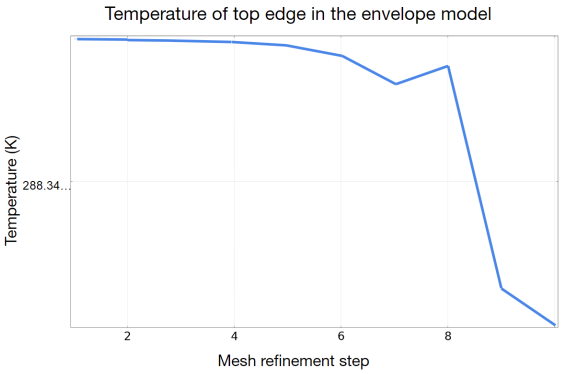

Figure O.15: Mesh convergence of temperature of the top edge in the envelope model.

O.3.2 Thermal performance models

Solid conduction

One-dimensional solid conduction is simulated in the simplified model. Three-dimensional solid conduction is simulated with two models, presented in Section 5.3.3. The symmetry model is a reduced version of the model shown in Figure 5.25. Both models are simulated using quintic elements. Mesh convergence of both models is shown in Figure O.16. Reducing the size of the symmetry model has no effect on the final temperature and convergence rate. However, the amount of degrees of freedom for the finest simulated mesh is 752229 for the larger model and 193779 for the smaller model. Figure O.17 shows the temperature distribution in the larger symmetry model for reference.

As mentioned in Appendix O.1, shell elements are preferred over solid elements for modelling honeycomb plate walls. However, the absence of geometrical thickness does have an effect on simulated conductance. honeycomb wall thickness shortens the effective foil length between two walls. Therefore, foil length is adjusted such that it is equal to the effective foil length. However, this means that the FEM model is slightly shortened.

Total length reduction is equal to four times the honeycomb wall thickness for the larger symmetry model. The distance between honeycomb walls is shortened by two times the honeycomb wall thickness for the larger symmetry model. Length reduction in the smaller symmetry model is half the length reduction in the larger symmetry model. Consequently, the volume of the

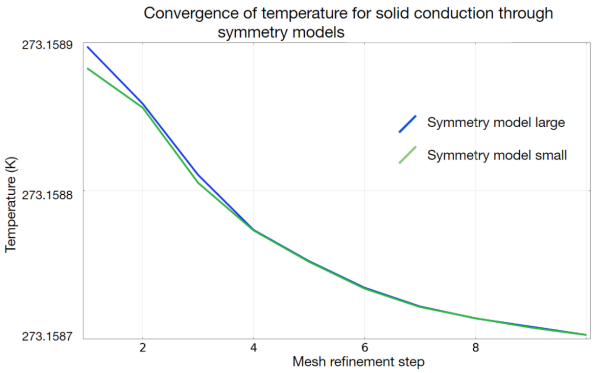

Figure O.16: Mesh convergences of average temperature of top surface in small and large symmetry mode as a result of isolated solid conduction.

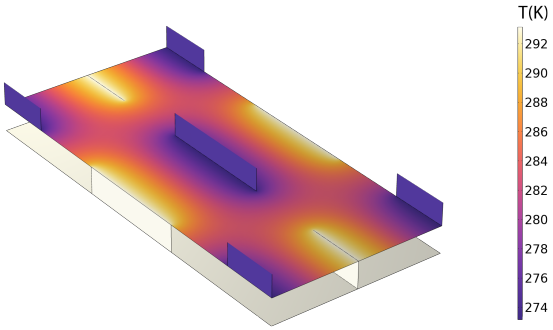

Figure O.17: Temperature distribution in the larger symmetry model.

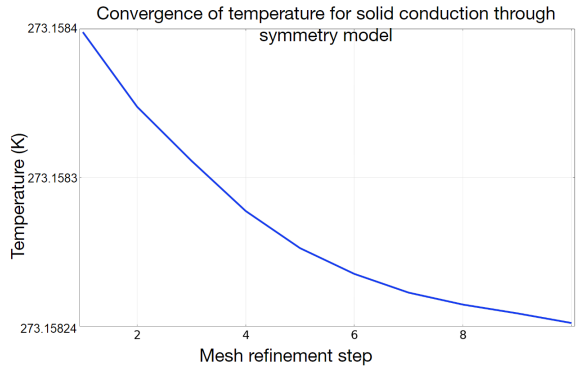

Figure O.18: Mesh convergence of average temperature of top surface in symmetry model 1 as a result of isolated solid conduction.

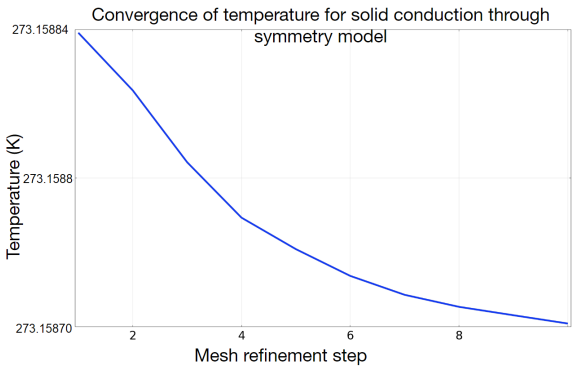

Figure O.19: Mesh convergence of average temperature of top surface in symmetry model 2 as a result of isolated solid conduction.

domains where gaseous conduction occurs reduces as well. This volume reduction will influence gaseous conduction and radiation. However, this is neglected since the volume change is only 3%.

Gaseous conduction and radiation are evaluated in combination with the symmetry model. The temperature in the symmetry model is evaluated for a symmetry model without the reduction in length, symmetry model 1, and a model with reduced length, symmetry model 2. Symmetry model 2 is accurate for solid conduction. Symmetry model 1 is used to estimate the error caused by reducing the length in gaseous conduction and radiation models.

Quintic elements have been used for convergence of the average temperature of the top surface in the symmetry model as a result of solid conduction. Figures O.18 and O.19 show the mesh convergence plot for 10 mesh convergence steps for symmetry models one and two respectively. The temperature of the top surface converges to 273.15824 K for symmetry model 1 and to 273.15869 for symmetry model 2. This corresponds with a thermal resistance of 249.9 K/W and 230.0 K/W respectively.

Gaseous conduction

Quartic elements have been used in the model for solid and gaseous conduction. Symmetry model 1 and 2 (with added air domains) are both evaluated. Mesh convergence of both models is shown in Figure O.20. Temperature of the top surface of model 1 and 2 converges to 273.16224

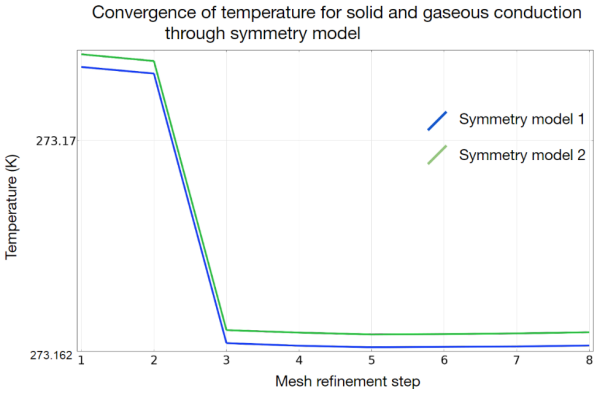

Figure O.20: Mesh convergence of average temperature of top surface in the two symmetry model as a result of solid and gaseous conduction.

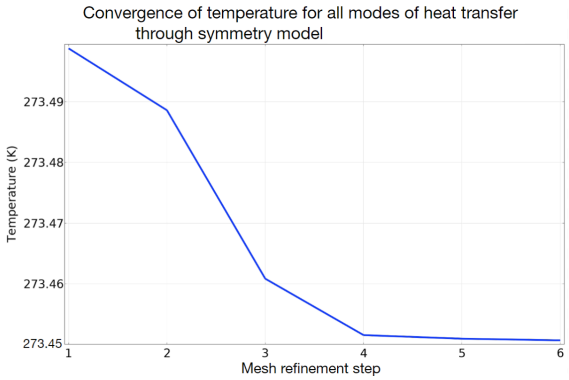

Figure O.21: Mesh convergence of average temperature of top surface in the symmetry model as a result of all modes of heat transfer for multiple element order combinations.

and 273.16274 K respectively. These temperatures correspond to a thermal resistance of 163.3 and 156.8 respectively. Thermal resistance of gaseous conduction as if it would act perfectly parallel to solid conduction, R_{gas}, can be calculated with Equation (O.6). Herein, $R_{gas+solid}$ is the thermal resistance obtained from the symmetry models and R_{solid} is the thermal resistance to solid conduction through the symmetry models. R_{gas} in symmetry model 1 and 2 is equal to 471.2 K/W and 492.6 K/W. A reduction in length of 3% results in an increase in thermal resistance of gaseous conduction of 4%. However, the benefit of using shell elements to reduce computation time outweighs the small change in thermal resistance to gaseous conduction. An error of 4% in the gaseous conduction will not significantly affect the total heat transfer estimation since the thermal resistance to gaseous conduction is the highest of all modes (shown in Table 5.1). Therefore, gaseous conduction is the least dominant mode of heat transfer.

$$R_{gas} = \frac{1}{\frac{1}{R_{gas+solid}} - \frac{1}{R_{solid}}} \tag{O.6}$$

Radiation

In general, higher element orders result in more accurate simulation results. However, increasing the order of radiosity for radiation barely has any effect on the final temperature and the convergence speed of the model as shown by the red and blue line in Figure O.22. Furthermore, radiation resolution also has little effect on the final solution. This is shown by the green and cyan lines in Figure O.22. Decreasing the order of shell elements does have an effect on the convergence speed. Therefore, a combination of high-order (quintic) shell elements, low-order (quadratic) surface radiosity and low radiation resolution (32) is optimal. The temperature of the top surface converges to 273.4 K for this optimal element combination, which corresponds to a thermal resistance of 7.9 K/W.

Reducing the total size of the FEM model does have an effect on radiative heat transfer. Heat radiates in all directions from a hot surface. The size of the radiating and the receiving surface with respect to open surfaces at the sides of the model is reduced for smaller models. A larger portion of heat radiated from a hot surface will therefore not reach the cold surface and disappears to the sides. Furthermore, COMSOL multiphysics allows for only one set of perpendicular symmetry planes for radiation in a model. Two symmetry planes, shown in Figure O.23 are

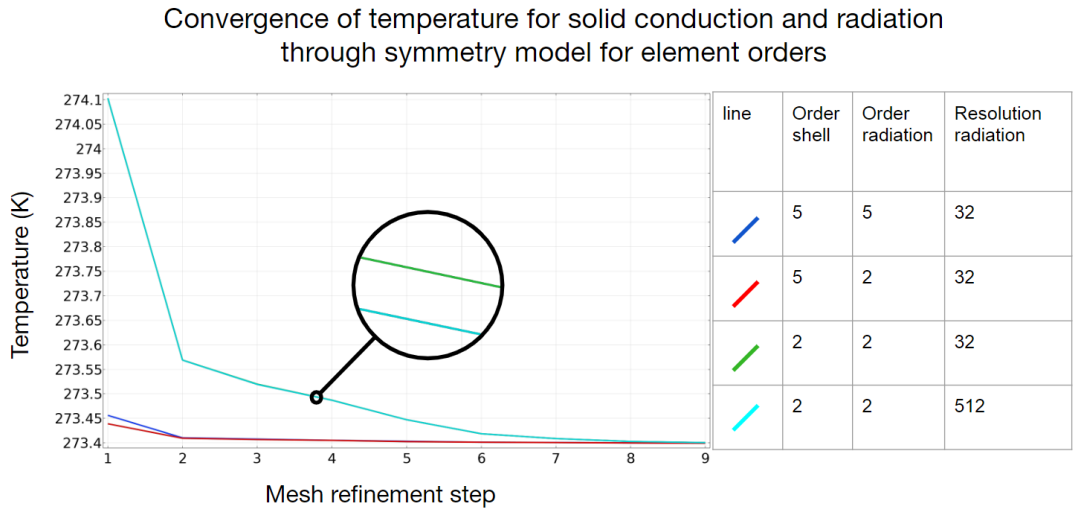

Figure O.22: Mesh convergence of average temperature of top surface in the symmetry model as a result of solid conduction and radiation for multiple element order combinations.

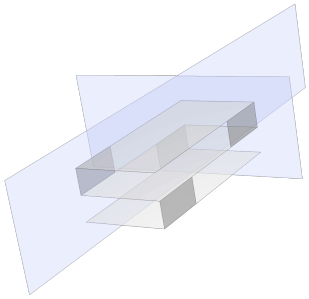

Figure O.23: Radiation symmetry planes.

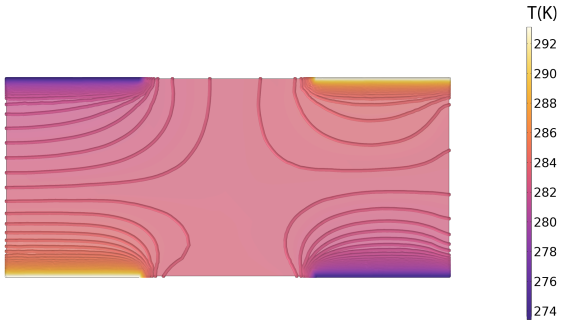

Figure O.24: Isothermal contour lines in the foil for solid conduction and radiation model.

applied, where four planes are actually necessary. This affects temperature distribution in the foil, as shown in Figure O.24. Symmetry planes have been applied at this foil's top and left sides. Isothermal contour lines at these edges show a smoother distribution compared to lines at the other two sides. The smaller model and the restriction on the number of symmetry planes induce modelling errors. However, thermal resistance to radiative heat transfer will always reduce for smaller models. No amount of symmetry planes can balance this reduction. Nonetheless, thermal resistance to radiative heat transfer is expected to be lower than the value obtained from this finite element simulation.

All modes of heat transfer

The final FEM model for thermal conduction incorporates all modes of heat transfer. Solid conduction has been modelled with shell elements. Gaseous conduction with solid domains. Radiation occurs at all surfaces of the shells used for solid conduction. The gaseous domain is treated as a transparent surface for radiation. Based on findings for the model for solid conduction and radiation, quintic elements have been used for the solid and gaseous conduction domains and low-resolution (32) quadratic elements have been used for surface radiosity. The temperature converges to 273.45 K, which corresponds to a thermal resistance of 6.57 K/W. However, actual thermal resistance to all modes of heat transfer is expected to be lower since thermal resistance to radiation is expected to be lower. Furthermore, edge effect should be added for a complete evaluation of all modes of heat transfer.

Appendix P Thermal resistance of FEM models

P.1 The total panel's thermal resistance

The boundary conditions that hold for all finite element models are shown in Figure P.1. All edges and surfaces at the bottom of the model (red) have a fixed temperature of 293.15 K, a heat flux of 10 W/m^2 is applied to the top edges and surfaces (blue) and the external air temperature is equal to 273.15 K. The grey box can be replaced with an arbitrary heat transfer model. Each model will let a certain amount of heat through from the hot to the cold surface, causing the top surface to heat up slightly. Because the top surface no longer has a temperature of 273.15 K, heat will be transferred from the top surface to the air surrounding it via convection. Heat transfer through the model and convection from the top have to be equal according to the first law of thermodynamics, discussed in Section 2.2.1. A conductivity k exists for which conduction through a solid between the hot and cold plate (the grey block) equals the amount of heat transferred by whatever mode of heat transfer is (or are) present in the model. Consequently, the two equations for the total energy transferred by one-dimensional solid conduction and convection, shown in Equations (P.1) and (P.2) respectively, have to be equal. The relevant area for convection A_{conv} is equal to the model area A_{model} if the top envelope is present. This top envelope is present in most, but not all, models. A final value for k can be calculated. Consequently, the thermal resistance of the model can be calculated with Equation (P.3) for the found value for thermal conductivity. The total thermal resistance of the panel can now be found by multiplying the thermal resistance of the model by the area fraction A_{model}/A_{panel}, as shown in Equation (P.4).

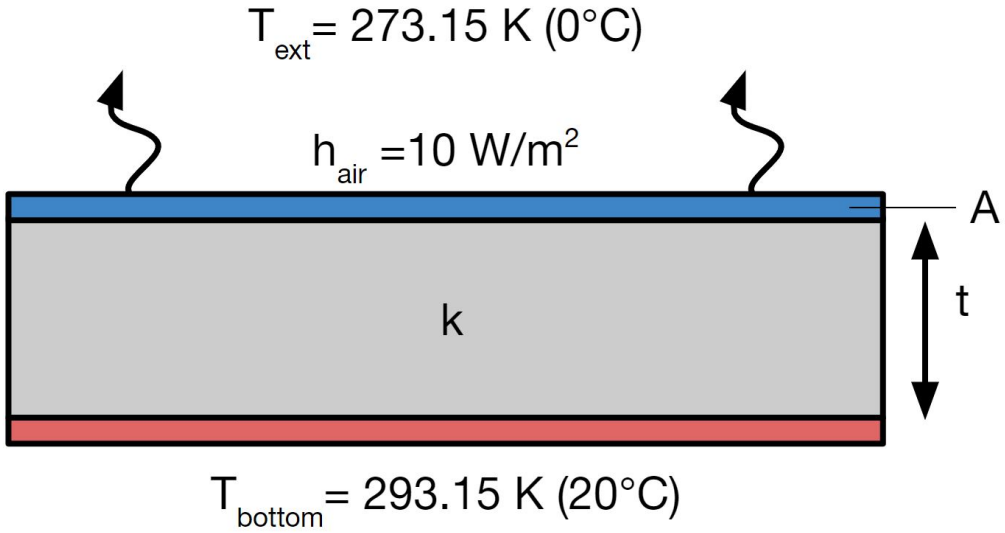

Figure P.1: General boundary conditions for all heat transfer models.

$$\dot{Q}_{conduction} = \frac{kA_{model}(T_{red} - T_{blue})}{t} \tag{P.1}$$

$$\dot{Q}_{convection} = hA_{conv}(T_{blue} - T_{ext}) \tag{P.2}$$

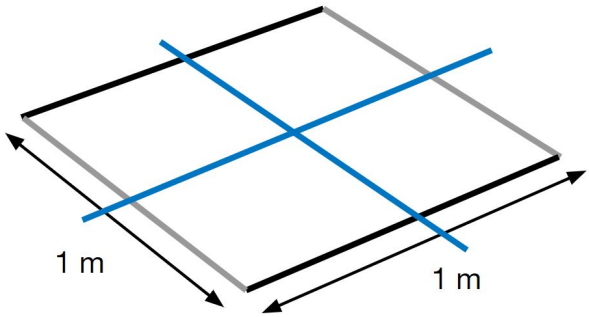

Figure P.2: Edges of the panel with blue symmetry lines.

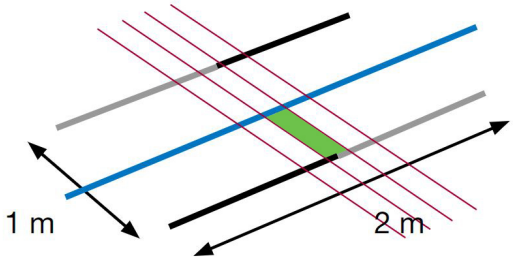

Figure P.3: Hypothetical panel geometry with symmetry line, possible panel section borders and a panel section area shown in blue, red and green respectively.

$$R_{model} = \frac{t}{kA_{model}} \tag{P.3}$$

$$R_{panel} = \frac{R_{model}A_{model}}{A_{panel}} \tag{P.4}$$

P.2 Geometry of the model for edge losses

A square-meter panel has been considered in this thesis. The edges of this panel are represented by the black and grey lines in Figure P.2. The blue lines in this figure represent symmetry lines. For this panel geometry, the smallest usable panel section is one-fourth of the total panel. However, smaller usable panel sections can be obtained by altering the geometry. This hypothetical geometry is obtained by rotating the grey edges in Figure P.2 by 90 degrees and re-aligning the newly obtained panel sides. Figure P.3 shows this hypothetical panel. This hypothetical panel has a total edge length equal to the original panel (note that two of the four sides of this panel are missing edges, which is impossible in reality). Therefore, the same amount of heat will be transferred through the edges shown in Figures P.2 and P.3. The blue line in Figure P.3 shows the symmetry line. Multiple small panel sections, bordered by two red lines, the blue symmetry line and a panel's edge can be created. The width of the envelope model (i.e. the distance between two red lines in Figure P.3) presented in Section 5.3.2 is set to the panel thickness (1 cm). The green area represents the area of such a panel section. Using this model affects the areas in the equations in Appendix P.1. A_{panel}, A_{model} and A_{conv} are equal to $2w_p^2$, $0.5w_pt_p$ and t_et_p respectively, where t_e is the total thickness of an MF2 envelope (65 µm).

Bibliography

[1] UNFCCC. Adoption of the Paris Agreement. Paris, Nov 2015.

[2] Ministerie van Infrastructuur en Waterstaat. Klimaatbeleid. https://www.rijksoverheid.nl/onderwerpen/klimaatverandering/klimaatbeleid, Aug 2021. Accessed: 5-10-2021.

[3] H. Ritchie and M. Roser. Emissions by sector. https://ourworldindata.org/emissions-by-sector, May 2020. Accessed: 19-10-2021.

[4] European Commission. Energy consumption by end-use. https://ec.europa.eu/energy/content/energy-consumption-end-use_en, Jun 2019. Accessed: 19-10-2021.

[5] Eurostat. Energy consumption in households. https://ec.europa.eu/eurostat/statistics-explained/index.php?title=Energy_consumption_in_households&oldid=488255#Energy_products_used_in_the_residential_sector, 2019. Accessed: 19-10-2021.

[6] J. Wassink. Hoe duurzaam is elektrisch verwarmen? https://www.tudelft.nl/delft-integraal/articles/hoe-duurzaam-is-elektrisch-verwarmen, dec 2018. Accessed: 19-10-2021.

[7] Z. Fang, N. Li, B. Li, G. Luo, and Y. Huang. The effect of building envelope insulation on cooling energy consumption in summer. *Energy and Buildings*, 77:197–205, Mar 2014. doi: 10.1016/j.enbuild.2014.03.030.

[8] M. Morsy, M. Fahmy, H.A. Elshakour, and A.M. Belal. Effect of thermal insulation on building thermal comfort and energy consumption in Egypt. *Journal of Advanced Research in Applied Mechanics*, 43(1), 2018.

[9] Calcasa B.V. 2022 q2 wox kwartaalbericht: Ondanks vergroening blijft percentage slechte labels gelijk. https://www.calcasa.nl/nieuws/2022-q2-wox-kwartaalbericht-ondanks-vergroening-blijft-percentage-slechte-labels-gelijk, Sep 2022. Accessed: 27-10-2022.

[10] A. Binz, A. Moosmann, G. Steinke, U. Schonhardt, F. Fregnan, H. Simmler, S. Brunner, K. Ghazi, R. Bundi, U. Heinemann, H. Schwab, J.J.M. Cauberg, M.J. Tenpierik, G. Johannesson, T. Thorsell, M. Erb, and B. Nussbaumer. *Vacuum insulation in the building sector : systems and applications*. s.n., 2005.

[11] J. Schnieders, W. Feist, and L. Rongen. Passive houses for different climate zones. *Energy and Buildings*, 105:71–87, 2015. doi: 10.1016/j.enbuild.2015.07.032.

[12] R. Baetens, B.P. Jelle, J.V. Thue, M.J. Tenpierik, S. Grynning, S. Uvsløkk, and A. Gustavsen. Vacuum insulation panels for building applications: A review and beyond. *Energy and Buildings*, 42(2):147–172, 2009. doi: 10.1016/j.enbuild.2009.09.005.

[13] H. Simmler and S. Brunner. Vacuum insulation panels for building application: Basic properties, aging mechanisms and service life. *Energy and Buildings*, 37(11):1122–1131, 2005. doi: 10.1016/j.enbuild.2005.06.015.

[14] N. Simões, M. Gonçalves, C. Serra, and S. Resalati. Can vacuum insulation panels be cost-effective when applied in building façades? *Building and Environment*, 191:107602, 2021. doi: 10.1016/j.buildenv.2021.107602.

[15] M.M. Koebel, J. Wernery, and W.J. Malfait. Energy in buildings—policy, materials and solutions. *MRS Energy amp; Sustainability*, 4:1–12, 2017. doi: 10.1557/mre.2017.14.

[16] A.F. Mills. *Basic Heat and Mass Transfer*. PEARSON, Harlow, 2014.

[17] K.H. Brodt. *Thermal insulations: cfc-alternatives and vacuum insulation*. PhD thesis, Delft university of technology, Delft, Jun 1995.

[18] R. Caps, U. Heinemann, M. Ehrmanntraut, and J. Fricke. Evacuated insulation panels filled with pyrogenic silica powders: properties and applications. *High Temperatures High Pressures*, 33(2):151–156, 2001.

[19] H. Wu, S. Grabarnik, A. Emadi, G. Graaf, and R. Wolffenbuttel. Characterization of thermal cross-talk in a mems-based thermopile detector array. *Journal of Micromechanics and Microengineering*, 19:074022, 06 2009. doi: 10.1088/0960-1317/19/7/074022.

[20] C. Escriba, E. Campo, D. Estève, and J.Y. Fourniols. Complete analytical modeling and analysis of micromachined thermoelectric uncooled ir sensors. *Sensors and Actuators A: Physical*, 120(1):267–276, 2005. ISSN 0924-4247. doi: 10.1016/j.sna.2004.11.027.

[21] M. Ashby, H. Shercliff, and D. Cebon. *Materials Engineering, Science, Processing and Design*. Elsevier Ltd., Oxford, 2014.

[22] T.G. Langdon and F.A Mohamed. A simple method of constructing an ashby-type deformation mechanism map. *Journal of Material Science*, 13:1282–1290, 1978. doi: 10.1007/BF00544735.

[23] M.E. Kassner, P. Geantil, and R.S. Rosen. Ambient temperature creep of type 304 stainless steel. *Journal of engineering materials and technology*, 133(2), 2011.

[24] S. Fuller. Life-cycle cost analysis (LCCA). *National Institute of Building Sciences, An Authoritative Source of Innovative Solutions for the Built Environment*, 1090:1–11, 2010.

[25] K. Foo, G. Chai, and L. Seah. Mechanical properties of nomex material and nomex honeycomb structure. *Composite Structures*, 80:588–594, 10 2007. doi: 10.1016/j.compstruct.2006.07.010.

[26] J.W. Klintworth and W.J. Stronge. Elasto-plastic yield limits and deformation laws for transversely crushed honeycombs. *International Journal of Mechanical Sciences*, 30(3):273–292, 1988. doi: 10.1016/0020-7403(88)90060-4.

[27] M. P. Savruk and A. Kazberuk. *Stress concentration at notches*. Springer, Steinhausen, 2017.

[28] Vulkan Europe BV. Basaltvezel roving. `https://vulkan-europe.com/roving/`. Accessed: 02-06-2022.

[29] R. Hatakenaka, M. Takeshi, H. Sugita, M. Saitoh, and T. Hirai. *Thermal Performance and Practical Utility of a MLI Blanket using Plastic Pins for Space Use*, page 3503. American Institute of Aeronautics and Astronautics, Vail,CO, 2013. doi: 10.2514/6.2013-3503.

[30] A.V. Nenarokomov, L.A. Dombrovsky, I.V. Krainova, O.M. Alifanov, and S.A. Budnik. Identification of radiative heat transfer parameters in multilayer thermal insulation of spacecraft. *International Journal of Numerical Methods for Heat & Fluid Flow*, 2017.

[31] M. Kanda, K. Matsumoto, and S. Yamaguchi. Heat transfer through multi-layer insulation

(mli). *Physica C: Superconductivity and its Applications*, 583:1353799, 2021. doi: 10.1016/j.physc.2020.1353799.

[32] J.S. Chang, S.U. Yang, Y.S. Jung, and H. Huh. Quantitative analysis on the radiative and conductive heat transfer through space-borne mli based on theoretical approach. In *49th International Conference on Environmental Systems*, Boston,MA, 2019. International Conference on Environmental Systems.

[33] B. Suurmeijer, T. Mulder, and J. Verhoeven. *Vacuum science and Technology.* high tech institute and settels savenije group of companies, Eindhoven, 2000.

[34] K.G. Wakili, R. Bundi, and B. Binder. Effective thermal conductivity of vacuum insulation panels. *Building Research and Information*, 32:293–299, 07 2004. doi: 10.1080/0961321042000189644.

[35] T.N. Bitzer. *Honeycomb technology: materials, design, manufacturing, applications and testing.* Springer Science & Business Media, Dublin,CA, 1997.

[36] P. Karami, N. Al-Ayish, and K. Gudmundsson. A comparative study of the environmental impact of swedish residential buildings with vacuum insulation panels. *Energy and Buildings*, 109:183–194, 2015. doi: 10.1016/j.enbuild.2015.10.031.

[37] V.D Chaudhari and A.D. Desai. Performance evaluation of vacuum system: Pump-down time. *International Journal of Scientific & Engineering Research*, 2:1–4, 2011.

[38] S.D. Papka and S. Kyriakides. In-plane compressive response and crushing of honeycomb. *Journal of the Mechanics and Physics of Solids*, 42(10):1499–1532, 1994. doi: 10.1016/0022-5096(94)90085-X.

[39] E. Wegger, B.P. Jelle, E. Sveipe, S. Grynning, A. Gustavsen, R. Baetens, and J.V. Thue. Aging effects on thermal properties and service life of vacuum insulation panels. *Journal of Building Physics*, 35(2):128–167, 2011. doi: 10.1177/1744259111398635.

[40] S.M. Elsherbiny, G.D. Raithby, and K.G.T. Hollands. Heat Transfer by Natural Convection Across Vertical and Inclined Air Layers. *Journal of Heat Transfer*, 104(1):96–102, 1982. doi: 10.1115/1.3245075.

[41] B. Gross and A. Mendelson. Plane elastostatic analysis of v-notched plates. *International Journal of Fracture Mechanics*, 8(3):267–276, 1972. doi: 10.1007/BF00186126.

[42] J.H. Kim, F.E. Boafo, S.M. Kim, and J.T. Kim. Aging performance evaluation of vacuum insulation panel (VIP). *Case Studies in Construction Materials*, 7:329–335, 2017. doi: 10.1016/j.cscm.2017.09.003.

[43] S.A. Omer, S.B. Riffat, and G. Qiu. Thermal insulations for hot water cylinders: a review and a conceptual evaluation. *Building Services Engineering Research and Technology*, 28 (3):275–293, 2007. doi: 10.1177/0143624406075269.

[44] K. Cho, Y. Hong, and J. Seo. Assessment of the economic performance of vacuum insulation panels for housing projects. *Energy and Buildings*, 70:45–51, 2014. doi: 10.1016/j.enbuild.2013.11.073.

[45] M. Alam, H. Singh, S. Suresh, and D.A.G. Redpath. Energy and economic analysis of vacuum insulation panels (VIPs) used in non-domestic buildings. *Applied Energy*, 188:1–8, 2017. doi: 10.1016/j.apenergy.2016.11.115.

[46] S.S. Alotaibi and S. Riffat. Vacuum insulated panels for sustainable buildings: a review of research and applications. *International Journal of Energy Research*, 38(1):1–19, 2014. doi: 10.1002/er.3101.

[47] M. Davraz and H.C. Bayrakci. Performance properties of vacuum insulation panels produced with various filling materials. *Science and Engineering of Composite Materials*, 21 (4):521–527, 2014. doi: 10.1515/secm-2013-0162.

[48] M. Koru. Determination of thermal conductivity of closed-cell insulation materials that depend on temperature and density. *Arabian Journal for Science and Engineering*, 41: 4337–4346, 2016. doi: 10.1007/s13369-016-2122-6.

[49] M. Kayfeci. Determination of energy saving and optimum insulation thicknesses of the heating piping systems for different insulation materials. *Energy and Buildings*, 69:278–284, 2014. doi: 10.1016/j.enbuild.2013.11.017.

[50] A.M. Papadopoulos. State of the art in thermal insulation materials and aims for future developments. *Energy and Buildings*, 37(1):77–86, 2005. doi: 10.1016/j.enbuild.2004.05.006.

[51] E. Cuce, P.M. Cuce, C.J. Wood, and S.B. Riffat. Toward aerogel based thermal superinsulation in buildings: A comprehensive review. *Renewable and Sustainable Energy Reviews*, 34:273–299, 2014. doi: 10.1016/j.rser.2014.03.017.

[52] S.A. Al-Sanea, M.F. Zedan, S.A. Al-Ajlan, and A.S.A. Hadi. Heat transfer characteristics and optimum insulation thickness for cavity walls. *Journal of Thermal Envelope and Building Science*, 26(3):285–307, 2003. doi: 10.1177/109719603027973.

[53] H.R. Kymäläinen and A.M. Sjöberg. Flax and hemp fibres as raw materials for thermal insulations. *Building and Environment*, 43(7):1261–1269, 2008. doi: 10.1016/j.buildenv.2007.03.006.

[54] M. Kayfeci, A. Keçebaş, and E. Gedik. Determination of optimum insulation thickness of external walls with two different methods in cooling applications. *Applied Thermal Engineering*, 50(1):217–224, 2013. doi: 10.1016/j.applthermaleng.2012.06.031.

[55] W. Villasmil, L.J. Fischer, and J. Worlitschek. A review and evaluation of thermal insulation materials and methods for thermal energy storage systems. *Renewable and Sustainable Energy Reviews*, 103:71–84, 2019. doi: 10.1016/j.rser.2018.12.040.

[56] CiDRA Precision Services. Silica - fused silica (silicon dioxide). `https://www.azom.com/article.aspx?ArticleID=1387`, 2018. Accessed: 25-09-2021.

[57] M.A. Lacasse and C. Sjöström. Recent advances in methods for service life prediction of buildings materials and components-an overview. In *Proceedings. CIB world building congress*, pages 1–10, Toronto, 2004. Institute for Research in Construction.

[58] M.J. Tenpierik, W.H. van der Spoel, and J.J.M. Cauberg. Simplified analytical models for service life prediction of a vacuum insulation panel. In *Proceedings of 8th International Vacuum Insulation Symposium*, pages 1–8, Bayern, 2007. ZAE-Bayern Universitat.

[59] H. Simmler and S. Brunner. Ageing and service life of VIPs in buildings. *Proceedings of the 7th International Vacuum Insulation Symposium*, pages 15–22, 2005.

[60] H. Schwab. *Vakuumisolationspaneele : Gas- und Feuchteeintrag sowie Feuchte- und Wärmetransport*. PhD thesis, Universität Würzburg, Würzburg, Oct 2005.

[61] H. Simmler, S. Brunner, U. Heinemann, H. Schwab, K. Kumaran, P. Mukhopadhyaya, D. Quenard, H. Sallee, K. Noller, E. Kuecuekpinar-Niarchos, C. Stramm, M. Tenpierik, H. Cauberg, and M. Erb. Vacuum insulation panels - study on VIP-components and panels for service life prediction of VIP in building applications (subtask a). Technical report, Swiss Federal Office of Energy, Berne.

[62] A. Beck, O. Frank, and M. Binder. Influence of water content on the thermal conductivity of vacuum panels with fumed silica kernels. In *Proceedings of the 8th International Vacuum Insulation Symposium*, pages 1–9, Würzburg, 2007. Bavarian Center for Applied Energy Research.

[63] M.J. Tenpierik. *Vacuümisolatiepanelen toegepast in bouwconstructies*. PhD thesis, Delft University of Technology, Delft, Feb 2010.

[64] M.A. Aegerter, N. Leventis, and M.M. Koebel. *Aerogels handbook*. Springer Science & Business Media, New York, NY, 2011.

[65] NVM. Marktinformatie vrije sector huur. `https://www.nvm.nl/wonen/marktinformatie/huurmarkt/`. Accessed: 05-11-2021.

[66] E. Di Giuseppe, M. Iannaccone, M. Telloni, M. D'Orazio, and C. Di Perna. Probabilistic life cycle costing of existing buildings retrofit interventions towards nZE target: Methodology and application example. *Energy and Buildings*, 144:416–432, 2017. doi: 10.1016/j.enbuild.2017.03.055.

[67] U. Schonhardt, A. Binz, M. Wohler, R. Dott, and R. Frischknecht. Eco-balance of a vacuum insulation panel (VIP); oekobilanz eines vakuum-isolations-paneels (VIP). Technical report, Institut für Energie, Muttenz, Jul 2003.

[68] Ansys. Granta EduPack version 21.2.0, 2022.

[69] L. Han. Resistance Calculator version 2.0. `https://www.mathworks.com/matlabcentral/fileexchange/42521-resistance-calculator`. Accessed: 18-05-2022.